THE FLORIDA STATE UNIVERSITY

COLLEGE OF ARTS AND SCIENCES

TROPICAL CYCLONE INNER-CORE DYNAMICS: A LATENT HEAT RETRIEVAL AND ITS EFFECTS ON INTENSITY AND STRUCTURE CHANGE; AND THE IMPACTS OF EFFECTIVE DIFFUSION ON THE AXISYMMETRIZATION PROCESS

By

STEPHEN GUIMOND

A Dissertation submitted to the
Department of Earth, Ocean and Atmospheric Science
in partial fulfillment of the
requirements for the degree of
Doctor of Philosophy

Degree Awarded:
Fall Semester, 2010

The members of the committee approve the dissertation of Stephen Guimond defended on August 25, 2010.

Mark Bourassa
Professor Directing Dissertation

Michael Navon
University Representative

Robert Hart
Committee Member

Ming Cai
Committee Member

Xiaolei Zou
Committee Member

The Graduate School has verified and approved the above-named committee members.

I dedicate this to you, the reader.

ACKNOWLEDGMENTS

I would like to acknowledge Dr. Paul Reasor for his mentorship and research guidance during his years at FSU. I learned a great deal from him and this work is proof of that. He is sorely missed in the Department. I would also like to thank Dr. Mark Bourassa for providing enthusiasm and support of my work from the Master’s level up until the very end of my PhD. He always maintained a positive attitude even when I was not so optimistic. In addition, I would like to thank Dr. Jon Reisner for his support, mentorship and modeling expertise. I have and continue to learn much from him. Dr. Robert Hart has always been there throughout my time at FSU to provide constructive criticism on my work. His willingness to discuss my research in the absence of Paul is greatly appreciated. Drs. Chris Jeffery and Gerald Heymsfield provided support for visits to Los Alamos National Laboratory (LANL) and NASA Goddard Space Flight Center (GSFC), respectively as well as excellent feedback on the work.

Finally, I acknowledge Dr. David Nolan for many discussions on the work and providing figures from his paper, Dr. Robert Black for the particle data and processing in Hurricane Katrina (2005), Dr. Scott Braun for providing numerical model output, Dr. David Moulton for assistance with his PDE solver and Dr. Matt Eastin for providing a figure or two. This research was supported by the Los Alamos National Laboratory through a project entitled: “Flash Before the Storm: Predicting Hurricane Intensification using LANL Lightning Data” with Dr. Chris Jeffery the PI. In addition, financial support was also provided by a NASA ocean vector winds contract and a NOAA grant to Dr. Mark Bourassa.

TABLE OF CONTENTS

LIST OF TABLES

LIST OF FIGURES

ABSTRACT

Despite the fact that latent heating in cloud systems drives many atmospheric circulations, including tropical cyclones, little is known of its magnitude and structure due in large part to inadequate observations. In this work, a reasonably high-resolution (2 km), four-dimensional airborne Doppler radar retrieval of the latent heat of condensation is presented for rapidly intensifying Hurricane Guillermo (1997). Several advancements in the retrieval algorithm are shown including: (1) analyzing the scheme within the dynamically consistent framework of a numerical model, (2) identifying algorithm sensitivities through the use of ancillary data sources and (3) developing a precipitation budget storage term parameterization. The determination of the saturation state is shown to be an important part of the algorithm for updrafts of ~ 5 m s^{-1} or less. The uncertainties in the magnitude of the retrieved heating are dominated by errors in the vertical velocity. Using a combination of error propagation and Monte Carlo uncertainty techniques, biases were found to be small, and randomly distributed errors in the heating magnitude were ~16 % for updrafts greater than 5 m s^{-1} and ~156 % for updrafts of 1 m s^{-1}.

The impact of the retrievals is assessed by inserting the heating into realistic numerical simulations at 2 km resolution and comparing the generated wind structure to the Doppler radar observations of Guillermo. Results show that using the latent heat retrievals outperforms a simulation that relies on a state-of-the-art microphysics scheme (Reisner and Jeffery 2009), in terms of wind speed root-mean-square errors, explained variance and eye/eyewall structure. The incorrect transport of water vapor (a function of the sub-grid model and the numerical approximations to advection) and the restrictions on the magnitude of heat release that ensure the present model's stability are suggested as sources of error in the simulation without the retrievals.

Motivated by the latent heat retrievals, the dynamics of vortex axisymmetrization from the perspective of thermal anomalies is investigated using an idealized, non-linear atmospheric model (HIGRAD). Attempts at reproducing the results of previous work (Nolan and Grasso 2003; NG03) revealed a discrepancy with the impacts of purely asymmetric forcing. While NG03 found that purely asymmetric heating led to a negligible, largely negative impact on the vortex intensification, in the present study the impacts of asymmetries are found to have an important, largely positive role. Absolute angular momentum budgets revealed that the essential difference between the present work and that of NG03 was the existence of a significant, axisymmetric secondary circulation in the basic-state vortex used in the HIGRAD simulations. This secondary circulation was larger than that present in NG03's simulations. The spin-up of the vortex caused by the asymmetric thermal anomalies was dominated by the axisymmetric fluxes of angular momentum at all times, indicating fundamentally different evolution of asymmetries in the presence of radial flow.

Radial momentum budgets were performed to elucidate the mechanisms responsible for the formation of the physically significant secondary circulation. Results show that explicit (sub-grid) diffusion in the model was producing a gradient wind imbalance, which drives a radial inflow and associated secondary circulation in an attempt to re-gain balance. In addition, the production of vorticity anomalies from the asymmetric heating was found to be sensitive to the eddy diffusivity, with large differences between HIGRAD and the widely used WRF model for the exact same value of this uncertain parameter.

CHAPTER 1

INTRODUCTION

Tropical cyclones (TCs) can inflict great human suffering and pose a significant risk to the economic security of many nations through their impacts on workplace productivity, energy and infrastructure. The primary means of addressing these risks is through forecasts that provide decision-makers with timely information on the state of the atmosphere and ocean. Another method of mitigating TC risk is through the design of structures (e.g. building codes) that minimize damage from wind and water. If science cannot find a way to accurately predict or potentially modify the TC, then efforts to cope with their impacts through engineering solutions are likely the best options.

It is well known within the meteorological community that current TC intensity and structure forecasts contain large uncertainty with little improvement relative to forecasts of track over the past 20 – 30 years (DeMaria et al. 2005). An integral part of the forecasting and coping strategies for alleviating risk is the understanding of the physical mechanisms governing TC evolution. Although significant strides have been made in our understanding of the TC, several issues still impede our ability to advance the science including: (1) incomplete observation of the storm lifecycle, (2) incomplete knowledge of the physics on a multitude of scales, and (3) issues with the numerical details of solving a system of coupled, non-linear partial differential equations for which there is no unique solution (e.g. numerical approximations in space/time, parameterizations and predictability).

In this work, some of the critical issues plaguing TC science described above are addressed. In chapter two, an algorithm for the retrieval of the latent heat of condensation from airborne Doppler radar is presented and applied to unique observations of a rapidly intensifying storm. Chapter two also presents the results of realistic numerical simulations that utilize the new latent heat retrievals. In chapter three, the dynamics of vortex axisymmetrization from heating perturbations is studied using an idealized, non-linear numerical model. Comparisons with prior work are shown which highlight fundamental problems associated with numerically simulating large Reynolds number flows.

CHAPTER 2

LATENT HEAT AND TROPICAL CYCLONES

2.1 Background and Motivation

The main driver of TC genesis and intensity change is the release of latent heat (LH) in clouds where the source of moist entropy flux comes from the thermodynamic disequilibrium at the ocean-atmosphere interface (Charney and Eliassen 1964; Kuo 1965; Emanuel 1986). In the eyewall region, convective clouds dominate the core structure with a mix of stratiform and convective features extending out to the bands of the system. Integrated cloud heating over the entire volume of the storm is believed to be responsible for intensity and structure change (Cecil and Zipser 2003; Tory et al. 2006), although full-physics modeling studies (Braun 2002) and observational composites (Black et al. 1996) show that small-scale, intense convection ("hot towers") contribute the largest percentage of the total upward mass flux (~ 65 % from updrafts stronger than 2 m s^{-1}).

Despite the fundamental importance of LH release, little is known of the structure in both space and time during all phases of storm evolution. To make matters worse, balanced non-linear models of the vortex response to heating show large sensitivity to the structural characteristics (Hack and Schubert 1986). Most observational estimates of LH are from satellites, which have coarse resolution in both space (due to the height of the instrument as well as the limiting factors of antenna diameter and frequency choice) and time (due to orbit selection). Thus, the eyewall and rainband regions of a TC with embedded hot towers are poorly resolved leading to large errors in the LH field.

Early satellite estimates were made using passive microwave radiometers with horizontal resolutions of ~ 25 km at nadir (Adler and Rodgers 1977). The use of passive instruments for estimating LH release is difficult because of the broad, overlapping weighting functions and the complexity of the radiative transfer in clouds, especially those with mixed phase regions (Petty 2006). As a result, the specific details of hydrometeor distributions contributing to an observed brightness temperature can have large uncertainty. In addition, Adler and Rodgers (1977) and others (i.e. Sitkowski and Barnes 2009) use an estimate of the rainfall rate to compute LH; this approach represents a vertically integrated quantity and thus, less information on cloud structure is obtained. More recent satellite estimates use the Tropical Rainfall Measuring Mission (TRMM) Microwave Imager (TMI), which has a much higher horizontal resolution of ~ 4 - 5 km at 85 GHz. Rodgers et al. (2000) were the first to use the TMI to compute vertical profiles of LH in a TC and found that as the storm intensified, heating rates increased in the inner core and extended upward into the mid-upper troposphere. Recently, the TRMM Precipitation Radar (PR) has been used to estimate ~ 4.3 km horizontal and 0.25 km vertical resolution LH rates in TCs with three – dimensional (3D) capabilities (Tao et al. 2006).

Active instruments such as radars are not without errors either as many different drop size distributions and values of derived water content parameters, such as rainfall rate, can be associated with a measured value of reflectivity (Doviak and Zrnic 1984). As a result, LH estimates that rely solely on reflectivity derived parameters can be expected to contain significant random error (a factor of nearly four for mean rainfall rate; Doviak and Zrnic 1984). As the TRMM PR is non-Doppler, critical information needed in the computation of LH (three components of the wind, especially vertical velocity) is unknown. In addition, the ~ 4.3 km surface footprint of the PR is still too coarse to resolve the important details of hot towers and deep convection in TCs (Guimond et al. 2010).

Dual-polarization radar has been used to estimate warm rain and mixed phase microphysical processes in Florida convection (Tong et al. 1998). From an area-integrated perspective, Tong et al. (1998) found that warm rain processes (condensation and evaporation) dominated the total LH budget with a small component attributed to mixed phase processes (freezing/melting). Although very few dual-polarization observations of TCs have been published, intuition and results from the numerical modeling portion of the present work (see section 2.3.4) show that the findings of Tong et al. (1998) extend to convection in TCs.

There are not many published Doppler radar estimates of LH in TCs. Gamache et al. (1993) used the NOAA WP-3D (P-3) tail radars to calculate the water budget of decaying Hurricane Norbert (1984). Although no LH estimates were calculated, Gamache et al. (1993) showed 3D distributions of condensed water that were retrieved using the steady-state continuity equation for water. An important result from Gamache et al. (1993) was that azimuthal asymmetries accounted for nearly half the net condensation of the storm. In addition, they noted significant departures from saturation in their full 3-D retrievals whereas in the axisymmetric mean, the entire storm was saturated (except in the eye). These results, for a decaying storm, indicate that computing the LH field within the inner-core of TCs is not as simple as taking the product of the upward mass flux and the vertical derivative of the saturation mixing ratio. Whether this result holds for a rapidly intensifying TC will be shown in section 2.3.

In addition to the above observational studies, several investigators have documented considerable sensitivity to numerical model microphysical schemes when simulating TC intensity and structure. McFarquhar et al. (2006) found that choice of microphysics parameterization (including alterations to the condensation scheme) lead to variations in simulated storm intensity by nearly 10 hPa. Uncertainty in graupel characteristics were found to also produce large changes in storm intensity and are likely one of the culprits behind the consistent and significant over prediction of radar reflectivities when compared to observations (McFarquhar et al. 2006; Rogers et al. 2007).

The goal of the first part of this work is to perform a comprehensive, high-resolution, 4D, airborne radar retrieval of the LH of condensation in a rapidly intensifying TC. New additions to existing retrieval methods will be highlighted including detailed error characteristics. Besides providing insight into the TC intensification problem, the LH fields presented in this study may prove useful for the validation of space-based algorithms and provide motivation for future satellite sensors (i.e., Doppler in space).

2.2 Doppler Radar Platforms and Data

The primary remote sensing instrument used in this work is airborne Doppler radar using the NASA EDOP and NOAA P-3 tail (TA) systems. Both platforms operate at essentially the same frequency ~ 10 GHz, yet the geometry and scanning strategies are vastly different. The EDOP has two stationary antennas, one pointed at nadir and the other 33° off-nadir. Measurements from EDOP are taken from the high-altitude (20 km) ER-2 aircraft (able to overfly intense convection) every 0.5 s with a 200 m s^{-1} ground speed providing some of the finest sampling of any current airborne radar (100 m along-track with a typical 37.5 m gate spacing; Heymsfield et al. 1996). The along-track spacing results in significant oversampling of precipitation yielding an effective horizontal resolution between 100 m and the 2.9° beamwidth (i.e. ~ 0.55 km at surface and ~ 0.30 km at 10 km altitude). The main advantage of EDOP is the nadir-viewing geometry that provides direct measurements of the vertical component of Doppler velocities relative to the aircraft and superior resolution when compared to scanning radars. A major disadvantage of EDOP is the inability to retrieve the three components of the wind and 3D features, as the non-scanning beams only measure Doppler velocities along the vertical plane of the aircraft track. In addition, for track headings not aligned along a Cardinal direction, the along-track wind structure is often complicated and difficult to interpret.

The P-3 TA radars have one antenna that scans 360° in a plane perpendicular to the flight track often alternating fore/aft (FAST) look angles. The aircraft typically flies between 3 – 4 km height and does not penetrate convective cores, relying on side-looking views of high reflectivity regions. The along-track sampling of the P-3 TA radar in normal-plane scanning mode and FAST scanning mode is ~ 0.75 km and ~ 1.5 km, respectively with 0.15 km gate spacing (Gamache et al. 1995; Black et al. 1996). Taking into account the 1.9° vertical and 1.35° horizontal beamwidths of the TA antennae and the sampling intervals using FAST, grid resolutions from the P-3s range from 1.5 – 2.0 km in the horizontal to 0.5 – 1.0 km in the vertical (Reasor et al. 2000; Reasor et al. 2009). The main advantage of the P-3s is the ability to provide essential information on 3-D winds through the use of a retrieval technique (Gamache 1997; Gao et al. 1999). In addition, the P-3 database is much more extensive than that from EDOP. However, the relatively coarse resolution of the analyses, the need to solve for the vertical velocity and contamination of much of the boundary layer from ocean surface backscatter are the primary drawbacks of this system.

The EDOP data utilized in this study is compiled from multiple NASA field experiments yielding thirteen samples of deep convection and hot towers in TCs (Heymsfield et al. 2010). The peak vertical velocity of the mean profile was ~13 – 14 m s^{-1} while individual members had values as high as 25 m s^{-1} located at 12 – 14 km in height. Guimond et al. (2010) describes the detailed structure of two hot tower samples from the Heymsfield et al. (2010) population occurring within the eyewall of rapidly intensifying Hurricane Dennis (2005). In the present study, a hot tower is defined as a special class of deep convection: the top five maximum updrafts in the Heymsfield et al. (2010) sample (shown in Fig. 1 along with the mean). See Heymsfield et al. (2010) for more information on these data. The mean of this hot tower sample is considered to represent mature updrafts near peak intensity. Note that this dataset likely represents the highest quality (resolution, direct measurement of vertical Doppler velocity) updraft structure currently available in TCs and deep convection. Further studies of EDOP data in TCs including comparisons to in situ data can be found in Heymsfield et al. (2001).

The P-3 data analyzed here were collected by two aircraft in the core of Eastern Pacific Hurricane Guillermo on 2 August 1997 for ~ 5.5 hours (10 composite periods with ~ 34 minute sampling frequency) coincident with a rapid intensification episode of the storm (Reasor et al. 2009). Weak to moderate vertical wind shear (7 – 8 m s^{-1}) resulted in convection displaced to the downshear left quadrant of storm during this period. Low wavenumber vorticity asymmetries propagating around the vortex were found to excite strong convective bursts that coincided with the greatest intensification (Reasor et al. 2009). Figure 2 shows reflectivity scans from the NOAA P-3 lower fuselage radar (5.3 GHz) at 3 km altitude during ten eyewall penetrations on 2 August. Oscillations in the structure of the reflectivity from asymmetric to more axisymmetric can be seen in Fig. 2 along with the presence of several convective bursts.

The Guillermo dataset is nearly ideal for studying fundamental problems associated with the impacts of deep convection and the role of the asymmetric mode in TC intensification. However, coarse resolution of the Doppler analyses in space and time still limits the interpretation of the basic physics. The storm-centered radar domain is a box extending 120 km on a side with 2 km grid spacing and 20 km in the vertical with 1 km grid spacing. The first level of useful data is at 1 km height due to ocean surface contamination. Guillermo's 3-D wind field was retrieved using a variational approach on a system of equations that includes the radar projection equations, the anelastic mass continuity equation and a Laplacian filter, among others, including boundary conditions for the surface and just above the echo top (Gamache 1997; Gao et al. 1999; Reasor et al.

2009). Regions of the domain that do not have Doppler velocity information (such as portions of the eye) are effectively interpolated/extrapolated from regions where Doppler velocity was observed through a Laplacian filter (Reasor et al. 2009). The radar scanning strategies employed in the Guillermo sampling (Reasor et al. 2009) require a finite time separation between radial wind measurements in order to construct an accurate wind vector. Reasor et al. (2009) found a maximum time separation of ~ 6 min on the edges of the Guillermo Doppler domain and much less in the eyewall region (~ 3 min) indicating small impact on the present analysis, which focuses on the eyewall. The synthesized reflectivity measurements also suffer from this time separation. This radar dataset is used to perform a LH retrieval, described in detail in the next section.

2.3 Latent Heat Retrieval Algorithm

The technique for retrieving LH from airborne Doppler radar is based on the method of Roux (1985) and Roux and Ju (1990). Several advancements in the algorithm are developed and presented below including: (a) analyzing the scheme within the dynamically consistent framework of a numerical model, (b) identifying sensitivities through the use of ancillary data sources and (c) developing a water budget storage term parameterization. In addition, uncertainty estimates for the retrieved heating in Hurricane Guillermo (1997) are presented.

2.3.1 Theory

To prove the efficacy of the retrieval method, output from a non-hydrostatic, full-physics, quasi cloud-resolving model simulation of Hurricane Bonnie (1998) at 2-km horizontal grid spacing (Braun et al. 2006; Braun 2006) is examined. The focus here will be on a one hour period of the simulation where model variables and precipitation budget terms were output every three minutes during a time when the simulated storm was intensifying despite the influence of northwesterly vertical wind shear (Braun et al. 2006). Although the simulated TC does not replicate the real storm, the dynamically consistent nature of the model budgets allows the assessment of the qualitative and, to some degree, quantitative accuracy of the method. Using numerical model output to test observational retrieval methods is typically referred to as an "observing system simulation experiment" or OSSE. Gao et al. (1999) performed an OSSE to test the accuracy of a Doppler radar wind retrieval algorithm and found errors that are consistent with those computed from *in situ* data using a similar retrieval algorithm (Reasor et al. 2009). More real cases are needed to determine if the quantitative aspects of the Gao et al. (1999) results are valid, but the qualitative accuracy appears robust.

The release of the LH of condensation occurs when water vapor changes phase to liquid water, which requires the air to be saturated. However, for strong updrafts, analysis of the vertical momentum equation reveals that local buoyancy from the release of LH must be present to generate significant vertical wind speeds and accelerations (Braun 2002; Eastin et al. 2005). Therefore, an important question is: does a threshold of vertical velocity exist where saturation and the release of LH can be assumed? Figure 3 (courtesy of Matt Eastin) shows 620 updraft cores (defined as convective-scale vertical velocities that exceed 1.0 m s^{-1} for at least 0.5 km) as a function of relative humidity from P-3 flight level (1.5 – 5.5 km altitude) measurements in the eyewall and rainband regions of 14 intense TCs (Eastin et al. 2005). At 5.0 m s^{-1} and below, large variability in relative humidity is observed while above 5.0 m s^{-1}, nearly all updraft cores are saturated. Levels above ~ 5.5 km are not sampled by the aircraft. This data suggests that using a vertical velocity saturation threshold of ~ 5.0 m s^{-1} is reasonable although the sample size is small.

The numerical simulation of Hurricane Bonnie was used to calculate basic statistics on saturated vertical velocities (on a grid point by grid point basis) to compare to the observational data. Over the one hour portion of the simulation analyzed here, approximately 52% of grid points with an updraft were unsaturated with 94% of these coming from values less than 1 m s^{-1}. In addition, approximately 24% of grid points with a downdraft were saturated with a large percentage coming from small magnitudes, similar to the updrafts. More importantly, ~ 92% of grid points with updrafts greater than 5 m s^{-1} were saturated (95,635 out of 104,074 points) which corroborates the observational data shown in Fig. 3. A similar result was found for downdrafts. Based on this data, we conclude that a threshold of $|w|$ > 5 m s^{-1} is reasonable for assuming saturation. Above 5 m s^{-1}, vertical accelerations are dominated by local buoyancy forcing while below 5 m s^{-1} various physical processes may play a role in the evolution such as perturbation pressure gradient forces (that are not generated by heating) and turbulence (Braun 2002; Eastin 2005). This threshold should only be used as a guide as updrafts likely do not obey strict rules, but rather evolve through a continuum. Note that ~ 99% of updrafts were found to be less than or equal to 5 m s^{-1}, which carries the vast majority of the upward mass flux (~ 70 %; Black et al. 1996; Braun 2002). As a result, saturation cannot be assumed for the vast majority of updrafts and a large percentage of the total mass flux, which motivates the need for the determination of saturation through the algorithm described below.

The simplified form of the full model equation for the continuity of total precipitation mass (rain, snow and graupel) can be written in a manner similar to Braun (2006),

$$\frac{\partial \rho q_p}{\partial t} = -\nabla \bullet \left(\rho q_p \vec{u}\right) - \frac{\partial\left(\rho q_p w\right)}{\partial z} + \frac{\partial\left(\rho q_p V_t\right)}{\partial z} + \rho Q_+ - \rho Q_- + \rho D + \rho Z\text{ ,} \tag{1}$$

where ρ is the dry air density, q_p is the total precipitation mixing ratio in kg kg^{-1}, V_t is the hydrometeor fallspeed in m s^{-1}, Q_+ and Q_- are the total precipitation sources and sinks (units of kg kg^{-1} s^{-1}), respectively, D is the diffusive tendency of q_p and Z is an artificial model offset for negative mixing ratios. The horizontal winds ($\vec{u}$) are storm-relative and w is the vertical velocity all in m s^{-1}. Examination of each budget term (see Braun 2006 for a description of some terms) on the convective scale (20 by 15 km horizontal mean centered on strong eyewall convection and single grid points within an eyewall convective cell) revealed that the turbulent diffusion of precipitation and model offset terms were small and can be neglected. These results are consistent with Braun (2006). The reduced form of the continuity equation for total precipitation mass used in this study becomes

$$\frac{\partial \rho q_p}{\partial t} \cong -\nabla \bullet \left(\rho q_p \vec{u}\right) - \frac{\partial \rho q_p \left(w + V_t\right)}{\partial z} + \rho Q_{net}\text{,} \tag{2}$$

where the vertical flux divergence of precipitation and the sedimentation of precipitation terms are combined to yield a vertical Doppler velocity flux divergence of precipitation. In addition, the sources and sinks of precipitation mass are combined into a net precipitation source term (Q_{net}). Although the second term on the right hand side of (2) reduces the error in the budget (avoids estimation of hydrometeor fallspeeds), it can only be used when the radar antenna is positioned in vertical incidence. The P-3 antennae were often positioned in FAST scanning mode during the investigation of Guillermo and thus, the vertical flux divergence term must be separated as shown in (1).

Figure 4 shows a scatter plot of the relationship between Q_{net} and the source of cloud water (condensation, indicating saturation) for model grid points that are producing precipitation between 0 – 10 km height in the first nine minutes (with three minute output) of the one hour simulation period (see Braun 2006 for details of simulation). This subset of data is representative of the entire simulation and includes 828,611 points. A height of 10 km is used as a cap for points in Fig. 4 because the simulation revealed that the source of cloud water ceased at this level in deep convection (see Fig. 5 for an example). The points in Fig. 4 are colored by temperature with red points > 0°C (rain microphysics) and blue points ≤ 0°C (ice microphysics). There is a linear relationship between the two variables in Fig. 4 with ~70 % of the variability (statistic computed for the entire one hour period) in Q_{net} explained by the source of cloud water for all points (rain and ice processes). The dominant mode of precipitation growth shown in Fig. 4 is rain microphysics and the associated collision-coalescence process (Rogers and Yau 1989) with the source of cloud water explaining 87 % of the variance in Q_{net} for rain microphysics (red points) only.

Braun (2006) notes that in the azimuthal mean the source of cloud water in the eyewall is immediately soaked up by precipitating hydrometeors (collision-coalescence process), which is shown here on the grid point scale. The off-linear scatter in Fig. 4 is explained by ice microphysics (blue points) taking over the net production of precipitation. Note that there is some overlap between the red and blue points (mostly near the freezing level) because no discrete threshold for rain/ice microphysics exists. Indeed, observations suggest that super cooled cloud liquid water can exist at altitudes of 12 km in deep convection located in the TC eyewall (Black et al. 2003).

Figure 5 shows an example of the vertical structure of the relationship found between Q_{net} and the source of cloud water for convection in the simulated TC (shown by values averaged over an eyewall convective cell). The source of cloud water matches very well with the net production of precipitation up to 5 – 6 km height (melting zone). Above 6 km height, ice phase microphysics begins contributing to the formation of precipitation. A similar vertical structure was found for many other locations in the numerical simulation of Hurricane Bonnie.

In summary, Figs. 4 and 5 demonstrate that by solving for Q_{net} in (2) and determining where $Q_{net} > 0$ (net production of precipitation), we are able to distinguish where the air is saturated, which is required before the release of LH can take place. Intuition on the possible microphysical sources of precipitation (Rogers and Yau 1989) suggests that this is also true of TCs in nature. Note that equations (1) and (2) and the association of $Q_{net} > 0$ with saturation are valid *instantaneously*. That is, assuming information on the water content and winds are available quasi-instantaneously, the saturation state of the air and the associated magnitude of the LH release (described below) can be determined at the same time. Therefore, by using the signal radar responds to (precipitating hydrometeors for 10 GHz) information on the saturation state (and LH release) at each grid point in the 3-D Doppler domain can be retrieved.

There are errors in this interpretation in mixed phase regions of convection and for small values of Q_{net} which could occur near cloud boundaries, for example. When applying the theory to radar observations, instrument errors are also possible due to resolution, non-homogeneous beam filling, attenuation and calibration of the beam. Another source of error is the time separation between radar beam intersections discussed in section 2.2 that violates the instantaneous assumption. However, the algorithm presented here is somewhat insensitive to these errors because information is only required on the *condition* of saturation, not the *magnitude* of that saturation. Using the steady state assumption to solve for Q_{net} in (2) is probably a larger problem with the current retrieval algorithm than those discussed above. Relying on Q_{net} for quantitative purposes (such as computing the LH magnitude) can be dangerous due to the large uncertainty in single frequency radar derived water parameters (see introduction; Gamache et al. 1993), including substantial errors in proportionality. We focus on the qualitative nature of Q_{net} to reduce the consequences of these errors, although dualfrequency radars show promise for quantitative retrievals of Q_{net} in the future. With the P-3 radar used in this study, substantially reduced errors in the LH magnitude can be achieved by using the radar estimates of vertical velocity rather than Q_{net}.

Once the saturation state is determined, the magnitude of the LH can be calculated according to the entropy form of the first law of thermodynamics,

$$C_p \frac{D \ln \theta}{Dt} = \frac{J}{T} \tag{3}$$

where C_p is the specific heat of dry air at constant pressure (1004 J K^{-1} kg^{-1}), θ is potential temperature in K, T is temperature in K and D / Dt is the material derivative. The entropy term in (3) takes the form $J = -L_c \frac{Dq_s}{Dt}$ with L_c the LH of condensation at 0 °C (2.50×10^6 J kg^{-1}) and q_s is the saturation mixing ratio in kg kg^{-1}. The material rate of change of the saturation mixing ratio, which is a function of temperature and pressure, is dominated by the vertical advection yielding an approximate expression for the entropy term, $J \cong -L_c w \frac{\partial q_s}{\partial z}$. Note that other diabatic contributions to the energy budget such as radiative effects have been neglected. Plugging the approximate entropy term into (3) and rearranging gives the expression used to calculate the magnitude of the LH release

$$\frac{D\theta}{Dt} \cong \frac{-L_c \theta}{C_p T} w \frac{\partial q_s}{\partial z}. \tag{4}$$

Note that this method provides information on the LH of condensation/evaporation only and does not include mixed phase processes. However, as mentioned in the introduction, the overwhelming contribution to the total LH and energy budget in convection comes from warm rain processes (Tong et al. 1998; Zhang et al. 2002).

Figure 6 presents a flowchart summarizing the main steps in the LH retrieval algorithm described above. Imagine that the P-3 TA radar samples some precipitation in Guillermo at the analysis resolution stated in section 2.2. The two main steps are: (a) determine where heat is released by solving equation (2) for the net production of precipitation (Q_{net}) and identify regions where $Q_{net} > 0$ (saturation) and (b) compute the magnitude of the LH release using equation (4).

Previous studies employing a form of the retrieval method outlined above have been unable to calculate the storage term in (2) due to inadequate Doppler radar sampling and thus, assumed the system or the clouds were in a steady state (Roux 1985; Roux and Ju 1990; Gamache et al. 1993). Clouds, and the entire lifecycle of TCs, are not steady state and significant error can be expected if using this assumption (Gamache 1993), especially on a local scale. The Guillermo dataset is unique in that composite Doppler radar sampling was completed on average every 34 minutes allowing estimation of the storage term. However, it was found that using a 34 minute time increment for computing the storage term added no more information (order of magnitude smaller than other terms) to the precipitation budget than using the steady state assumption. This result is not surprising considering the lifecycle of a cloud is on the order of 30 minutes (Houze 1993).

Figure 7 shows sensitivity tests using a storage term parameterization (described below) revealing large changes to the azimuthal mean heating in Guillermo relative to the steady state case. Differences of ~ 20 % at mid-levels to over 100 % at lower (3 km) and upper (10 km) levels highlights the significant impact the storage term can have on LH computations. The storage term values produced through the parameterization are very similar to those calculated from ground-based radar (refresh time of ~5 minutes) and P-3 LF radar (refresh time of 30 s) observations of mature TCs.

The parameterization of the storage term was derived using output from the Bonnie numerical simulation. For those grid points that were producing precipitation, a linear relationship between the total horizontal advective flux of precipitation (largest contribution from tangential component) and the storage of precipitation was found (Fig. 8). Note that Fig. 8 only includes data at one snapshot while the linear fit used for computation ($R^2 = 0.78$),

$$\frac{\partial \rho q_p}{\partial t} = 0.802 \times \left[-\nabla \bullet \left(\rho q_p \vec{u} \right) \right] \qquad (5)^1$$

represents the average of the fits at three minute intervals over one hour. Note, that the

---

[1] It was found that using the terms multiplied by density produced a slightly better fit, explaining an extra 7% of the variance.

strong relationship in (5) does not mean that the saturation signal (Q_{net}) is a small residual and therefore prone to large error. The magnitude of Q_{net} relative to other terms in (2) was analyzed on the grid point scale as well as for spatial and temporal averages in various convective and stratiform regions and was found to have a significant signal relative to the other terms. Physically, the relationship in (5) can be understood by the fact that the strong tangential winds and associated advective transport of precipitation in mature TCs controls the storage of precipitation to a large degree (a consequence of the divergence theorem). This relationship indicates that morphing (Wimmers and Velden 2007) the radar reflectivity and derived precipitation fields using the Doppler wind analyses to generate a storage term tendency shows promise.

Figure 9 shows that using the storage term parameterization in (5) reduces the root mean square error (RMSE) in Q_{net} by more than a factor of two relative to the steady state case. This result can also be expressed in terms of a cylindrical volume integrated error,

$$\mathit{Error} = \frac{\left| \int_0^z \int_0^r \overline{X^P} 2\pi r dr dz - \int_0^z \int_0^r \overline{X^O} 2\pi r dr dz \right|}{\int_0^z \int_0^r \overline{X^O} 2\pi r dr dz} \tag{6}$$

where $\overline{X^P}$ is the azimuthal mean of the predicted variable (in this case, calculating Q_{net} different ways), $\overline{X^O}$ is the azimuthal mean of the observed variable (in this case, Q_{net} output directly from the model) and *r* and *z* are the chosen outer (200 km) and upper (17 km) boundaries of the domain, respectively. Figure 10 depicts a time series of (6) for Q_{net} revealing that in the temporal mean, the storage term parameterization reduces the error in Q_{net} by ~ 16 % with improvements of nearly 30 % at various times using the numerical model output. Also shown in Figs. 9 and 10 is the error from using the approximate form of the precipitation continuity equation in (2) with (1) serving as the control for all cases. The errors in using (2) are low, which is consistent with the scale analysis already discussed.

To summarize so far, Q_{net} has been shown to be a very good proxy for saturation in a numerical setting. In addition, using the reduced form of the precipitation continuity equation with a parameterization for the storage term has been shown to provide a good diagnosis of the actual Q_{net} output from the model. An obvious question is: what is the impact of these approximations on the derived heating?

Figure 11 shows the errors (according to equation 6) in releasing heat as a result of using the approximations stated above in determining saturation at each grid point. The control is computed by releasing heat at grid points that are producing cloud water, which is required for air to be saturated. Note that latent heating rates computed from the model's microphysical scheme were not available, so the diagnostic heating rate (considering updrafts only) in (4) was used instead. Differences between the heating rates should be small and the expression in (4) is currently the only practical way to compute heating rates from radar observations. Sensitivity tests and error analyses of the diagnostic heating expression in (4) are detailed in the next section. The temporal mean error in Fig. 11 is ~8% with ~93% of the variance in the azimuthal mean heating explained by the retrieval method. Errors computed using both updrafts and downdrafts showed similar results albeit with a weaker explained variance (~87%). These OSSE results, including the ones described above, indicate that the method for determining saturation in the LH retrieval is reasonable. Validating this result using observations is difficult because of the lack of in situ data over the large swaths sampled by the radar. Using a combination of flight level data and dropsondes offers the best avenue for validation and is left for future work.

2.3.2 Applying the theory to observations

To compute saturation (Q_{net}) from Doppler radar, the total precipitation mixing ratio must be known. In order to derive this quantity, in situ cloud particle data collected by NOAA P-3 aircraft at ~ 4 km altitude in the intense stages of Hurricane Katrina (2005) was analyzed. The cloud particle data was averaged over a period of 6 s in an attempt to match the sampling volumes of the particle probe and Doppler radar pulses (Robert Black, personal communication). Using the cloud particle data, radar reflectivity factor

(Z) and liquid water content (LWC) were computed and the coefficients (A and B) of the power law ($Z = A \times LWC^{B}$) were determined. Figure 12 shows a scatter plot (~ 7,000 data points) of the relationship between reflectivity factor (expressed in dBZ) and LWC for the Katrina data. The red line shows the best fit ($Z = 402 \times LWC^{1.47}$) with a correlation coefficient of 0.88 while the blue lines depict the 95% confidence interval, which gets larger with higher reflectivities (partly due to sampling). The relationship $Z = 402 \times LWC^{1.47}$ was used below the melting layer while the ice water content (IWC) parameterization $Z = 670 \times IWC^{1.79}$ (Black 1990) was used above the melting layer with linear interpolation of the two expressions within the melting layer.

Note that relationships between radar reflectivity factor and water content parameters are not unique and therefore, uncertainty in Q_{net} will exist. As mentioned in the previous section, however, the algorithm presented here is *somewhat* insensitive to these errors because information is only required on the condition of saturation, not the magnitude of saturation. Equation (2) was solved for Q_{net} using the Guillermo dual-Doppler analyses, the storage term parameterization in (5), the computed precipitation mixing ratios described above and hydrometeor fall speed relations for a gamma distribution (Ulbrich and Chilson 1994; Heymsfield et al. 1999). Based on Fig. 3 and the discussion in the previous section, grid points with $|w| > 5$ m s^{-1} are assumed saturated.

To compute the magnitude of LH released at saturated grid points in the radar domain, knowledge of the thermodynamic structure of convective cells is required, which is very difficult to obtain. To approximate the thermodynamic structure, a composite high-altitude (using NASA aircraft that fly at altitudes of 10 and 20 km) dropsonde representative of eyewall convection in TCs is utilized. The storms sampled were: Hurricane Bonnie (1998), Tropical Storm Chantal (2001), Hurricane Gabrielle (2001), Hurricane Erin (2001) and Hurricane Humberto (2001) yielding ten independent thermodynamic profiles of eyewall convection. The sampling of eyewall convection is verified using winds and relative humidity from the dropsondes as well as satellite observations. Discussion on the uncertainty associated with using a composite dropsonde is discussed in the next section. To complete the LH calculation, the vertical velocities derived from the dual-Doppler radar synthesis procedure are input to equation (4). The

LH of condensation is capped at 10 km altitude based on numerical simulation experiments and the structure of the cloud water source shown in Fig. 5.

Figure 13 displays two examples of the derived LH field in Guillermo showing the 3D structure (+/- 100 K h^{-1} isosurface) of deep convection. Figure 13a (valid at 1855 UTC 2 August 1997) shows a pronounced asymmetric distribution of LH in the down-shear quadrants of the storm as a result of persistent vertical shear forcing (Reasor et al. 2009). Almost 3.5 h later at 2225 UTC, Fig. 13b shows the emergence of large, individual pulses of LH, which are embedded within low-wavenumber vorticity asymmetries rotating around the eyewall of Guillermo (Reasor et al. 2009). The full observational period (~ 5.5 h) of the LH retrievals are used as time-dependent forcing in a non-linear numerical model in order to examine their impacts on numerically simulated intensity and structure change (see section 2.3.4).

Figure 14 shows the LH profile computed using the mean EDOP vertical velocity data presented in Fig. 1 and the composite thermodynamic data discussed above. Almost the entire mean profile in Fig. 1 was greater than 5 m s^{-1} and therefore, saturation was assumed. The mean EDOP LH profile is shown because of the high quality of the data (very high resolution and direct measurement of vertical Doppler velocities relative to the aircraft). The profile in Fig. 14 will be used to understand the dynamic response of a realistic TC vortex to observational heating perturbations in a future study.

2.3.3 Uncertainty estimates

Uncertainty is inherent to all observations and thus, it is essential to characterize these errors to provide a thorough product that can be used by the community. There are two main calculations in the LH retrieval that require error analysis: the computation of the saturation state and the magnitude of the LH. The approximate errors associated with determining saturation were analyzed in section 2.3.1 and thus, the focus here is on the magnitude of the LH fields. The magnitude of the LH is essentially a function of thermodynamic information (temperature and pressure) and vertical velocity. The uncertainty in the thermodynamic information is assessed by first gathering soundings from various regions (eyewall and environment) of the numerical simulation of Hurricane Bonnie and eyewall dropsonde observations in several storms (see section 2.3.2 for the list of TCs). These thermodynamic profiles are then input to equation (3) revealing differences in the peak LH of only ~ 10 – 15 %. These results indicate that the magnitude of the LH is not very sensitive to the details of the thermodynamic information in the eyewall of TCs.

Sensitivity to the vertical velocity is much greater and is the most important parameter in the estimation of LH. Reasor et al. (2009) compared the Guillermo Doppler radar analyzed vertical velocities to flight-level *in situ* measurements and found a RMSE of 1.56 m s^{-1} in the eyewall region with a relatively weak correlation coefficient (0.61) compared to the horizontal wind components. Morrow (2008) compared a large set of P-3 derived wind fields with flight-level wind measurements, including those from Guillermo, and found that overall the intense and wide updrafts were captured well by the Doppler analysis while those that were narrow and weaker were not well represented. This result extends to downdrafts as well (Morrow 2008; Reasor et al. 2009)

Figure 15 (from Morrow 2008) shows a representative comparison of flight-level vertical velocities (at ~3 km altitude) to those computed from the Doppler analysis valid at ~ 2002 UTC 2 August 1997 in Hurricane Guillermo. The strong, wide updraft pulse at 30 km radius is represented well by the Doppler analysis as are the general patterns of the vertical velocity field, but the narrow updrafts/downdrafts are clearly not captured. These errors are likely a result of: (1) inadequate matching of the radar and flight-level sampling volumes and resolutions and (2) the need to use the anelastic mass continuity equation (more specifically, divergence) to solve for the vertical velocity. For the 2 km horizontal resolution of the Guillermo dataset (which relies heavily on FAST), the vertical velocity is estimated by computing divergence from data over an area of 16 km^2, which effectively filters out smaller scale perturbations (Marks et al. 1992). In addition, surface contamination does not allow adequate computation of divergence in the boundary layer, which will lead to errors in the vertical velocity aloft.

The random error in the LH magnitudes can be estimated through an error propagation analysis. The general formula for error propagation is

$$\delta q^2 = \sum_i \left(\frac{\partial q}{\partial x_i} \delta x_i \right)^2 , \tag{7}$$

where δq represents the Gaussian uncertainty in q (a function of x_i), and each x_i denotes a variable with associated uncertainty δx_i, that contributes to the calculation of δq. Applying (7) to equation (4) yields

$$\delta^2_{D\theta/Dt} = \left(\frac{-L_c}{C_p}\right)^2 \left[\left(\frac{w}{T}\frac{\partial q_s}{\partial z}\delta_\theta\right)^2 + \left(\frac{\theta}{T}\frac{\partial q_s}{\partial z}\delta_w\right)^2 + \left(\frac{-\theta}{T^2}w\frac{\partial q_s}{\partial z}\delta_T\right)^2 + \left(\frac{\theta}{T}w\delta_{\partial q_s/\partial z}\right)^2\right]. \quad (8)$$

The uncertainties in each variable in (8) are determined from standard deviations in the dropsonde data described in section 2.3.2 and the RMSEs in vertical velocity from the Reasor et al. (2009) study: $\delta_T = 2.5\ \mathrm{K}$, $\delta_\theta = 3.1\ \mathrm{K}$, $\delta_{\partial q_s/\partial z} = 3.4\times10^{-7}\ \mathrm{m}^{-1}$ and $\delta_w = 1.56\ \mathrm{m\ s}^{-1}$. For all other variables in (8), characteristic values for the TC eyewall were chosen: $T = 300\ \mathrm{K}$, $\theta = 302\ \mathrm{K}$, $\frac{\partial q_s}{\partial z} = -4\times10^{-6}\ \mathrm{m}^{-1}$ and $w = 5\ \mathrm{m\ s}^{-1}$. The second term on the right-hand-side of (8) is larger than the other terms by at least an order of magnitude. Using this information and expressing the uncertainty in the LH magnitude as a percentage ($U_{D\theta/Dt}$) yields the following simplified equation

$$U_{D\theta/Dt} \cong \left|\frac{\delta w}{w}\right| \times 100. \quad (9)$$

Plugging in the characteristic values chosen above and assuming the RMSEs computed in Reasor et al. (2009) are representative of a spectrum of vertical velocities, the uncertainty in the LH magnitudes for updrafts of 5 m s^{-1} is ~ 32 %. For smaller vertical velocities the errors can be large: a 1 m s^{-1} updraft has an uncertainty in LH magnitude of ~ 156 %. The errors in the LH magnitudes are dominated by random errors, although a slight positive bias of 0.16 m s^{-1} in the eyewall vertical velocities was found by Reasor et al. (2009), indicating that the LH retrievals may release too much heat on average. However, when combining the biases in the LH magnitudes and structure (through the calculation of saturation), the sign of the total bias in the retrievals is not clear although it is small compared to the random errors. Section 2.3.4 will attempt to address this issue by analyzing the ability of the LH fields to reproduce the observed wind speeds of Guillermo using a numerical model.

The discussion above estimates the uncertainties with computing LH release. Another source of uncertainty is discovered by asking the question: how well does the

Guillermo dataset represent a larger distribution of convection and LH in TCs? This type of error is referred to as a sampling uncertainty. The updrafts (and LH) in Guillermo were log-normally distributed as are most TCs (Black et al. 1996) and require more advanced statistics than those of Gaussian distributions to describe their sampling uncertainties. We are interested in the sampling errors associated with deep convection and therefore, a subset of the LH field is selected for statistical analysis (vertical velocities greater than 5 m s^{-1}) shown in the histogram in Fig. 16.

In order to estimate the sampling uncertainty in the mean value of this subset (117 K h^{-1}), a Monte Carlo based method called the "bootstrap" was utilized. Estimation of the uncertainty in the mean (including the bootstrap method) is sensitive to the degrees of freedom in the dataset. To estimate the degrees of freedom in the LH field over the full 3-D domain and for all ten composite periods, a combination of statistical (auto-lag correlation) and physical reasoning was employed. An auto-lag analysis in time reveals that each grid point in the Doppler domain has a time scale for independence of about 30 minutes (convective lifetime), while one degree of freedom in the vertical was assumed to represent a column of the atmosphere. An auto-lag analysis in the horizontal directions through deep convective cells revealed an independent spatial scale of ~ 12 km in each direction (approximate deep convective cell size in P-3 data). The number of degrees of freedom (DOF) is then calculated as

$$DOF = \frac{T_x T_y T_z T_t}{I_x I_y I_z I_t}\alpha \ , \qquad (10)$$

where T_i are the number of grid points in a dimension, I_i are the length and time scales for independence in each dimension, and α is the percentage of the total sample being considered (3% for vertical velocities greater than 5 m s^{-1}). Using the scales discussed above along with (10), 30 degrees of freedom (or independent deep convective cells) were found in the Guillermo radar dataset.

The bootstrap was performed through the following two steps. First, a random number generator with a discrete uniform distribution was used to create 1000 perturbed LH datasets each with a sample size of 30 (degrees of freedom) from the observed distribution shown in Fig. 16. Second, averages were computed for each dataset and they were sorted in ascending order. Using the sorted data, the 25th and 975th values were selected yielding the 95% confidence interval for the mean LH rate in the observed distribution (117 K h^{-1}; Fig. 16) of 101 – 133 K h^{-1} (or 14 %). This sampling uncertainty is lower than the standard uncertainty found for updrafts of 5 m s^{-1} (~ 32 %) because of the distribution of data considered in the sampling case (updrafts > 5 m s^{-1}). Plugging the maximum updraft analyzed in the Guillermo P-3 dataset (~ 30 m s^{-1}) into (9) along with the approximate uncertainty of 1.56 m s^{-1} yields an error of ~ 5 %. Averaging this 5 % error value with that for a 5 m s^{-1} updraft (32 %) yields a mean error of 18.5 %, which is close to the sampling uncertainty.

2.3.5 Impacts on numerical predictions

The real test of the usefulness of the LH retrievals comes from an analysis of their impacts on the predicted intensity and structure of TCs. To this end, the Guillermo LH retrievals were used as forcing in a nonlinear numerical model to examine their impacts on the simulated intensity and structure change of the storm relative to a case that relies on the model's microphysical scheme for forcing. The HIgh GRADient (HIGRAD) applications model developed at the Los Alamos National Laboratory (LANL) was used to simulate the rapidly intensifying period of Guillermo sampled by the P-3 aircraft. Only basic information on the model is presented here as a more detailed explanation of the model is given in the next chapter. The HIGRAD model solves the 3D, rotating, compressible Navier-Stokes equations written in conservative form and framed in generalized coordinates (Reisner et al. 2005). For the simulations described here, a full stress tensor along with an eddy diffusivity scheme based on the grid spacing (see section 3.2.1) was used to represent both surface friction and diffusive tendencies associated with sub-grid scale fluxes. The cloud microphysical model is described in the appendix of Reisner and Jeffery (2009).

The setup of HIGRAD is as follows. The model domain extends 1,276 km on a side with a 120 km square region in the center with constant 2 km horizontal resolution (matching the Doppler analysis domain) stretching to ~15 km horizontal resolution at the boundaries using a differentiable hyperbolic tangent function. The first model level is centered at 35 m above the ocean surface and stretches to 22 km at the model top (71 total levels). The environmental potential temperature, density and water vapor initial conditions are taken from 1.125° European Centre for Medium-Range Weather Forecasts (ECMWF) operational analyses closest in time to the start of the aircraft observations of Guillermo (1855 UTC 2 August 1997). Newtonian relaxation zones on the sides and top of the model domain were used to nudge the fields back towards the ECMWF environmental conditions and control the reflection of wave oscillations into the domain interior. A full Coriolis force was used with the domain center at a latitude of 22°N (center of Guillermo at start of aircraft penetrations). A high-resolution (0.25°, daily) sea surface temperature dataset that relies on passive microwave satellite data (Reynolds et al. 2007) was used to initialize the ocean. Finally, a time step of two seconds was used for all simulations.

The initial vortex is taken directly from the first Doppler radar composite of Guillermo (1855 UTC 2 August 1997). This vortex only covers the inner portion of the model domain and therefore an extended Doppler vortex was created according to the following procedure. First, the Doppler winds are interpolated to a cylindrical grid extending out to the edge of the model grid with 2 km radial spacing and 72 azimuthal points. Next, the ECMWF analyses are used to compute the environmental, horizontal winds impacting Guillermo by averaging in annuli around the model depicted storm out to 500 km radius with large weight given to outer radii and small weight given to inner radii. This procedure effectively removes the symmetric part of the vortex from the model (Hanley et al. 2001). The outer radius of the cylindrical grid is then set to the computed environmental winds and a smooth exponential decay function is used to merge the edge of the Doppler domain into the environmental winds at each radial. Finally, the merged winds are interpolated to the model Cartesian grid. Figure 17 shows the 3D wind speed structure of the merged vortex on a subset of the full model grid (500 km on each side, but still 22 km in the vertical). Figure 18 shows a horizontal cross section through the merged vortex at ~1 km altitude on the full model grid for reference. The above procedure is able to retain the important asymmetric structure of the observed vortex in the interior while gradually relaxing the winds back to the environment on the domain boundaries.

The vortex is introduced into the model using a dynamic initialization procedure where forcing terms are added to the horizontal momentum equations,

$$\frac{Du_i\rho}{Dt} = \mathbf{F}_\mathbf{i} + G\left(u_i^o - u_i\right)\rho \ . \qquad (11)$$

The $\mathbf{F}_\mathbf{i}$ represents all the standard forcings on the right-hand-side of the horizontal momentum equations, u_i^o the horizontal winds from the merged vortex and G the chosen nudging coefficient of $10^{-3}\ \mathrm{s}^{-1}$. The dynamic initialization (or "nudging") procedure has been used successfully for over thirty years (e.g. Hoke and Anthes 1976) including studies of tropical cyclones (Chang 1981; Krishnamurti et al. 1998; Tory et al. 2006). The goal of the process is to develop a set of initial conditions based on observations that are balanced with respect to the full model equations. Several other methods exist for vortex initialization such as 3D and 4D variational approaches (e.g. Navon et al. 1992). We chose the nudging method for both its simplicity and effectiveness.

In this study, only the merged Guillermo vortex (Figs. 17 and 18) is nudged into the model as described above, allowing the other model variables (such as vertical velocity, potential temperature, density and water vapor) to develop in a consistent and balanced manner. The nudging coefficient was chosen by trial-and-error which is not without precedent (Krishnamurti et al. 1998) although more sophisticated methods have been used (Zou et al. 1992). Using too large of a coefficient produced large amplitude gravity wave oscillations along with a perpetually unbalanced mass and momentum field. On the flip side, using too small of a value did not provide enough forcing to spin-up a balanced vortex in a reasonable amount of time. A value of $10^{-3}\ \mathrm{s}^{-1}$ seemed to provide a good compromise between these two effects. Note that nudging different variables with a different observational dataset and especially with a different numerical model and setup will likely change the optimal coefficient (Hoke and Anthes 1976; Zou et al. 1992).

The model is integrated using (11) for a period of 10 h at which time the vortex reached a steady-state minimum pressure of ~ 958 hPa, which matches observations of the storm at this time (Mayfield 1997). Note that during the initialization, the model microphysical scheme is enabled, but the forcing associated with heat released from phase changes is set to zero. This allows consistency between the spun-up vortex and the moisture field while not allowing heat release that would change the wind field from that which was specified. Figure 19 shows a time series of minimum pressure for the dynamic initialization of the merged Guillermo vortex. After a period of ~ 2 h, the minimum pressure begins to asymptote towards the observed value of ~ 958 hPa. An offline, iterative thermal wind balance solver using the symmetric part of the merged vortex and an ECMWF environmental sounding as input revealed that the model is approaching thermal wind balance which, in terms of minimum pressure, is ~ 958 hPa for this vortex. The dynamic initialization is stopped at 9 h and the nudging coefficient is set to zero. At this time, nearly the exact structure of the merged vortex (Figs. 17 and 18) exists in the model along with the potential temperature and density fields that hold the vortex in quasi thermal wind balance.

After the nudging is stopped at 9 h, four simulations are spawned. In the first simulation, the retrievals discussed in the preceding section are used as forcing in the thermodynamic equation,

$$\frac{D\theta\rho}{Dt} = \mathbf{F} + F_{LH}\rho f(t) \tag{12}$$

where the $\mathbf{F}$ represents only the diffusive tendencies on θ (the release of heat through the model's microphysical scheme was shut off for this run), which includes sensible heat fluxes from the ocean surface and F_{LH} is the forcing from the LH retrievals. The variable $f(t)$ represents the time evolution of the LH forcing, which over the first ten minutes takes the form

$$f(t) = \left(1 - \tanh\left(\frac{\tau + 1}{\alpha}\right)\right) \tag{13}$$

with $\tau = 600 - t$ a time scale over a ten minute period and $\alpha = 300$. The function in (13) acts to smoothly ramp up the first snapshot of LH with an exponential increase in ten minutes. After the ten minute ramping period, the function in (13) is replaced by a linear interpolation operator that transitions each LH snapshot over a 35 minute period (commensurate with the model time step of 2 s) extending out to 5.25 h. This simulation will be called the "retrieval" run.

The second simulation is very similar to the first one except that every grid point in the Doppler radar domain is assumed saturated in the LH retrieval (which releases all heating/cooling) instead of computing the saturation state. This simulation will be called the "saturated" run.

In the third simulation, the LH retrievals are not used, but the heating produced through the model's microphysical scheme is turned on instead, which can be represented through the bold forcing variable shown in (12). Only warm rain processes were considered in this simulation as sensitivity tests with mixed phase microphysics revealed small differences in wind speed magnitude and structure (not shown) relative to the moist phase only results. This is consistent with the modeling results of Zhang et al. (2002).

The microphysical scheme relies on the water vapor field to release energy. Although a water vapor field consistent with Guillermo's vortex was produced during the dynamic initialization process, this moisture field is only representative of the basic-state (vortex) and not the perturbations (convection). Figure 20 shows a horizontal cross section of the water vapor mixing ratio at 5 km height after 9 h of vortex nudging revealing a relatively featureless field with fairly low values throughout the domain. In order to assist the microphysics scheme with the placement and magnitude of water vapor that would result in the observed convection, the first LH retrieval snapshot (a condensation rate; Fig. 13a) is converted to a cloud water tendency using the expression

$$Fq_c = \frac{F_{LH} T C_p}{\theta L_c C_{\lim}}, \tag{14}$$

where Fq_c is cloud water mixing ratio tendency in kg kg^{-1} s^{-1} and $C_{\lim}$ represents dimensionless constants used to scale the microphysical terms in order to keep the values well-behaved for numerical accuracy (Reisner and Jeffery 2009). These constants were cut in half initially to allow for stronger forcing. The converted cloud water was then assumed to have originated as a source of water vapor (from turbulent fluxes at the air-sea interface). This source of water vapor was added as a forcing term to the water vapor and mass continuity equations in the model over a ten minute period using the time evolution shown in (13).

Figure 21 shows the water vapor field at 5 km height after the dynamic initialization and the ten minute moisture forcing. The moisture field in Fig. 21 is clearly more realistic than that in Fig. 20, showing an asymmetric distribution of water vapor that is consistent with observed convection at this time (see Fig. 2 pass 1 and Fig. 13a). After ten minutes, the water vapor forcing is shut off and the model is allowed to run in a mode free from observational forcing with the microphysical scheme determining the release of heat. The model has no preference on where heat is released in the domain. Therefore, in order to enable fair comparisons with the retrieval run, the heating in the current simulation was only released over the Doppler domain. This was accomplished by multiplying the microphysical heating, represented by the bold term in (12), by an array that masks the outer portions of the domain. We call this third simulation the "freemode" run.

Finally, in the fourth simulation, no LH forcing or moisture forcing of any kind is considered with only the diffusive tendencies active on the right-hand-side of (12). This simulation is called the "unforced" run. A summary of the four simulations described above can be found in Table 1.

After the ten minute forcing period each simulation is run out to 6 h but only data up to 5.25 h (with output every 35 minutes to approximate the Doppler composite time separation) is used for comparisons to observations. Figure 22 provides an overview of the performance of each simulation in terms of minimum surface pressure along with observations during the aircraft sampling (see Zou et al. 2010) at the times noted in Fig. 2. At the beginning of the time series, every simulation experienced a roughly 0.5 h period of slight weakening, which is probably due to minor adjustments of the spun-up vortex. As expected, the unforced run is much too weak but it serves as a control to identify the impact of the various forcing experiments. The freemode run is also too weak with a roughly steady state predicted from ~ 2 h until the end of the simulation. The retrieval run performed quite well capturing most of the observed deepening of Guillermo with a difference of only two hPa at the end of the simulation. However, on average the retrieval simulation was a bit too strong possibly due to errors in the vertical velocity (see previous section) and the computation of saturation. The saturated run, which releases all the heat in the Doppler domain, is clearly too strong indicating that the inner-core of Guillermo may not have been completely saturated.

Comparisons are not made with the maximum wind speeds for two reasons: (1) the maximum wind speed is typically a volatile parameter that can reflect the chaos inherent in a single deterministic forecast rendering comparisons uncertain and (2) the maximum wind speeds in the Guillermo Doppler analyses exhibited small variability (see Fig. 1b of Zou et al. 2010) despite the observed rapid pressure falls during this time period. It is possible that the Doppler analyses are not resolving the peak wind due to resolution in space and time, smoothing and surface clutter. It is also possible that the mass-momentum adjustment process is lagging during the observational sampling period. To avoid some of these uncertainties, we focus on mean and integrated measures of error.

Since the first Doppler wind composite was used to spin-up Guillermo, comparisons of the model generated wind fields to observations are made with the other nine composite periods every 35 minutes out to 5.25 h as discussed above. The storm moves during the simulation, so in post-processing the model vortex is re-centered in the domain using a wind centroid finder that minimizes the azimuthal variance of the wind speed. The data are then interpolated from the model grid to the Doppler analysis grid.

Figure 23 shows the results of volume integrated wind speed errors (model vs. Doppler radar) computed very similar to (6) only azimuthal averages were not computed and the integrations were done over the Cartesian Doppler volume rather than a cylindrical volume. The errors are shown for all ten aircraft composite periods (see Fig. 2) with 0 h representing Guillermo's spun-up vortex. Several things are worth noting from Fig. 23. The first result is that omitting observational forcing of any kind (the unforced case) grossly under predicts the Doppler winds. Although this is obvious, it serves as a control case to identify the impact of various forcings. Second, the saturated case shows that assuming saturation of the entire inner-core of Hurricane Guillermo is invalid as the generated wind speeds are much too large, especially at later times. This is consistent with the minimum surface pressure shown in Fig. 22. As mentioned in section 2.3.1, the vast majority of the total upward mass flux in TCs comes from updrafts less than 5 m s^{-1}, many of which were shown to be unsaturated. It is clear that determining the saturation state of weak to moderate updrafts (and downdrafts) is important in accurately retrieving the LH field in TCs. For stronger updrafts, however, saturation can likely be assumed. Based on the analysis in the previous section, a threshold of 5 m s^{-1} is suggested for determining the saturation state.

The last interesting result from Fig. 23 is that the freemode run and the retrieval run are very similar in terms of volume integrated wind speed errors. The winds generated from the retrieval run are a bit too strong with possible error sources from the accuracy of the Doppler derived vertical velocities to the determination of the saturation state (tendency parameterization, reflectivity derived parameters, etc). Conversely, the winds generated from the freemode run are a bit too weak potentially due to uncertainties in the microphysics scheme among others. These results are generally consistent with Fig. 22 although the freemode run appears much weaker in terms of minimum surface pressure than in terms of integrated wind speed.

Figure 24 shows a time series of the RMSEs for the four simulations. The RMSEs were computed for each horizontal wind component first and then the wind speed was calculated. The reason why there is non-zero error at 0 h is because during the dynamic initialization process, the specified wind field must come into balance with the full model equations. The full model equations include the effects of effective diffusion (from both the sub-grid model and numerical approximations to the nonlinear terms), which will alter the wind field albeit not by a large amount. Errors in the model wind field grow quickly during each simulation with the unforced and saturated simulations having the largest errors at the end of the 5.25 h period. Between 2 – 3 h, all simulations have generally increasing error trends while those associated with the retrieval run stay fairly steady producing the smallest values (~ 7.5 m s^{-1}) at the end of the period.

Figure 25 presents a time series of the square of the linear correlation coefficient, which measures how well the simulations capture the variability in the Doppler observations. The simulations that use a form of the LH retrievals ("retrievals" and "saturated" runs) have the largest R^2 values with the experiment that solves for the saturation state explaining slightly more of the variance. By around 3.5 – 4.0 h into the simulations, a bifurcation occurs and the retrievals and saturated runs explain an extra 20% of the variance in the Doppler observations at the end of the 5.25 h period. This result shows that using the LH retrievals can account for a significantly larger percentage of the variability in the observations relative to using the model microphysical scheme.

Why does the retrieval run explain more of the variance in the Doppler observations? The answer to this question lies in the structure of the eye/eyewall region. Figures 26 - 28 show comparisons of the wind speed structure from the retrieval and freemode simulations relative to the corresponding Doppler analysis composite for the last three observation periods: Fig. 26 (2258 UTC 2 August 1997; corresponds to 4.08 h into simulations), Fig. 27 (2333 UTC 2 August 1997; corresponds to 4.67 h into simulations) and Fig. 28 (2404 UTC 2 August 1997; corresponds to 5.25 h into simulations). In terms of predicted wind magnitude, the retrieval run is too strong and the freemode run is too weak which is consistent with Figs. 22 and 23. In terms of predicted wind structure (placement of eyewall, variance in azimuth), it is clear from Figs. 26 – 28 that the retrieval run is more accurate with the freemode simulation producing too large of an eye and a stretched, smoothed eyewall.

Plots of azimuthal mean tangential wind and relative vertical vorticity averaged over a 1 – 5 km layer and all times (up to 5.25 h) in Fig. 29 further highlight the differences in structure between the retrieval and freemode simulations. The freemode simulations produce a RMW and peak vorticity that is, on average, 10 km too wide. In addition, Fig. 29b shows that the annulus of peak vorticity generated from stretching is too broad compared to observations. Schubert et al. (1999) show for simplified flows (unforced, barotropic and nondivergent) that broad annuli of vorticity have lower growth rates of exponential barotropic instability. As a result, errors in the width of the eyewall at short time intervals can potentially lead to long-lasting errors in the intensity and structure of the simulated storm.

Note, that the structure of the eyewall region in the freemode run is not unique to HIGRAD as many simulations using other mesoscale models also report overly large eye/eyewall regions and RMWs (Yau et al. 2004; Braun et al. 2006; Davis et al. 2008). Although horizontal (and vertical) resolution is a key component of simulated eye/eyewall structure, the differences shown here are not due to resolution, which was reasonably high for the present simulations (2 km in horizontal). Instead, the differences in structure shown in Figs. 26 – 29 are due to the use of the LH retrievals, which force the energy release and subsequent dynamic response to occur in the correct locations while the freemode run is a slave to the water vapor and microphysics scheme for energy release.

Figures 30 and 31 show comparisons of the LH field from the observations (retrievals) and the freemode simulation averaged over a 1 – 5 km layer for two time periods: 1933 UTC 2 August 1997 or 0.58 h into the simulation (Fig. 30) and 2258 UTC 2 August 1997 or 4.08 h into the simulation (Fig. 31). There are large differences in the heating between the observations and freemode simulation with larger magnitudes and more detailed, cellular structure for the observations. The simulated heating has lower magnitudes and the structure is diffuse with smooth, banded features. The wind field snapshots in Figs. 26a and 26b correspond very well with the associated heating fields in Figs. 31a and 31b. The smooth, banded heating in the freemode simulation generated a similar wind field with a large eye and poor eyewall placement. The detailed, cellular nature of the observational heating produced a wind field with excellent explained variance (Fig. 25) and an accurate eyewall placement.

We believe that a major reason for the deficiencies in the simulated structure of the eye/eyewall region in the freemode run is due to the transport of water vapor in the model. Figures 32 and 33 show horizontal snapshots of the water vapor field at 5 km height in the retrieval and freemode simulations at 4.67 h and 5.25 h revealing very similar structure to the LH fields (Figs. 30 and 31) and the wind fields (Figs. 26 – 28). That is, the region of maximum water vapor in the freemode run (eyewall) is stretched wide and overly smooth in azimuth, while the water vapor in the retrieval run is tightly concentrated with larger variance in azimuth. The transport of water vapor in the model is a function of the numerical schemes used for advection and the diffusive tendencies associated with sub-grid scale processes, both of which have inherent uncertainty. A detailed study of the effects of these processes on water vapor transport and eye/eyewall wind structure is needed, but is beyond the scope of the present work.

In addition to water vapor transport, there is also the issue of how well the microphysics scheme can generate the LH derived from the retrievals. Comparing the heating output from the freemode simulation to the LH retrievals (see Figs. 30 and 31) may not isolate the impacts of the microphysical scheme as the updrafts (which are crucial) generated in the freemode simulation are not very consistent with the Doppler analyses. To more accurately isolate the effects of the microphysics, the vertical velocities determined from the Doppler analyses are nudged in the model (similar to the dynamic initialization of the Guillermo vortex) with a coefficient of 10^{-1} s^{-1} for ~ 1 h. In addition to the vertical velocity nudging, the water vapor field derived from the LH retrievals was also used as forcing. Thus, the microphysics scheme (warm rain only) has everything it needs (water vapor and vertical velocities) to generate the retrieved heating over the ~ 1 h forcing period. For this experiment, the model is started from scratch with no vortex, but with the ECMWF profiles of potential temperature, density and water vapor consistent with Guillermo's environment set in the background.

Figure 34 shows the Doppler domain averaged LH rates for $|w| > 5$ m s^{-1} (which are mostly saturated, see section 2.3.1) from the observational forcing experiment and the LH retrievals. The model microphysical scheme under-predicts the retrieved LH rate by a significant amount which is consistent with the integrated wind speeds being too weak for the freemode simulation (see Fig. 23). As discussed above, the microphysical model used here is that of Reisner and Jeffery (2009), which was used to model stratus clouds. In this model, limiters for the condensational heating rate (and others) are employed in order to keep the values well-behaved for numerical accuracy. Preliminary results indicate that these limiters are the reason for the under-prediction shown in Fig. 34. As a result, the work shown here suggests that although the limiters may allow the numerical scheme to achieve higher order accuracy, potentially large errors in heating magnitudes can occur for different cloud systems such as intense convection in TCs. Bulk condensation models similar to Reisner and Jeffery (2009) may have to be tuned for these different cloud systems with a larger limit necessary for the current Guillermo simulations. An important question for future research might be: does a unique bulk condensation model exist for TCs and if not, what is the expected range of variability?

The discussion and figures from the present section show that the LH retrievals produce a more accurate simulation of rapidly intensifying Hurricane Guillermo in terms of RMSEs, explained variance and eye/eyewall structure than using the model microphysics scheme in a freemode run. The differences are likely due to errors/uncertainties in the model associated with: (1) the transport of water vapor which is a function of diffusion and numerical approximations to advection and (2) the microphysics scheme, specifically the limits on heat release. Detailed conclusions from the entirety of chapter two are discussed in chapter four.

Table 1. Summary of Hurricane Guillermo (1997) numerical experiments examining various heat forcings. All simulations start from the same initial vortex (Figs. 17 and 18), which is introduced into the model through a 9 – 10 h dynamic initialization procedure described in the text. After the initialization, the model is run for ~ 6 h for each experiment. See the text for the details of each experiment.

Experiment Name	**Description**
Retrieval	3D latent heat retrievals used as forcing with an initial ten minute ramping period described in (13); linear interpolation between each snapshot used thereafter. No model microphysical heating is allowed.
Saturated	Same as the retrieval run, only all heating/cooling released in the latent heat retrieval (assumes all grid points are saturated).
Freemode	No latent heat retrievals used directly. Instead, model microphysical heating is enabled. In addition, the first latent heat retrieval snapshot is converted to water vapor and forced into the model over a ten minute ramping period similar to the retrieval run.
Unforced	No heating or moisture forcing of any kind is used.

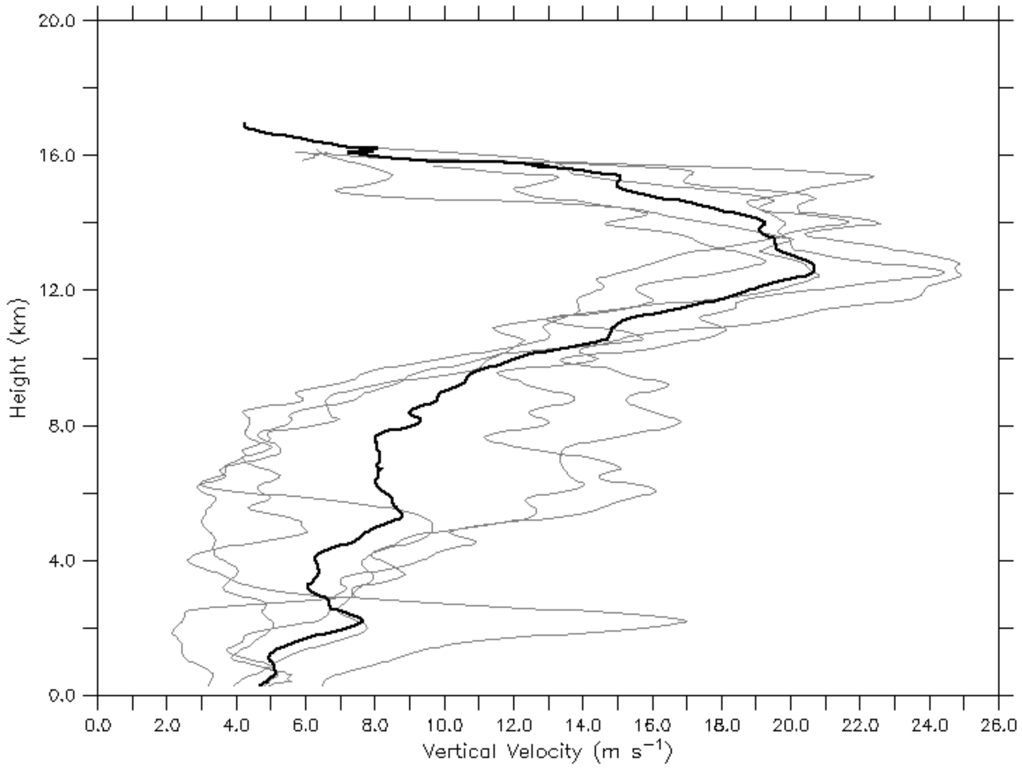

Figure 1. The top five maximum updraft profiles in TC hot towers from the Heymsfield et al. (2010) population. The gray lines show each member with the black line representing the mean. See Heymsfield et al. (2010) for more information.

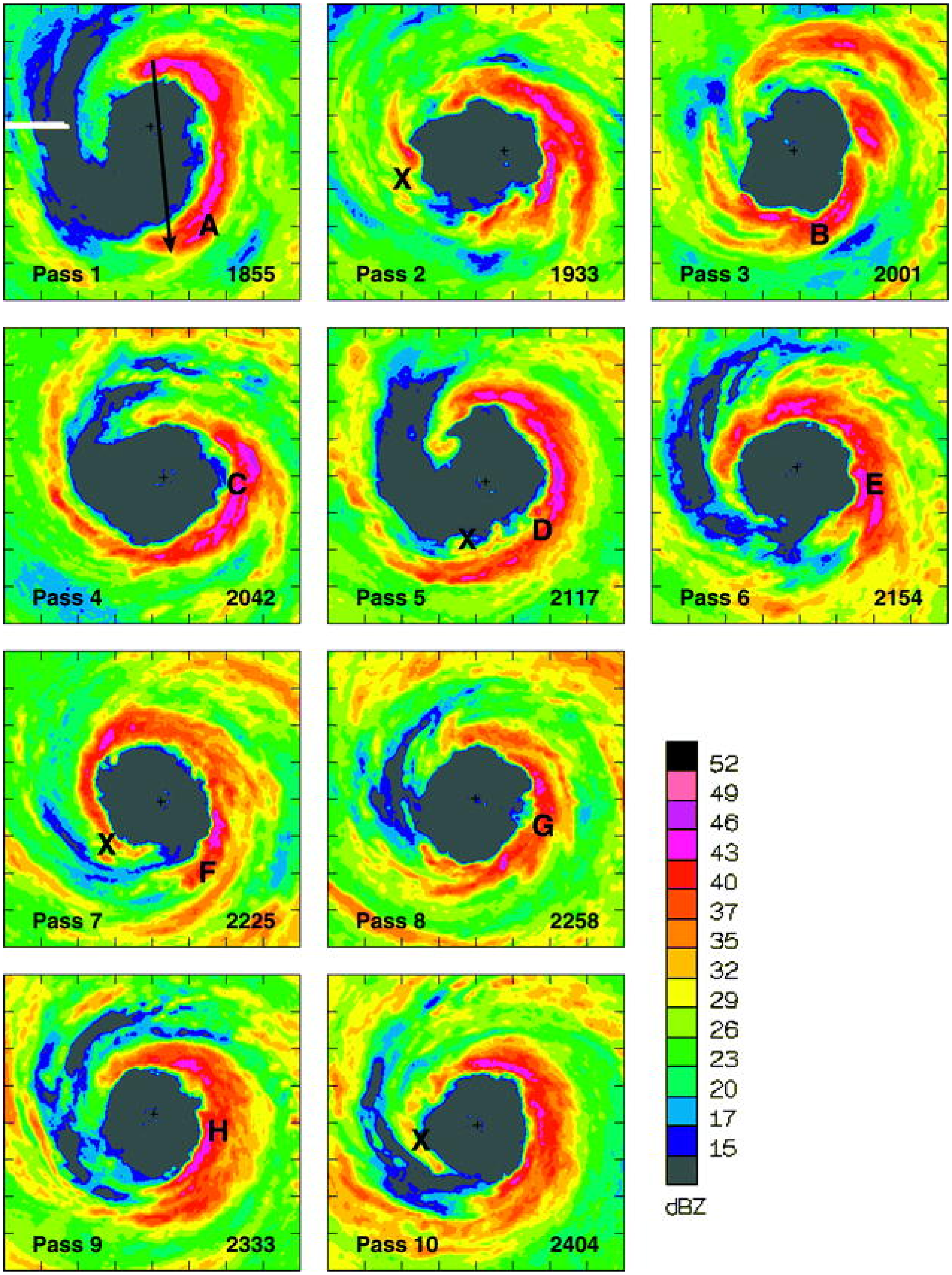

Figure 2. NOAA P-3 lower fuselage radar (5.3 GHz) reflectivity at 3-km height during the center of each aircraft pass through Hurricane Guillermo (1997). The domain is 120 km on each side with tick marks every 15 km. The solid arrow in pass 1 represents the time-averaged, local shear vector and the capital letters denote details of the convective bursts. Figure is taken from Reasor et al. (2009). Used with permission of the AMS.

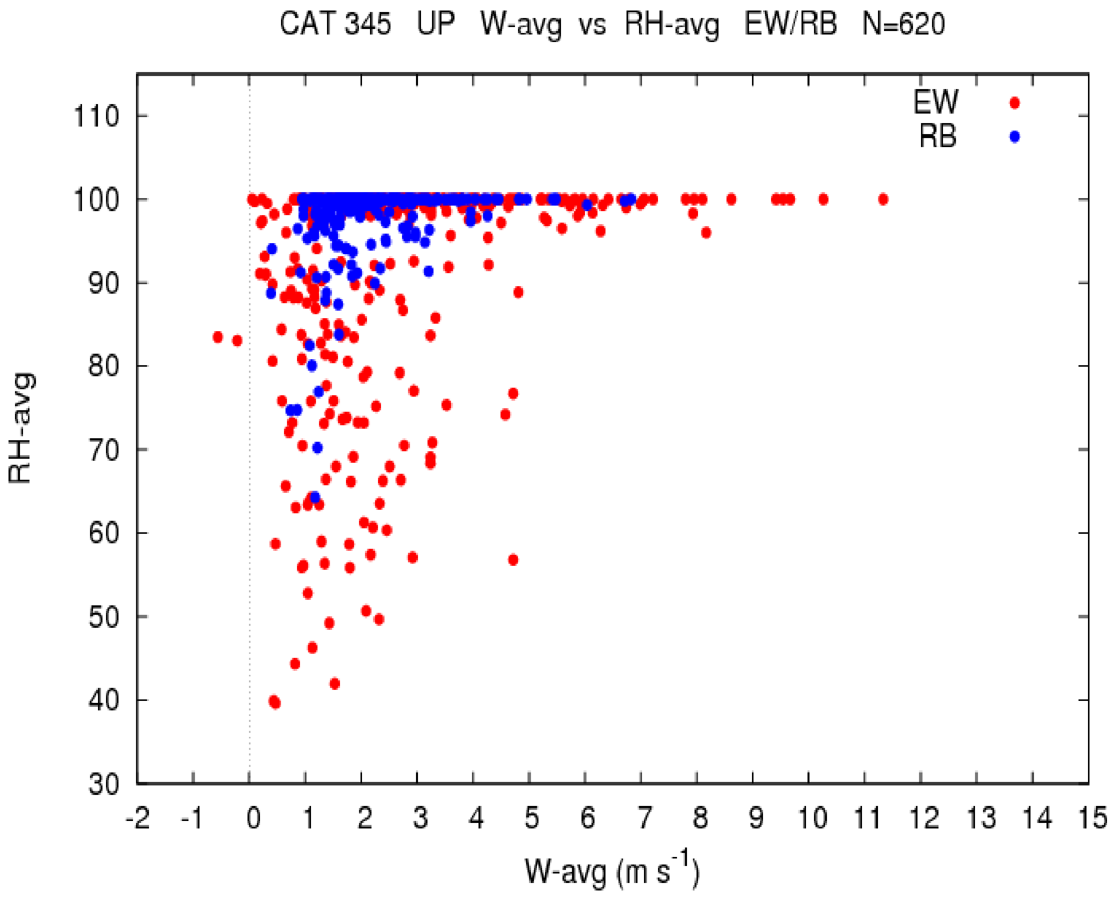

Figure 3. Aircraft (P-3) flight level (between 1.5 to 5.5 km altitude) measurements of updraft core magnitude as a function of relative humidity from the eyewall and rainband regions of intense TCs. Note that there are 620 data points in the figure. The figure is courtesy of Matt Eastin; see Eastin et al. (2005) for details.

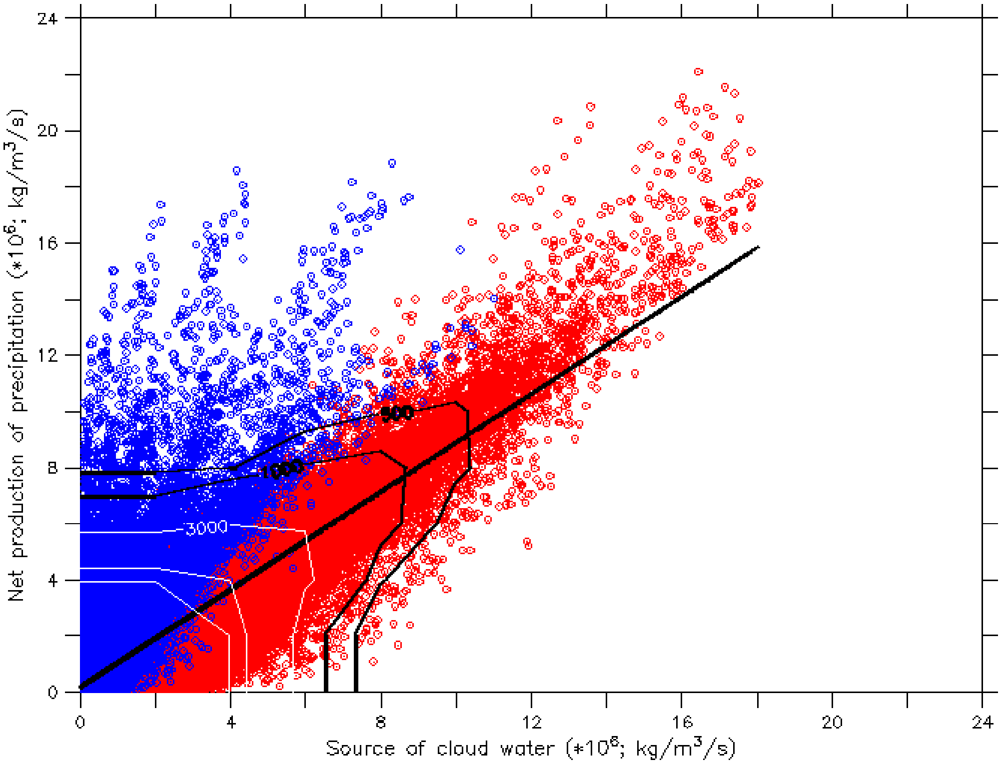

Figure 4. Relationship between the source of cloud water and the net production of precipitation for grid points that are producing precipitation in the model domain between 0 and 10 km height and over a nine minute period (with three minute output). Data is from the numerical simulation of Hurricane Bonnie (1998; Braun 2006). The black line shows the linear fit to the data with an R^2 of ~0.70 found using all 60 minutes of model output. The red and blue circles denote warm ($T > 0°C$) and mixed/ice ($T \leq 0°C$) phase precipitation processes, respectively. An R^2 of ~0.87 was found applying the linear fit to the red points only over a 60 minute period. The contour lines show the number of points in dense regions of the scatter plot. Black contours start at 500 with a 500 point interval while white contours start at 3000 with a 6000 point interval. There are a total of 828,611 points in the figure with the largest percentage located in the lower left corner (> 15,000 points).

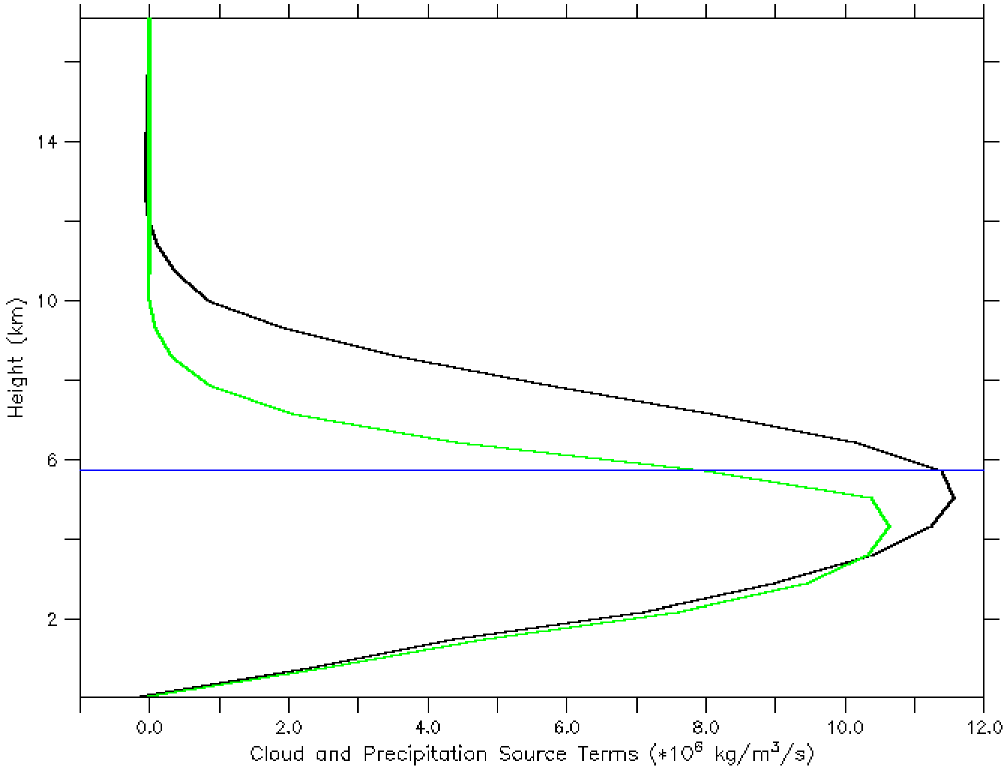

Figure 5. A typical profile of the net source of precipitation (black line) and the source of cloud water (green line) through deep eyewall convection in the numerical simulation of Hurricane Bonnie (1998; Braun 2006). The profiles were averaged over a 10 km by 10 km horizontal region centered on a convective cell for one snapshot in time. The blue line highlights the freezing level.

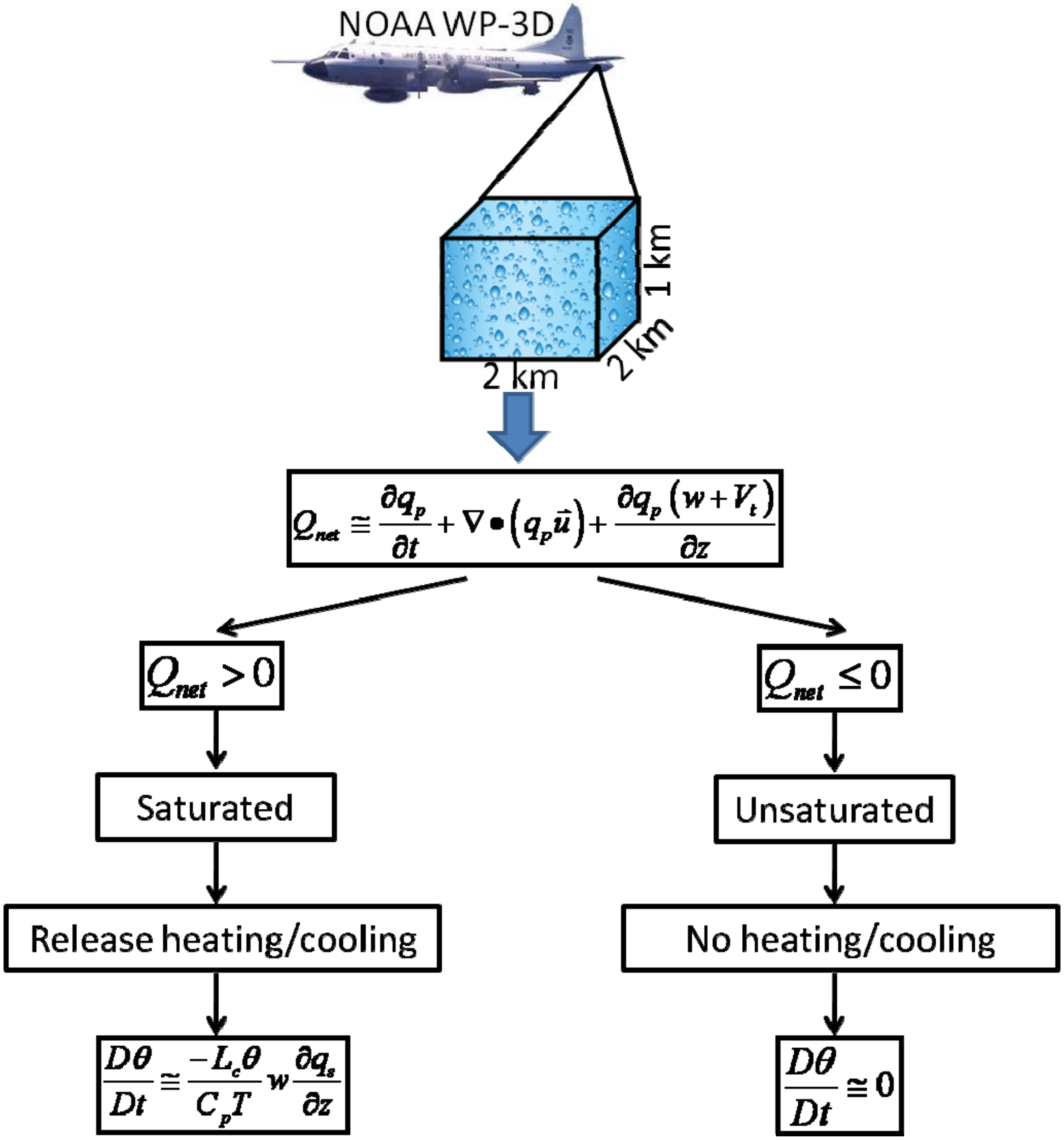

Figure 6. Flowchart summarizing the basic steps in the LH retrieval algorithm. These steps are performed at each grid point in the Doppler analysis domain. All variables and equations, including approximations are defined in the text.

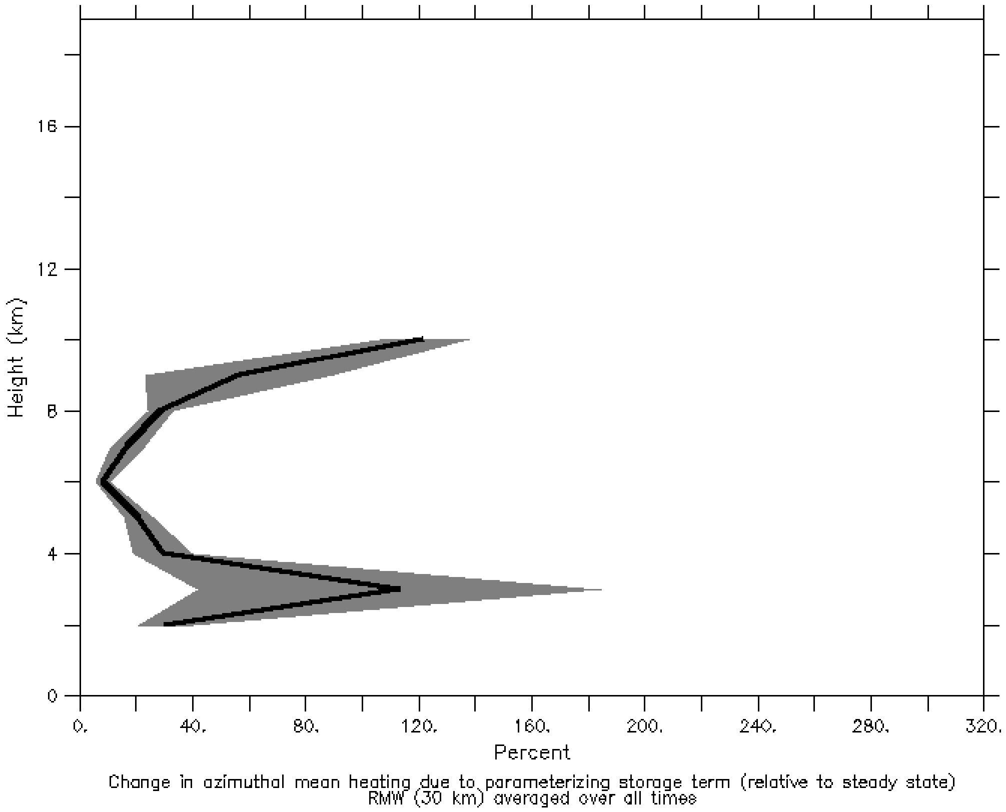

Figure 7. The impact of the model-derived storage term parameterization on the azimuthal mean heating at the RMW for the Guillermo Doppler analyses. The thick black line shows the time mean and the shading depicts the standard deviation of the mean.

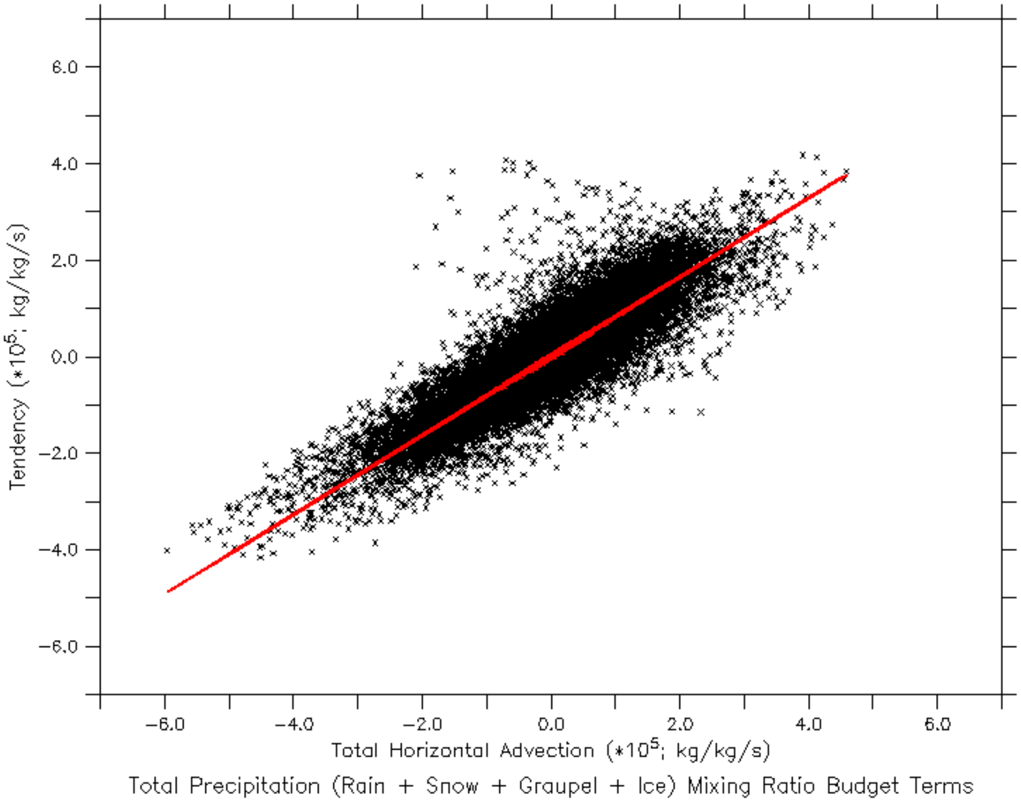

Figure 8. The relationship between the horizontal advective flux of precipitation (in brackets on right-hand-side of equation 5) and the storage of precipitation for all grid points that are producing precipitation at one snapshot in time. Model data is from Hurricane Bonnie (1998; Braun 2006) using 2 km horizontal resolution. The fit (see text) explains 78% of the variance in the data.

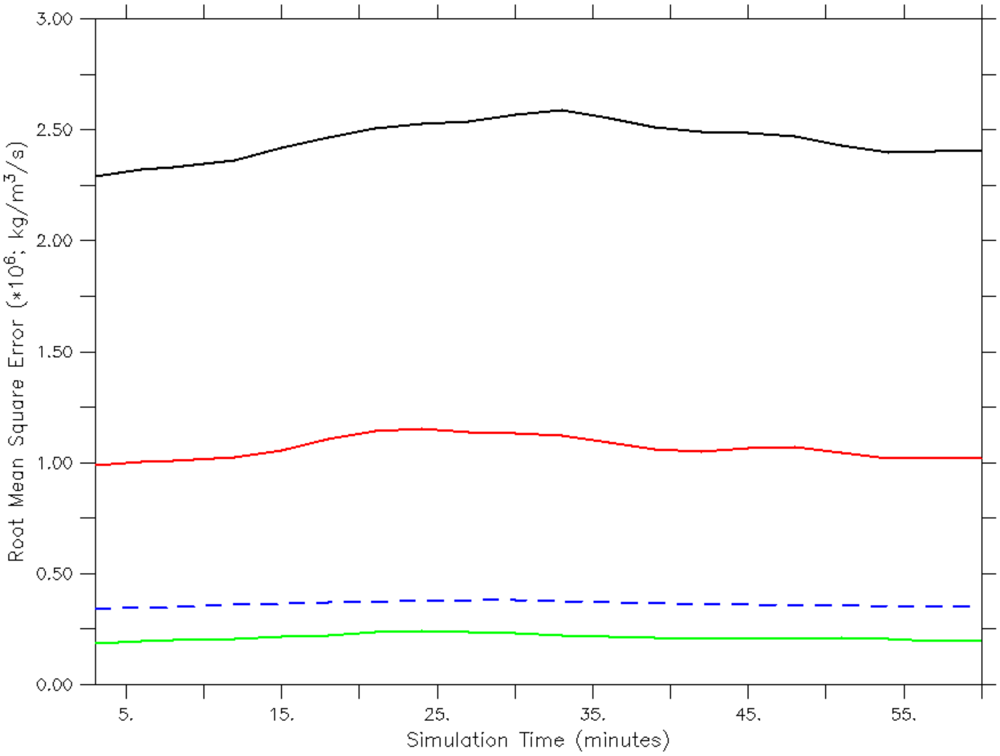

Figure 9. The impact of the model-derived storage term parameterization in terms of the RMSE for Q_{net} averaged over the model domain. Computing Q_{net} using the steady state assumption (black line), the parameterization (red line) and the reduced form of the precipitation continuity equation (2) shown in the green line. The control is the full model equation presented in (1). The blue dashed line shows the mean value of Q_{net} for reference.

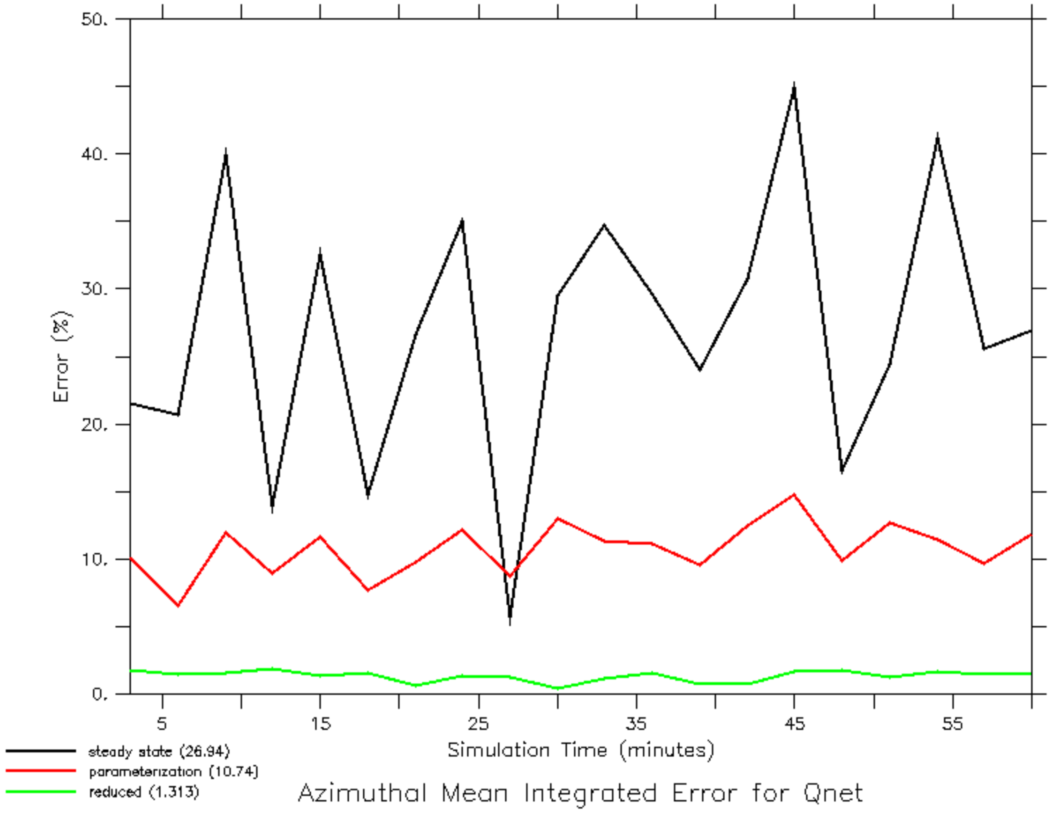

Figure 10. Same as Fig. 9 only the chosen measure of error here is the azimuthal mean integration for Q_{net}. The mean values over time for each case are: steady state (~27%), parameterization (~11%) and reduced form (~1%).

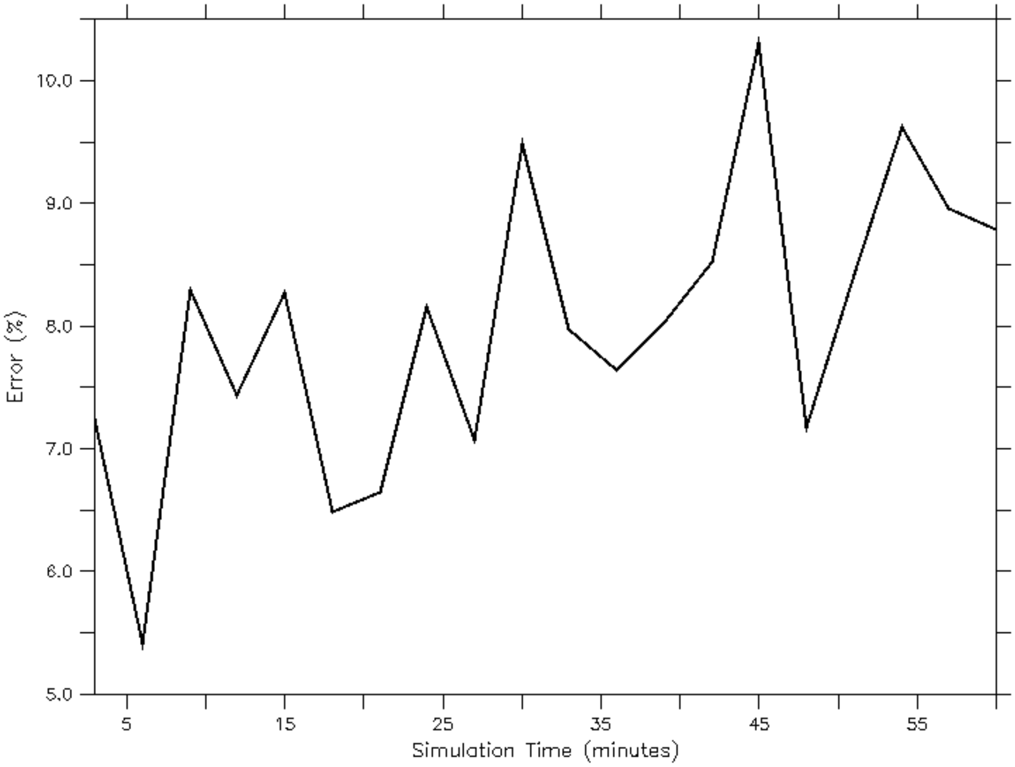

Figure 11. The error (according to equation 6) in releasing heat by using Q_{net} as a proxy for saturation and equations (2) and (5) to determine where the values of Q_{net} are greater than zero. The control is releasing heat where grid points are producing cloud water. Heating rates are computed according to equation (4) with the figure showing results for updrafts only. See text for algorithm details. The temporal mean error is ~8%.

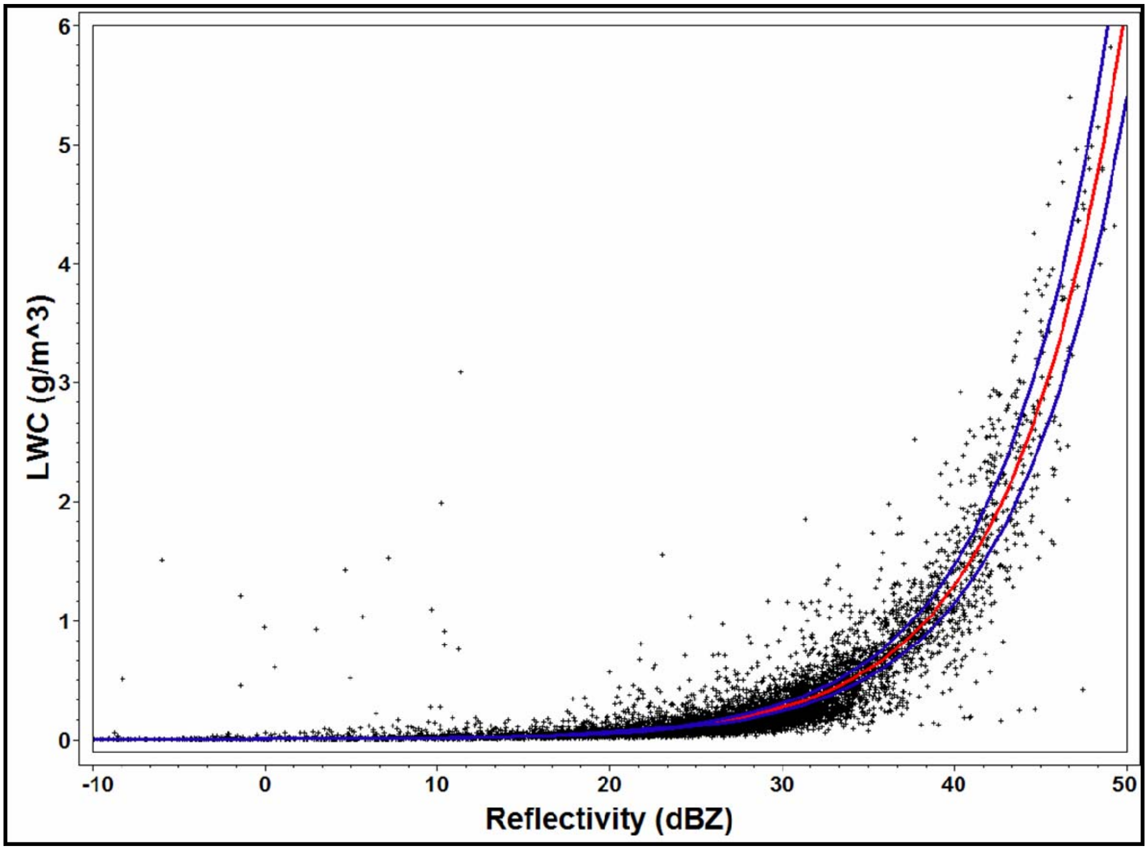

Figure 12. The relationship between radar reflectivity factor (expressed in dBZ) and liquid water content using cloud particle data (~ 7,000 data points) from NOAA P-3 aircraft flying at ~ 4 km altitude in Hurricane Katrina (2005) during a mature stage of the storm. The red line shows the best-fit nonlinear model ($Z = 402 \times LWC^{1.47}$) and the blue lines represent the 95% confidence interval. The correlation coefficient is 0.88.

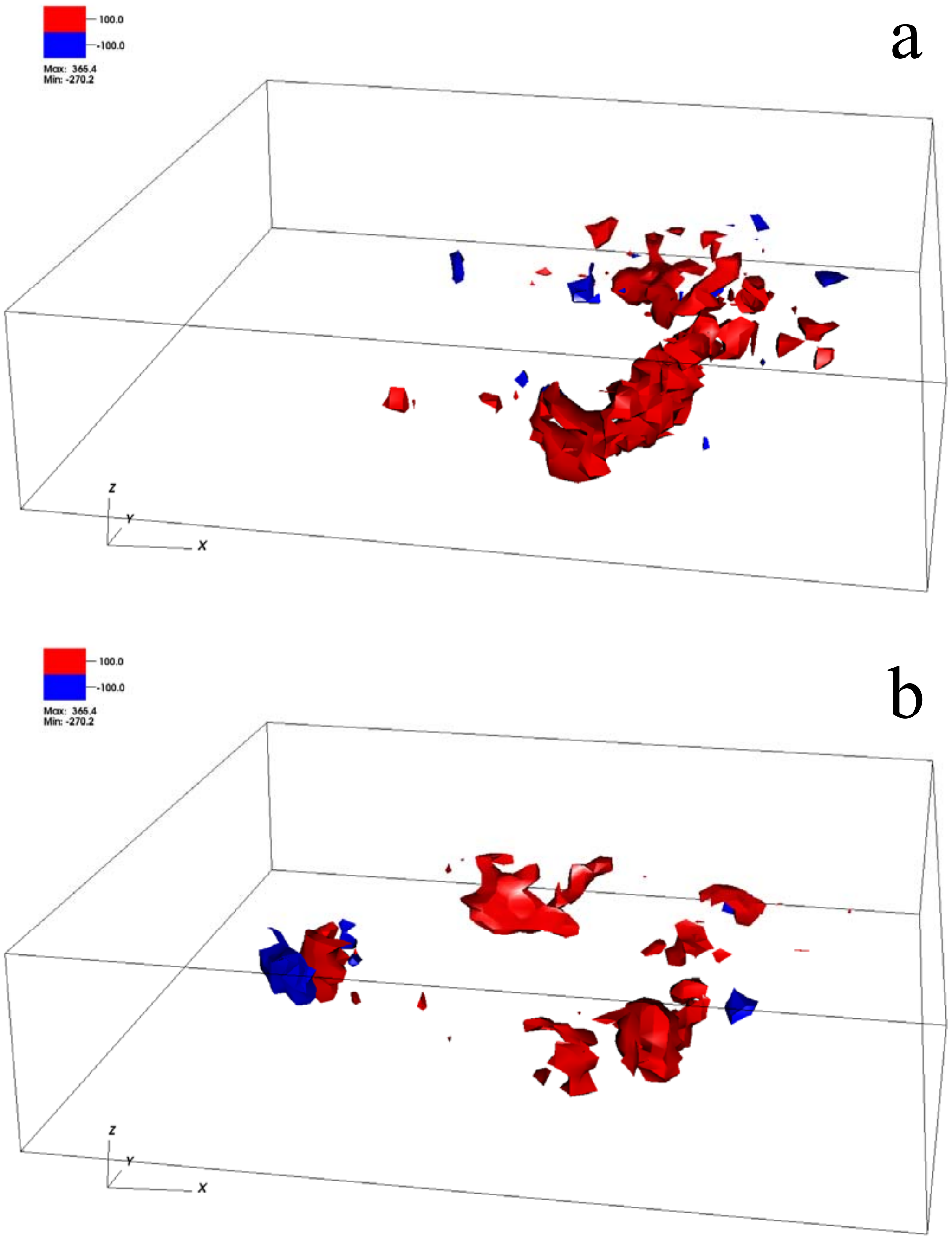

Figure 13. Three-dimensional isosurfaces of the latent heat of condensation (K h^{-1}) retrieved from Doppler radar observations in Guillermo at (a) 1855 UTC 2 August and (b) 2225 UTC 2 August. The grid volume is storm-centered extending 120 km on each side and 19 km in the vertical with a grid spacing of 2 km in the horizontal and 1 km in the vertical. The first useful level is at 1 km due to ocean surface contamination. Red indicates condensation while blue shows evaporation.

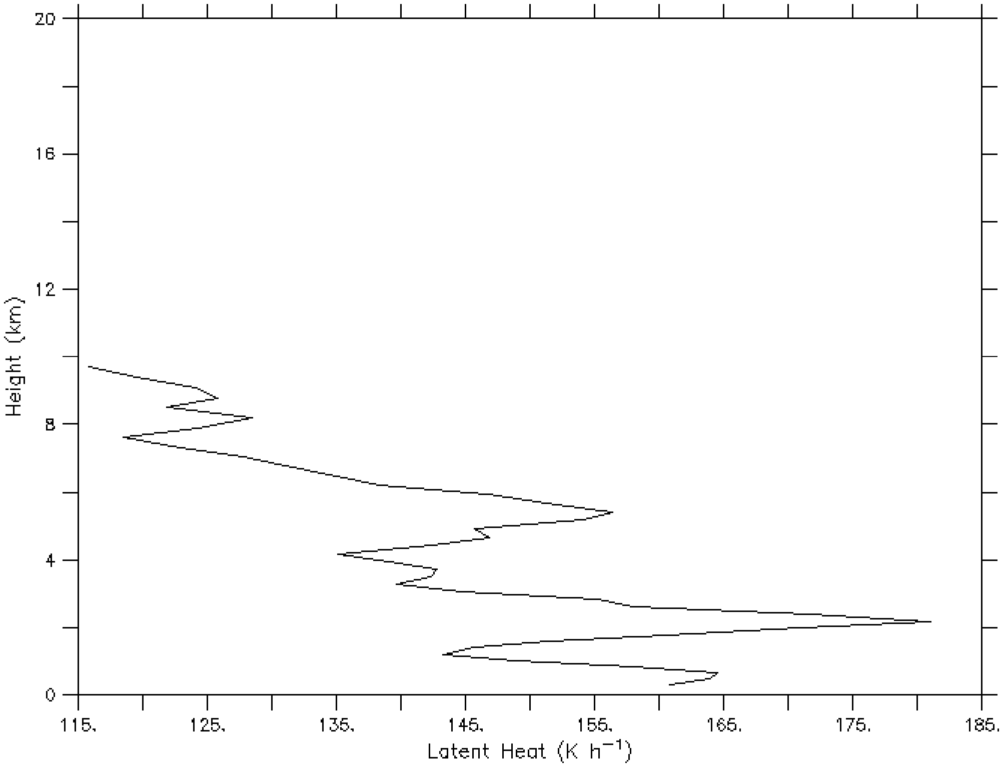

Figure 14. Profile of the LH of condensation (K h^{-1}) for the mean EDOP hot tower profile shown in Fig. 1. See text for details.

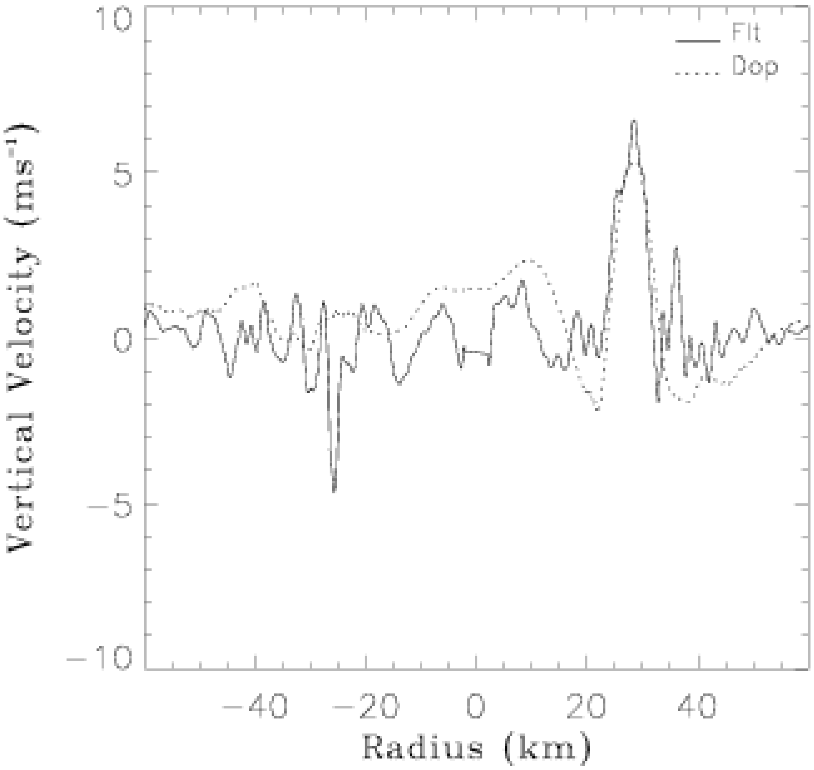

Figure 15. Comparison of P-3 flight level (~3 km altitude) and Doppler radar retrieved vertical velocity for a radial penetration into Hurricane Guillermo valid at ~2002 UTC 2 August 1997. Figure is from Morrow (2008). See Reasor et al. (2009) for details of the comparisons.

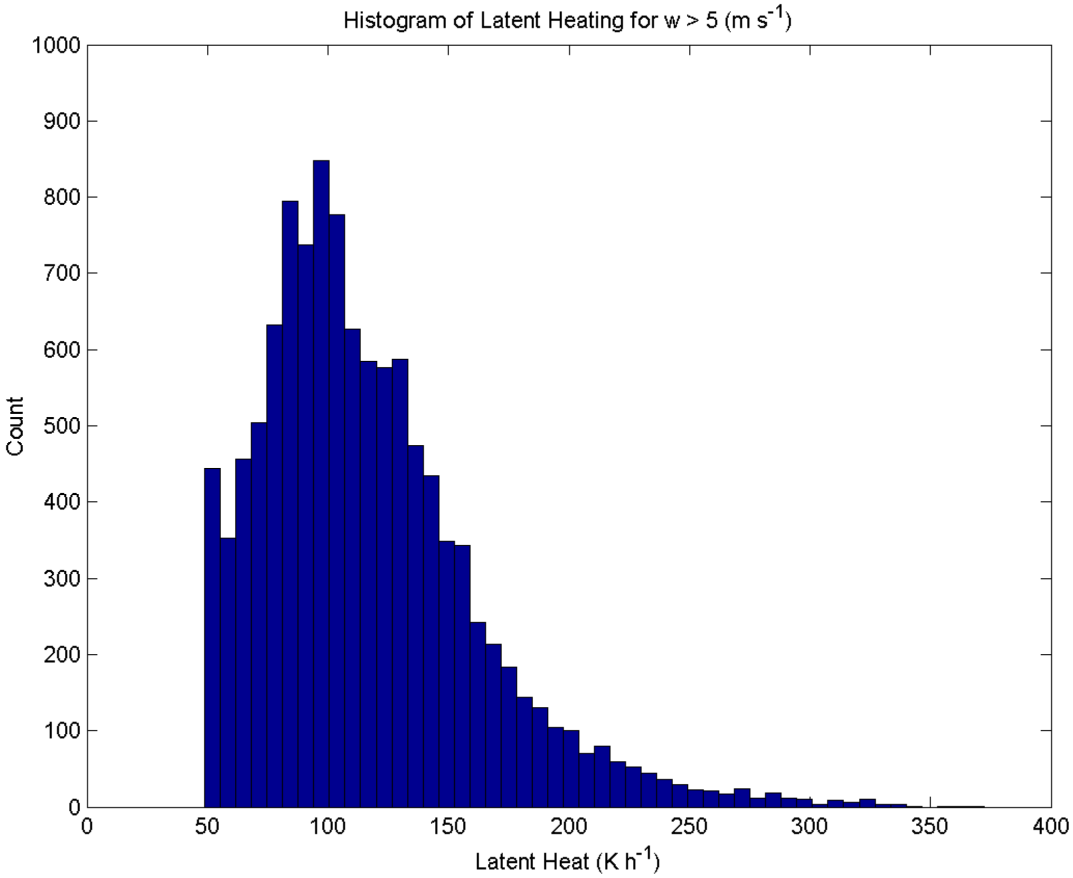

Figure 16. Histogram of Doppler radar retrieved latent heating rates for vertical velocities > 5 m s^{-1} in Hurricane Guillermo on 2 August 1997.

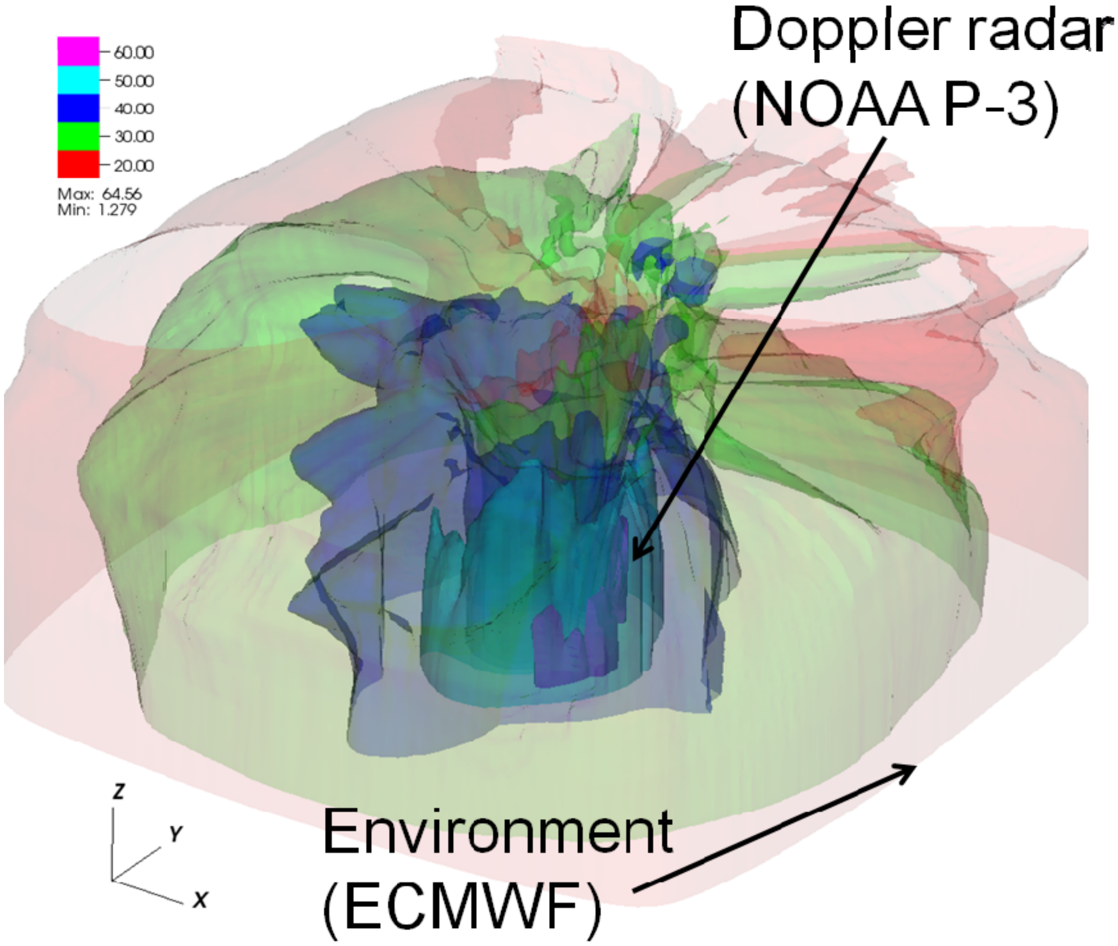

Figure 17. A 3D depiction of the merged vortex used to initialize Hurricane Guillermo into HIGRAD. Shown are isosurfaces of wind speed (m s^{-1}) with opacity scaling that allows a view of the inner core of the storm (from Doppler radar analyses) as well as the blending into the environment (from ECMWF analyses). The grid volume is storm-centered and shows an inner portion (roughly 500 km on each side) of the full model domain and up to 22 km in the vertical. See text for more details on the model grid.

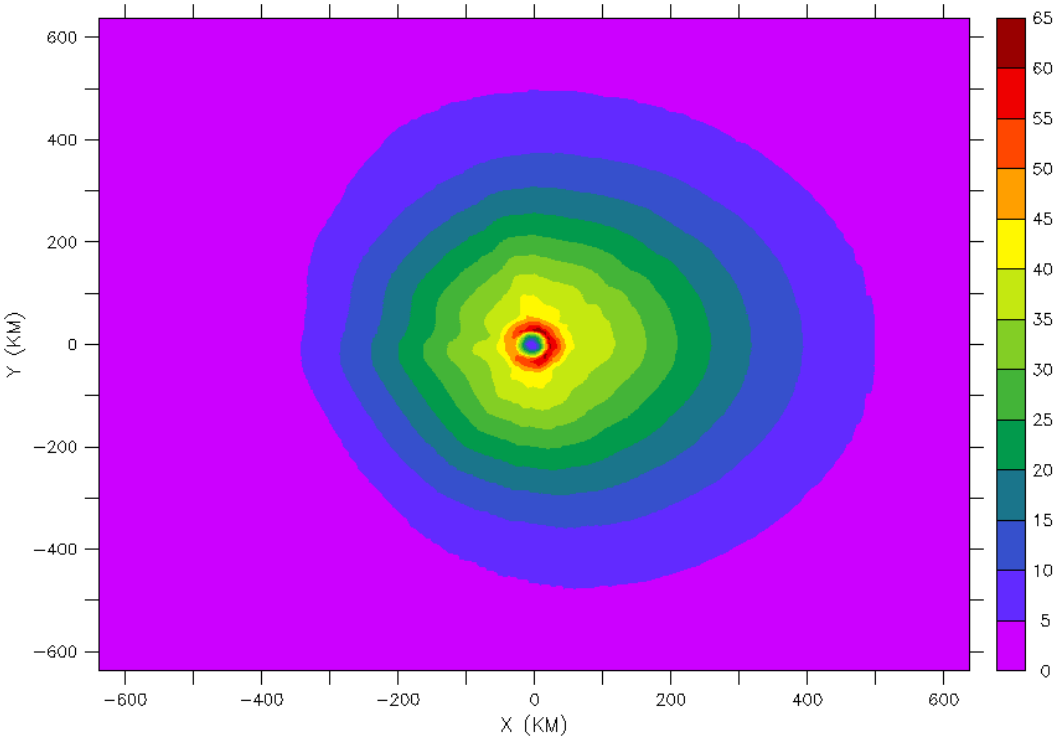

Figure 18. A horizontal cross section of the merged vortex used to initialize Hurricane Guillermo (1997) in HIGRAD showing wind speed at ~ 1 km altitude on the full model domain.

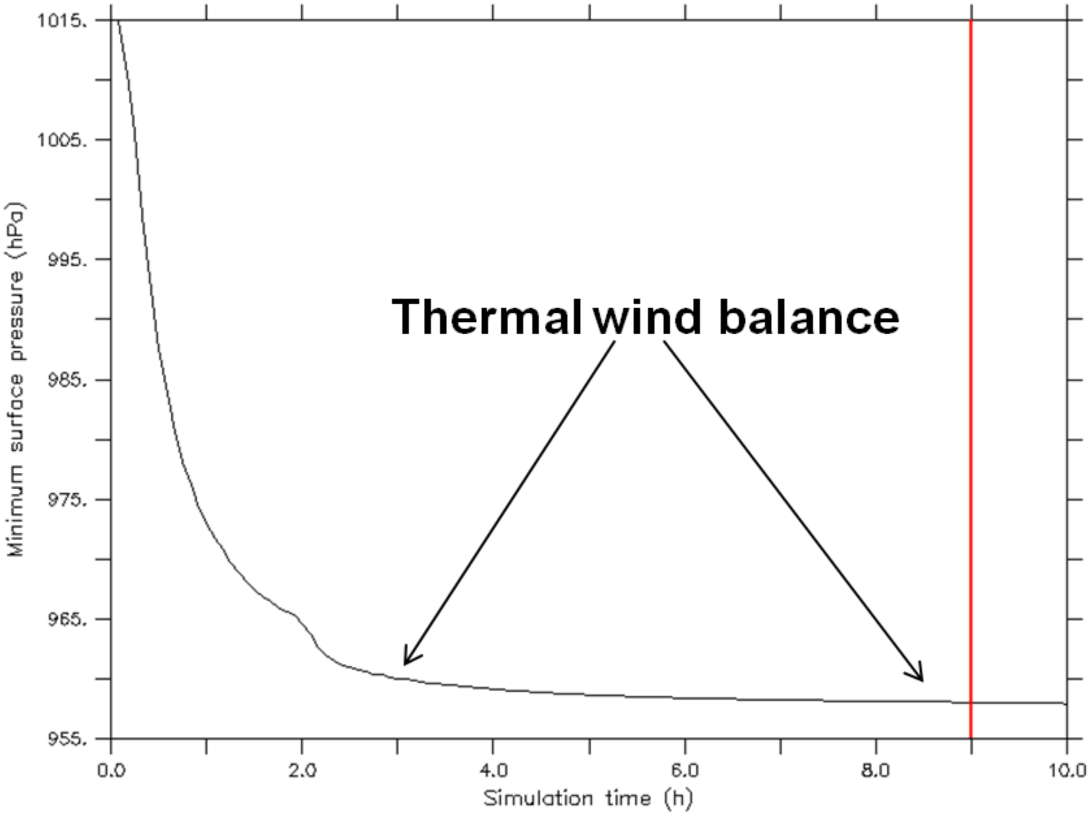

Figure 19. Time series of the minimum pressure in HIGRAD for the dynamic initialization of the merged Guillermo vortex. The red line marks when the initialization was stopped and the nudging coefficient set to zero.

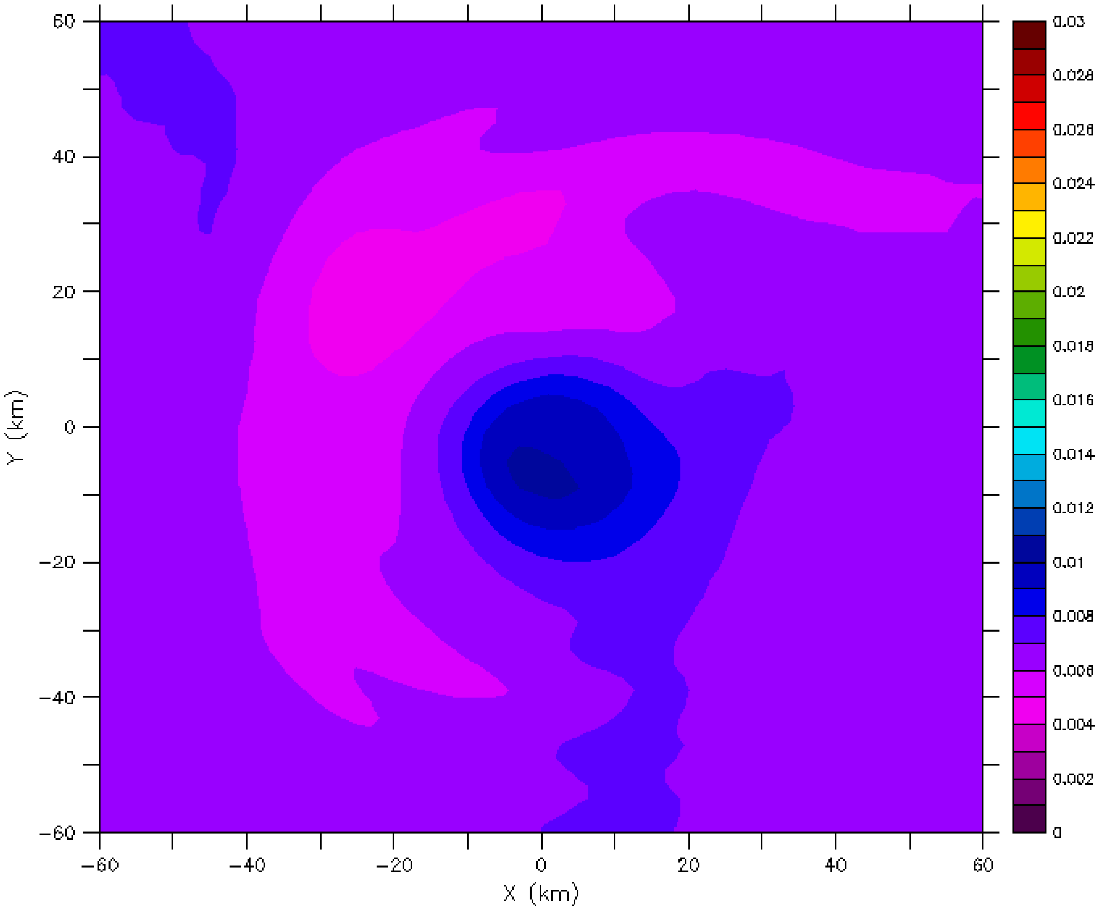

Figure 20. Horizontal cross section of water vapor mixing ratio (kg kg^{-1}) at 5 km height after 9 h of vortex nudging. Only the inner part of the model domain that corresponds to the Doppler analysis is shown.

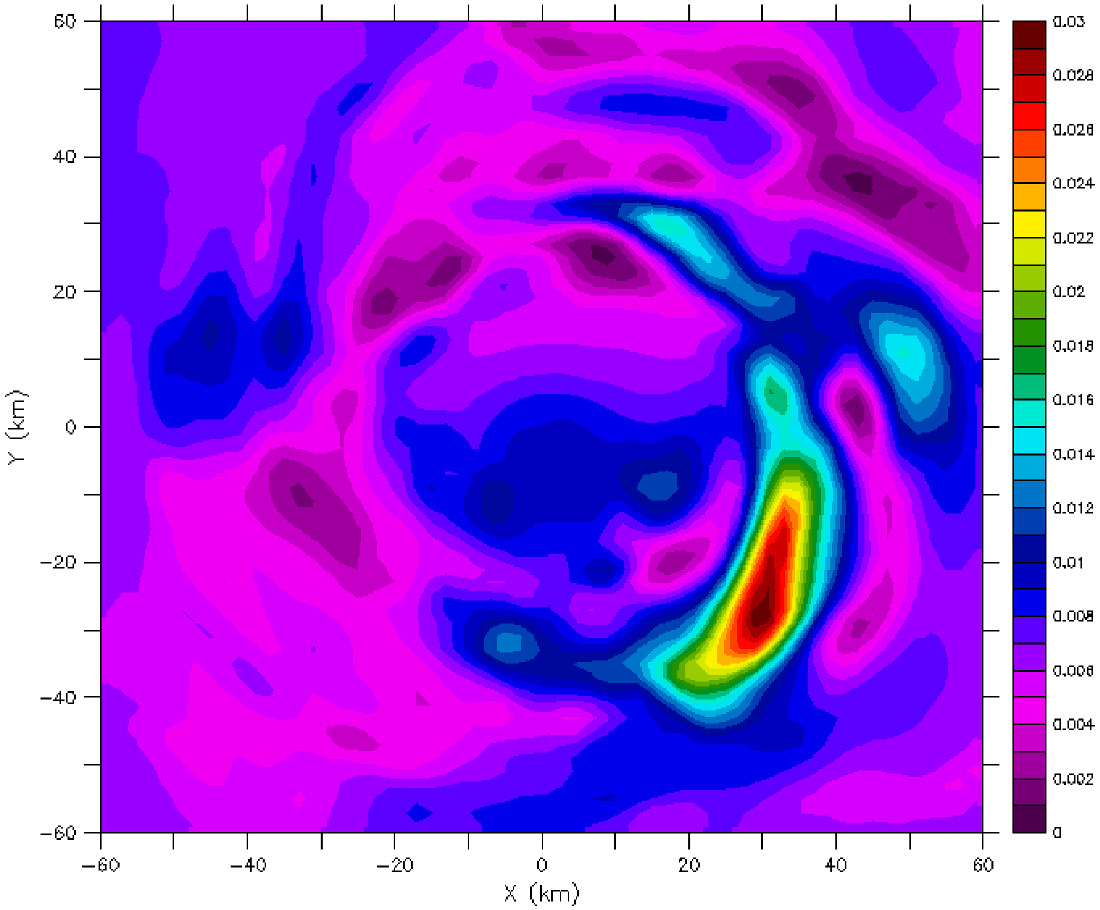

Figure 21. Horizontal cross section of water vapor mixing ratio (kg kg^{-1}) at 5 km height after the dynamic initialization and ten minutes of moisture forcing. Only the inner part of the model domain that corresponds to the Doppler analysis is shown.

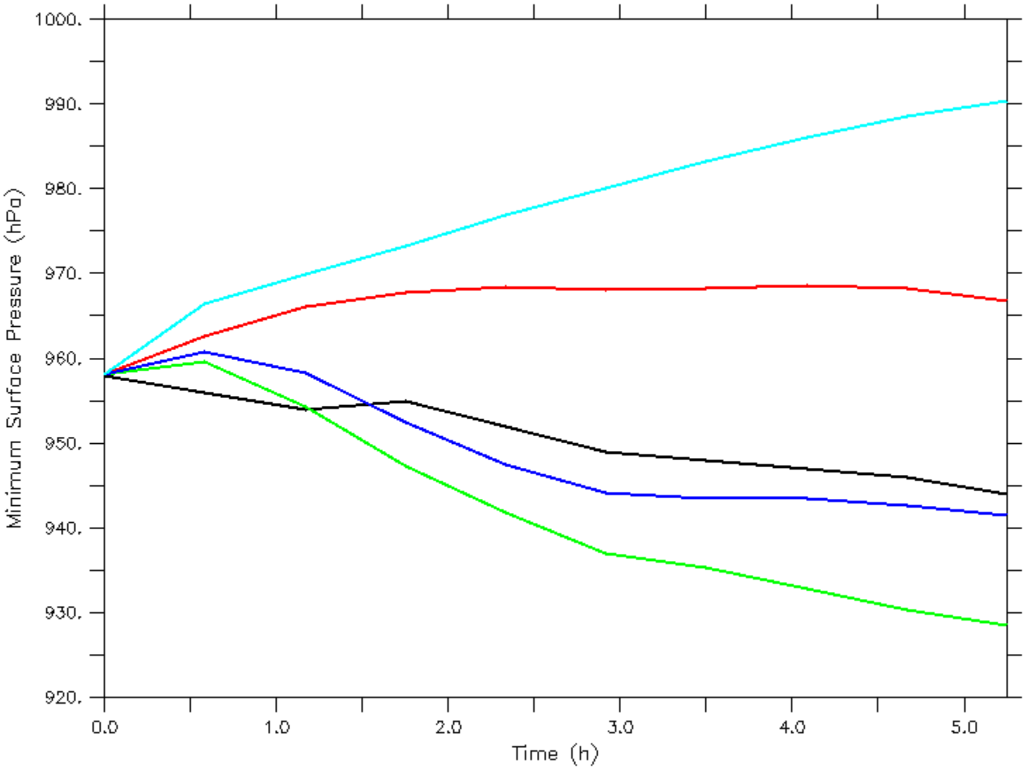

Figure 22. Time series of minimum surface pressure (hPa) for the Guillermo numerical simulations discussed in the text. Values are plotted for all ten aircraft composite times listed in Fig. 2 with 0 h representing the spun-up, merged vortex of Guillermo. The turquoise line is the unforced run, red is the freemode run, blue is the retrieval run and green is the saturated run. The black line shows the observations (Zou et al. 2010).

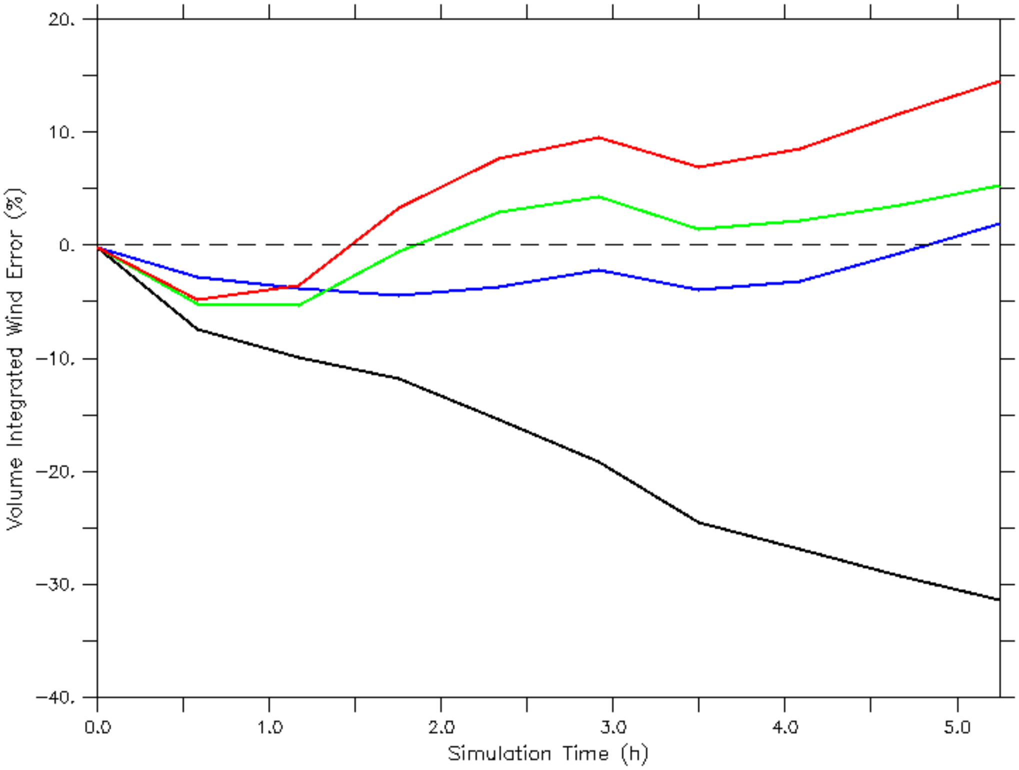

Figure 23. Time series of simulated wind speed errors relative to Doppler radar analyses computed according to (6), only integrated over the Cartesian Doppler analysis volume rather than an azimuthally averaged, cylindrical volume. Errors are shown for all ten aircraft composite times listed in Fig. 2 with the 0 h simulation time representing the spun-up, merged vortex of Guillermo. The black line is the unforced run, blue line the freemode run, green line the retrievals run and the red line is the saturated run.

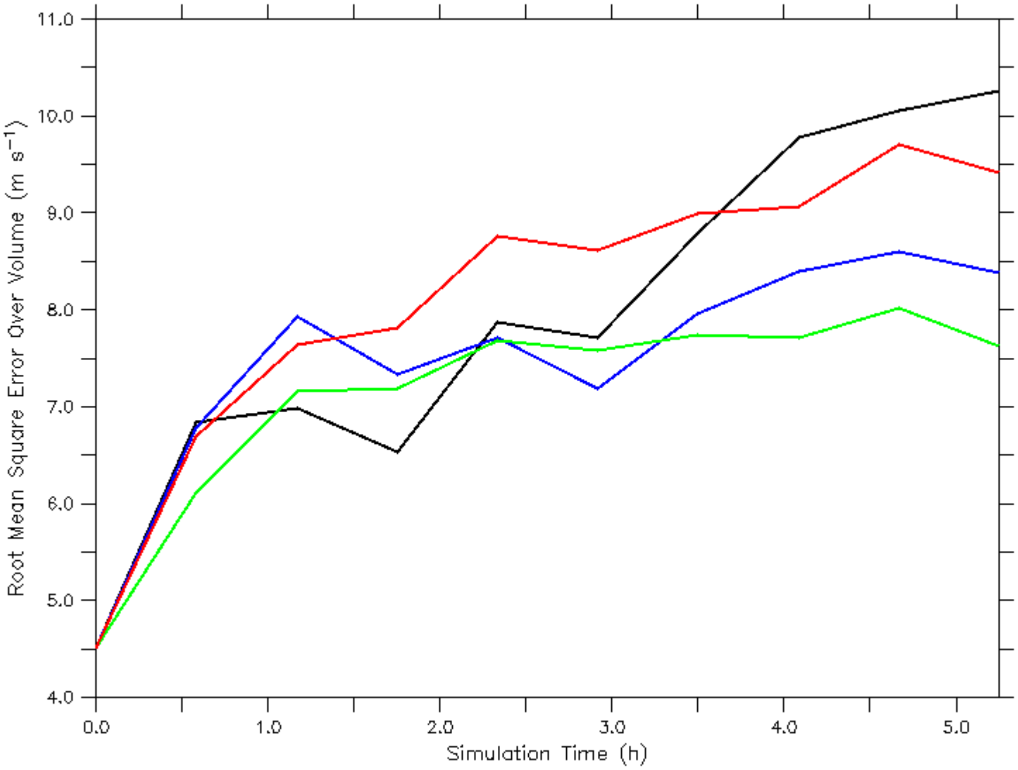

Figure 24. Similar to Fig. 23, only showing RMSEs for the simulated wind speed relative to the Doppler radar analyses. The RMSEs are computed for each horizontal wind component first, then the wind speed is calculated.

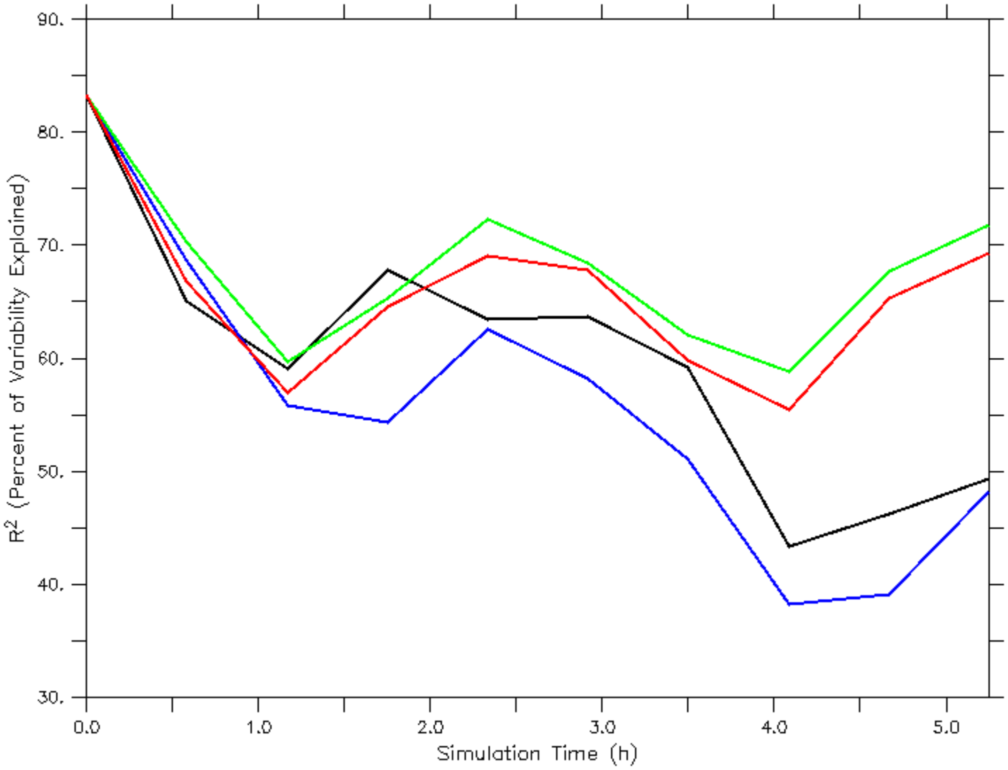

Figure 25. Similar to Fig. 23, only showing the square of the correlation coefficient (a measure of how well the simulations capture the variability in the observations) for the simulated wind speed relative to the Doppler radar analyses.

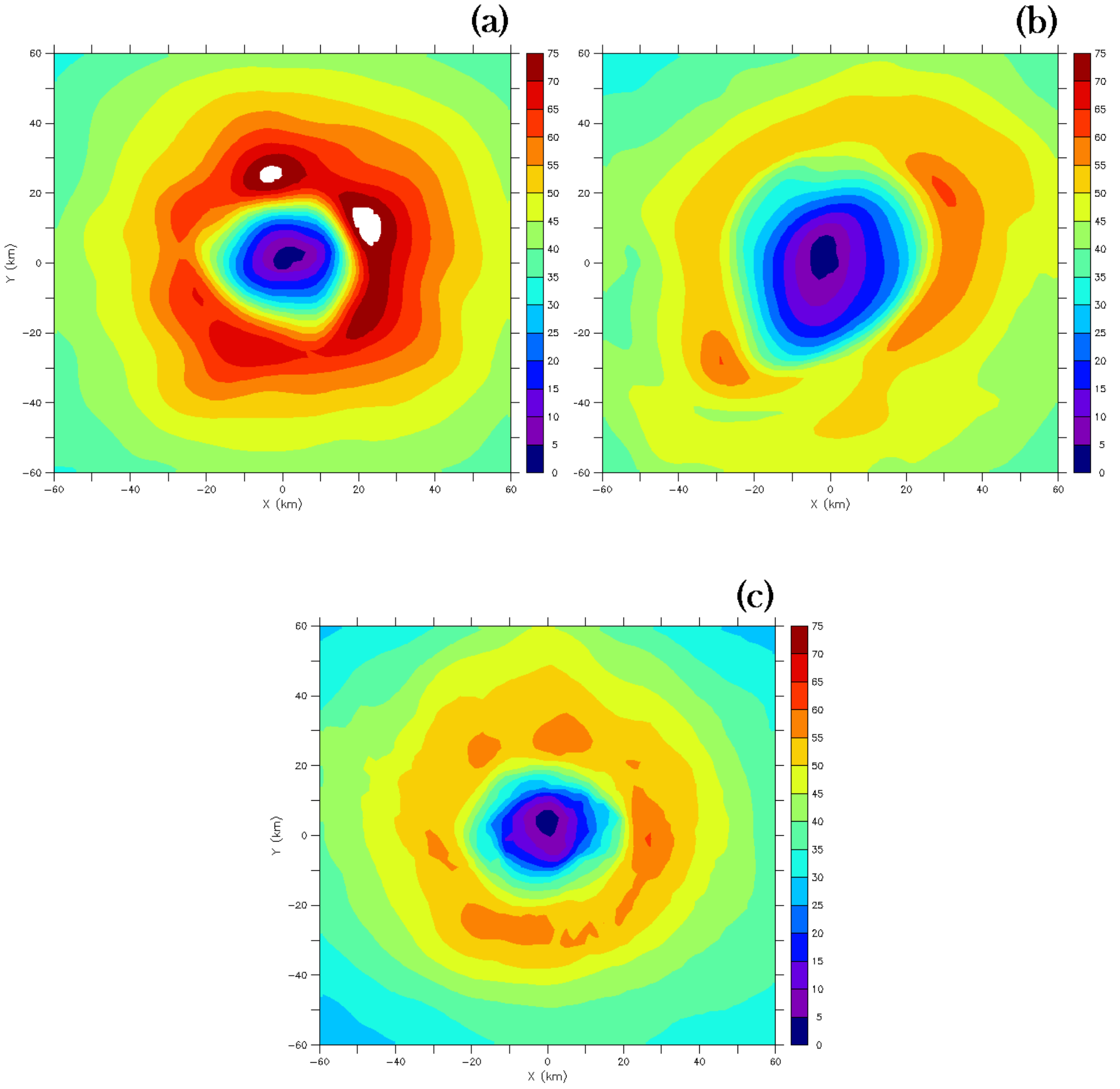

Figure 26. Horizontal cross sections of wind speed (m s^{-1}) at 1 km height after (a) 4.08 h of simulation for the retrieval run, (b) 4.08 h of simulation for the freemode run and (c) the Doppler analysis at 2258 UTC 2 August 1997 at which time (a) and (b) are valid. Only the inner part of the model domain that corresponds to the Doppler analysis is shown in (a) and (b).

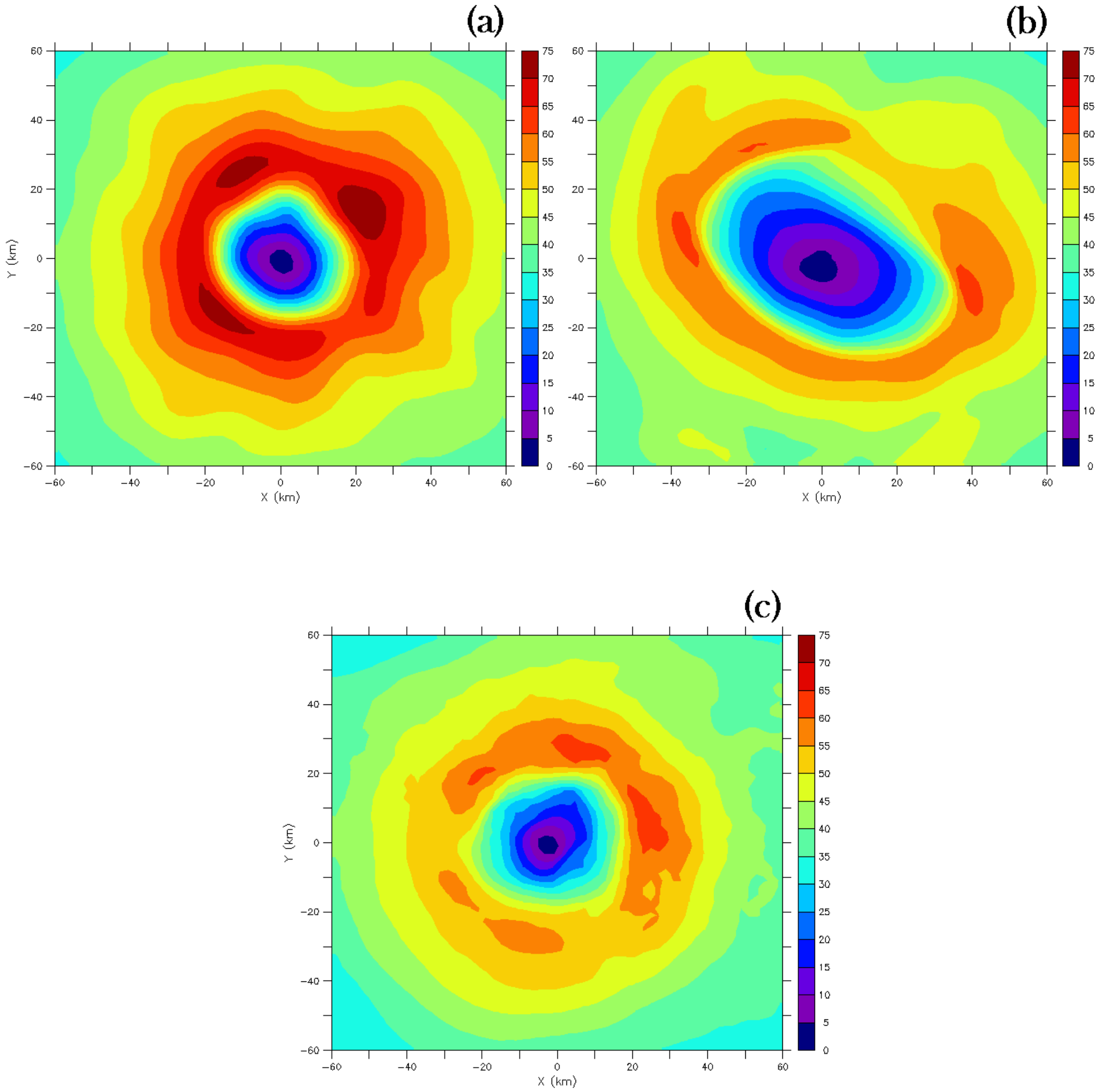

Figure 27. Same as in Fig. 26 only at 4.67 h into the simulations for (a) and (b) with the the Doppler analysis in (c) at 2333 UTC 2 August 1997.

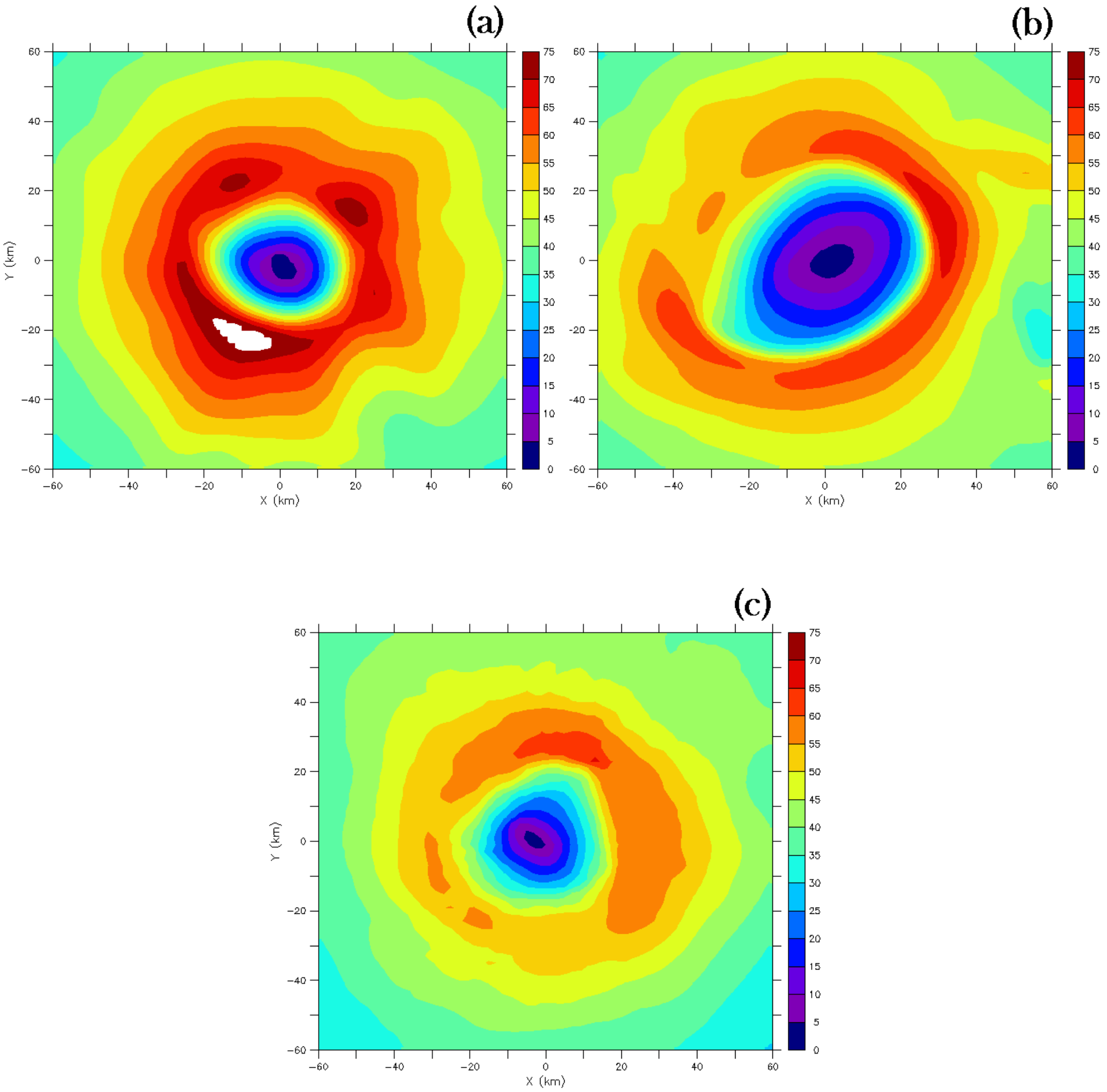

Figure 28. Same as in Fig. 26 only at 5.25 h into the simulations for (a) and (b) with the the Doppler analysis in (c) at 2404 UTC 3 August 1997.

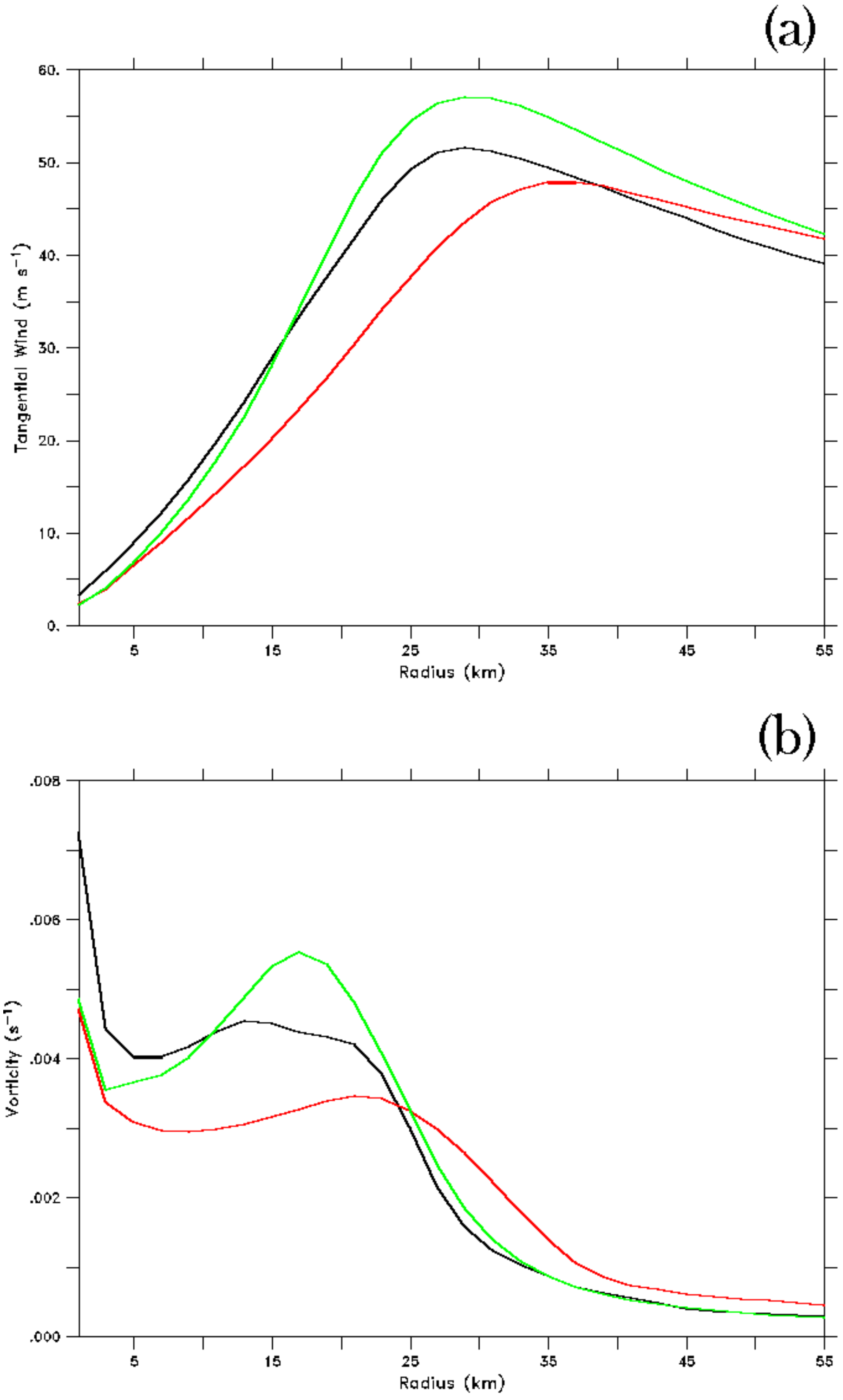

Figure 29. Azimuthally averaged plots of (a) tangential wind (m s^{-1}) and (b) relative vertical vorticity (s^{-1}) for the retrieval run (green line), freemode run (red line) and Doppler observations (black line). The fields are averaged over height (1 – 5 km) and time (up to 5.25 h).

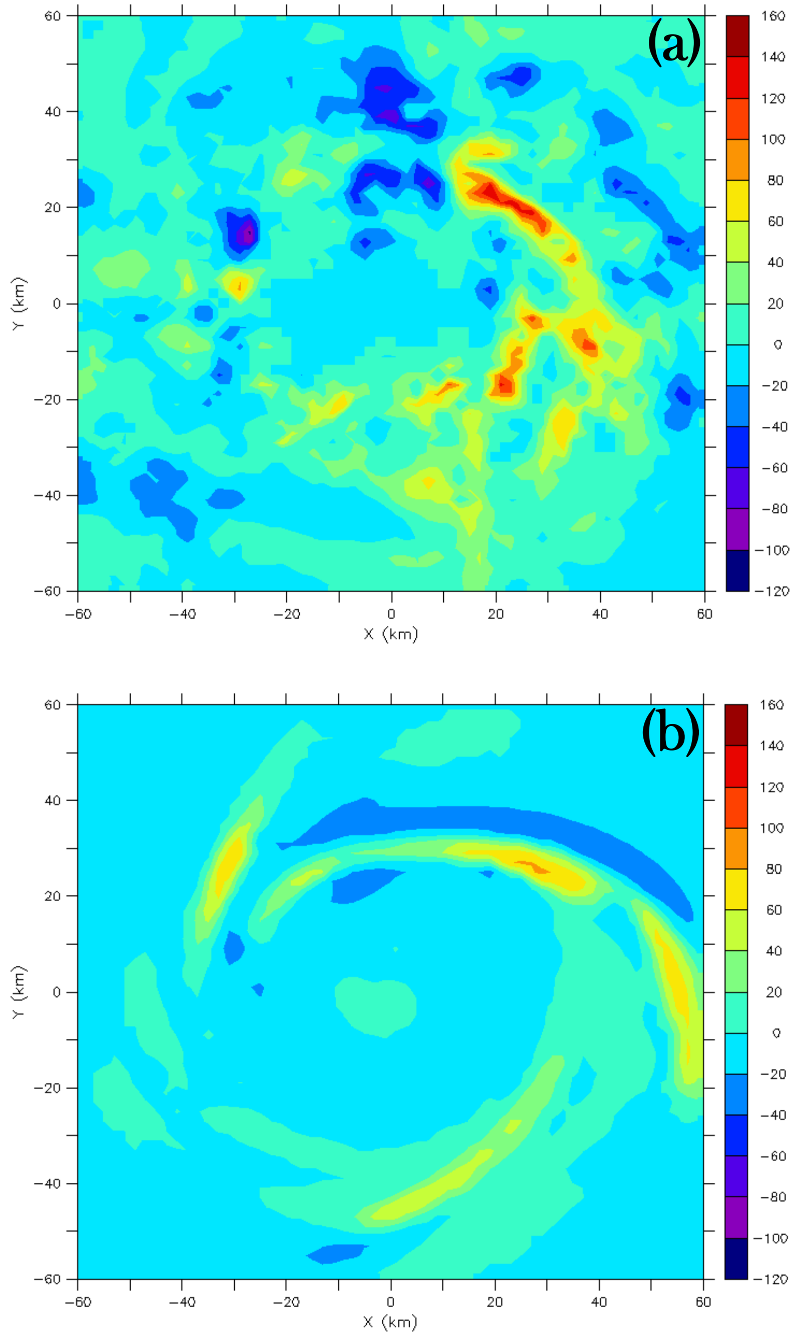

Figure 30. Horizontal cross-sections of latent heating rate (K h^{-1}) averaged over a 1 – 5 km layer for (a) the retrievals (observations) at 1933 UTC 2 August 1997 and (b) the freemode simulation at 0.58 h (valid at observation time).

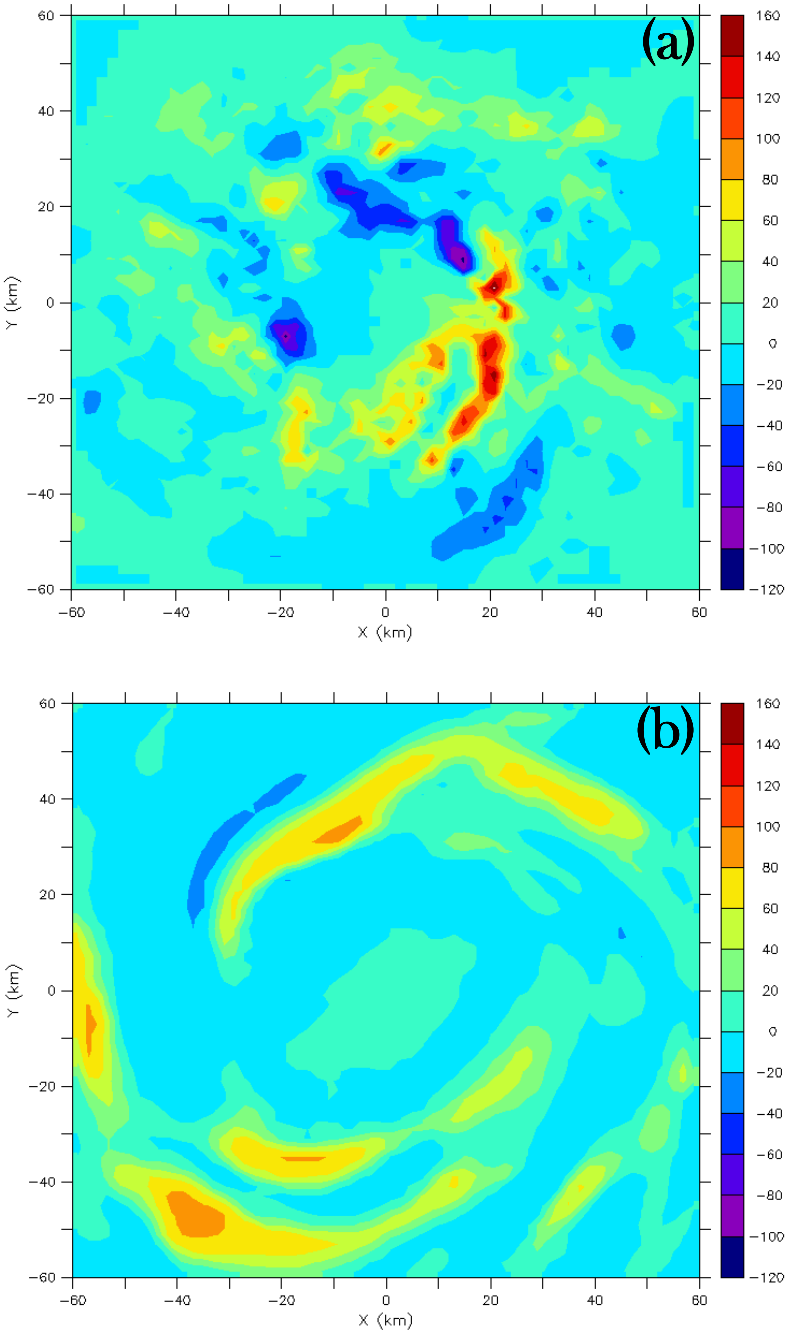

Figure 31. Same as Fig. 30 only for (a) the retrievals (observations) at 2258 UTC 2 August 1997 and (b) the freemode simulation at 4.08 h (valid at observation time).

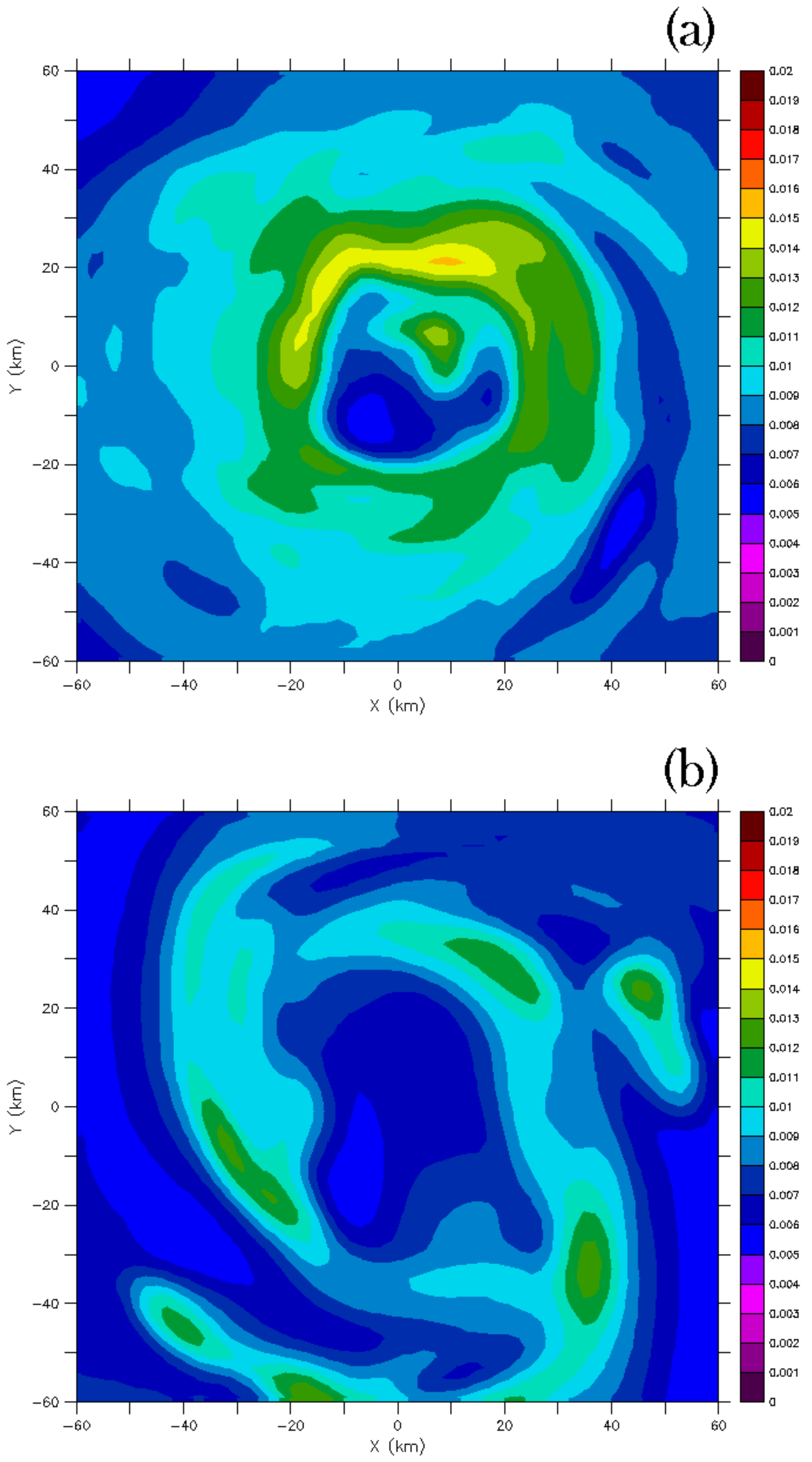

Figure 32. Horizontal cross-sections of water vapor mixing ratio in kg kg^{-1} at 5 km height and 4.67 h into the (a) retrieval and (b) freemode simulations.

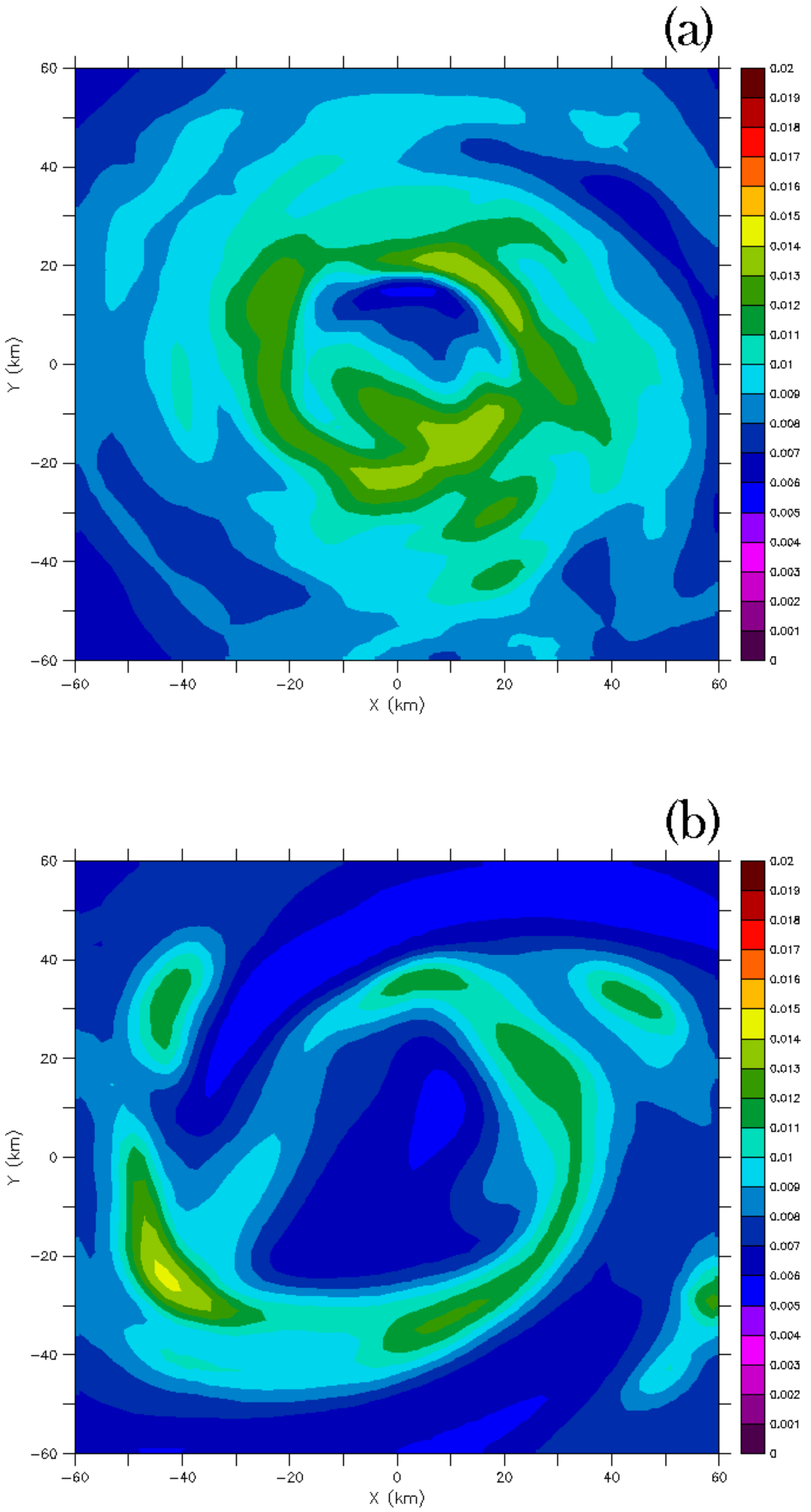

Figure 33. Same as in Fig. 32, only 5.25 h into the simulations.

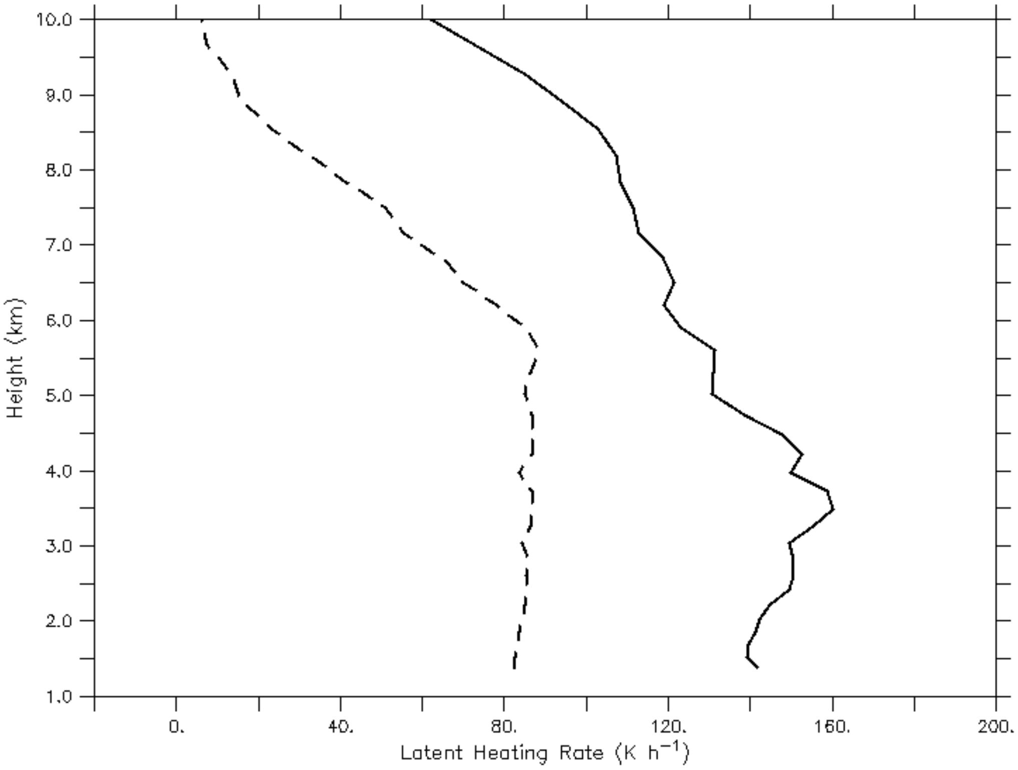

Figure 34. Doppler domain averaged latent heating rates (K h^{-1}) for |w| > 5 m s^{-1}. The solid line shows the LH retrievals while the dashed line shows the results from the model for the observational forcing simulation discussed in the text.

CHAPTER 3

VORTEX DYNAMICS

3.1 Background and Motivation

3.1.1 Symmetric and asymmetric dynamics

The dynamics of TCs can be broken down into two main groups relative to the storm center: axisymmetric and asymmetric. Although the wind and vorticity fields of a TC are highly axisymmetric (Reasor et al. 2000), the forcing (upper-tropospheric Rossby waves and the distribution of convection and LH) is often asymmetric with seemingly disorganized variations in time (Molinari and Vollaro 1989; Nolan et al. 2007). Axisymmetric theories such as the Wind Induced Surface Heat Exchange (WISHE) mechanism focus on mean structure (Emanuel 1986). The secondary circulation is viewed as providing the energy to maintain and intensify the primary circulation against frictional dissipation. Boundary layer radial inflow acquires moist entropy from the underlying warm ocean and through Ekman pumping, deposits this energy aloft where the air turns outward following slantwise, neutrally stratified, angular momentum surfaces. Radiative cooling in the outflow layer causes the air to sink at large radius back to the inflow in the boundary layer. This feedback loop is closely analogous to a Carnot process and is described in a number of papers (Emanuel 1986; Rotunno and Emanuel 1987; Emanuel 1995; Emanuel 1997).

While considerable insight has been gained from the WISHE model, asymmetries associated with eddy angular momentum fluxes, vortex Rossby waves, potential vorticity mixing and vortical hot towers have been shown to be integral to TC intensity and structure change (Emanuel 1997; Montgomery and Kallenbach 1997; Schubert et al. 1999; Montgomery et al. 2006), yet they can only be parameterized in axisymmetric models.

A fundamental part of asymmetric vortex dynamics in the presence of forcing is the so-called "axisymmetrization" process. Early studies of the barotropic, non-divergent vorticity equation using a pseudospectral model by Melander et al. (1987) described how an initially elliptical vortex developed filaments (asymmetries) that decay over time and lead to an end state that relaxes to an axisymmetric structure. This process was dubbed "axisymmetrization" and is recognized as a universal process of smoothly distributed (stable) vortices under the presence of some type of asymmetric forcing (Melander et al. 1987; Montgomery and Kallenbach 1997; McWilliams et al. 2003). Note, that in Melander et al. (1987) a fourth order "hyperviscosity" was added to the vorticity equation to simulate the effects of diffusion on the relaxation process. By conducting a series of sensitivity tests where the viscosity coefficient was increased, they showed that for the simplified flow considered, the axisymmetrization process is essentially inviscid.

The studies of Smith and Montgomery (1995) and Montgomery and Kallenbach (1997) extended the work of Melander et al. (1987) by explaining the dynamics behind the axisymmetrization process and applying the theory to TCs. Physically, a perturbation introduced into a TC-like vortex will be sheared apart by the differential rotation (described by the angular velocity profile) creating filaments or bands of vorticity with fluid parcels that oscillate in the core of the storm with an intrinsic frequency dictated by the basic-state radial potential vorticity gradient. These vortex Rossby waves interact with the mean flow through eddy momentum and heat fluxes causing intensification (for up gradient transport) episodes in TCs (Montgomery and Kallenbach 1997; Montgomery and Enagonio 1998). The above studies showed that vortex development and intensification can occur as the result of asymmetric processes, which is fundamentally distinct from that of symmetric mechanisms such as WISHE.

Localized pulses of convection that often occur during rapid intensification episodes (Heymsfield et al. 2001; Guimond et al. 2010) contain both an azimuthal mean component and a spectrum of higher order wavenumbers (asymmetries). In a series of recent papers, Nolan and Montgomery (2002; NM02), Nolan and Grasso (2003; NG03) and Nolan et al. (2007; NMS07) studied the 3D dynamics of prescribed, linear, symmetric and asymmetric temperature/heating perturbations to baroclinic vortices modeled after realistic TCs. For localized heating, these studies found that the *transformation of energy from the perturbations to the mean vortex is dominated by the projection of the heating onto the symmetric mode with pure asymmetries having a negligible, negative impact on intensification.* This result is in contrast to a large amount of work on the barotropic (2-D) axisymmetrization of non-divergent vorticity perturbations (Smith and Montgomery 1995; Montgomery and Kallenbach 1997; Nolan and Farrell 1999b) and the 3-D analog using balanced potential vorticity perturbations (Montgomery and Enagonio 1998; Moller and Montgomery 2000) where pure asymmetric perturbations always lead to mean vortex intensification. The essential difference of the Nolan et al. studies is that a baroclinic vortex along with temperature/heating perturbations were considered instead of using barotropic vortices with vorticity or potential vorticity perturbations in balance models.

As mentioned in the previous section, heating is the fundamental quantity driving TC dynamics and thus, represents more of the true essence of convection. In addition, in real TCs that posses a warm core (and thus a radial temperature gradient), there is always some degree of baroclinicity to keep the vortex in thermal wind balance. NG03 show that the use of nonhydrostatic temperature perturbations in a baroclinic base state leads to the formation of an up-shear tilt configuration of the potential vorticity anomalies, which extract energy from the mean vortex through down-gradient eddy momentum fluxes (Orr 1907; Farrell 1982). Although some of the energy contained in the perturbations is returned to the vortex through axisymmetrization (up gradient eddy momentum fluxes), there is typically a net sink of energy in the vortex of negligible magnitude (NG03; NMS07). The NG03 results were computed using a linear, anelastic model and verified using a nonlinear, compressible code; the dynamic core of the Weather Research and Forecast (WRF) model (version 1.2.1).

Clearly, the debate on the basic dynamics (symmetric vs. asymmetric) governing TC evolution and intensification is a complex and largely unsolved one although great progress has been (and continues to be) gained from the aforementioned studies. The original goal of the second part of this work was to advance the understanding of the roles played by symmetric and asymmetric vortex dynamics in a fully nonlinear, observational heating regime where the generation of more vertically coherent potential vorticity anomalies may lead to a different tilt configuration and energy partitioning. Early attempts to reproduce the nonlinear (WRF) results of NG03 using a different numerical model revealed discrepancies with the impact of pure asymmetric thermal anomalies. As a result, the work moved in a new, interesting direction. This chapter is now devoted to understanding these differences and there impacts on understanding TC intensification dynamics.

3.1.2 The impacts of diffusion

In order to simulate large Reynolds number, turbulent flows (such as TCs) in a numerical model accurately, it is necessary to resolve all scales of motion from the large energy containing eddies down to the small dissipative ones. The conservation of momentum equation is valid for all of these scales and can be written in Einstein summation notation as,

$$\frac{\partial u_i}{\partial t} + u_j \frac{\partial u_i}{\partial x_j} = -\delta_{i3} g + f \varepsilon_{ij3} u_j - \frac{1}{\rho} \frac{\partial p}{\partial x_i} + \upsilon \frac{\partial^2 u_i}{\partial x_j{}^2} \qquad (15)$$

where u_i is velocity, δ is the Kronecker delta, g is the acceleration due to gravity, f is the Coriolis parameter, ε is the alternating unit tensor, p is pressure, ρ is density and υ is molecular kinematic viscosity. As an extreme case, Bryan et al. (2003) notes that for deep moist convection (and other large Reynolds number flows), a grid spacing of ~ 0.1 mm would be required to resolve the entire energy spectrum. The circulation of TCs can extend out to 500 km radius or more; consequently, using a square model domain of 1000 km on a side with a resolution of 0.1 mm would require 10^{20} grid points for one level of computation, not to mention the very small time step required for numerical stability. Obviously, this scale is well beyond our current computer resource limitations (but not necessarily in the future) and thus, a filtered (or averaged) form of the conservation equations that removes smaller scales must be used to make the problem computer manageable. This conservation of momentum equation takes a similar form to (15),

$$\frac{\partial \overline{u_i}}{\partial t} + \overline{u_j} \frac{\partial \overline{u_i}}{\partial x_j} = -\delta_{i3} g + f \varepsilon_{ij3} \overline{u_j} - \frac{1}{\overline{\rho}} \frac{\partial \overline{p}}{\partial x_i} - \frac{\partial \left(\overline{u_i' u_j'} \right)}{\partial x_j} \ , \qquad (16)$$

only with the removal of molecular viscosity and the addition of a turbulent momentum flux term (last term on the right-hand-side). Note that we only show the Reynolds stress in the turbulent momentum flux term for simplicity. Over bars over all variables in (16) represent the filtered, grid-resolved quantity with the primes denoting sub grid scale fluctuations.

In order to close the equation set, parameterizations for the turbulent fluxes must be derived that play two main roles: (1) to specify the subgrid flux of mass, momentum and energy and (2) to transfer kinetic energy to unresolved scales in order to represent the observed cascade of energy (Stull 1988; Pielke 2002). The process of representing these two roles in numerical models is typically referred to as "explicit diffusion". In addition to explicit diffusion, most numerical models have some degree of noise that originates from the use of approximations (e.g. finite-differences) to the governing equations such as advection (Pielke 2002). Some numerical models add artificial, scale-selective filters to the governing equations to reduce this noise. However, these filters cannot distinguish between the physical signal and the noise in the solution leading to damping of all small scale perturbations. The background noise associated with the numerical approximations as well as artificial filters is often referred to as "implicit diffusion". Naturally, the final solution in a numerical model is dependent on "effective diffusion", which is a combination of *both* implicit and explicit components.

Unfortunately, the effects of implicit diffusion can be significant (Lilly and Jewett 1990; Wiesman et al. 1997) and the parameterizations of explicit diffusion contain large uncertainty resulting in potentially large inaccuracies in the simulated flow (Stull 1988; Pielke 2002). Both Lilly and Jewett (1990) and Wiesman et al. (1997) found that the impacts of implicit diffusion had more effect on simulations of supercell thunderstorms than did the mixing accomplished through the explicit diffusion parameterization. Takemi and Rotunno (2003) using an early version of the WRF model found that adding an artificial numerical filter (fourth-order horizontal diffusion) outweighed the effects of the explicit diffusion parameterization (either a first-order deformation based method or a 1.5 order Turbulent Kinetic Energy (TKE) method using standard values of the mixing coefficients) in terms of spatial noise in their squall line simulations. They also found that in order to avoid using the artificial numerical filter, larger values of the explicit diffusion mixing coefficients are needed to reduce computational noise in the solution arising from numerical approximations. This result implies that there is quasi-conservation of *effective* diffusion between two numerical models with different levels of implicit and explicit diffusion.

Some of the theories on TC structure and intensity change outlined in the previous section are sensitive to diffusive and turbulent properties. For example, Emanuel (1997) described the eyewall as an atmospheric front where the frictionally induced inflow concentrates moist entropy inside the radius of maximum winds (RMW) leading to strong radial gradients in angular momentum. In order for enhanced periods of intensification to occur (i.e. rapid intensification) in the WISHE model, mechanical spin-up of the eye by radial turbulent fluxes of angular momentum from the eyewall is necessary to amplify the entropy gradient. Despite this theoretical finding, there has been very little work on the role of all types of diffusion and turbulence in TCs although recent numerical work has found significant sensitivity of TC structure and intensity to the representation of uncertain aspects of the turbulence parameterization (Braun and Tao 2000; Bryan and Rotunno 2009).

3.2 Axisymmetrization Dynamics

3.2.1 Numerical model, vortex and initialization procedure

The dynamic core of HIGRAD was used to attempt to reproduce the WRF (version 1.2.1) results of NG03. Details of the dynamic core of WRF can be found in Wicker and Skamarock (2002), Takemi and Rotunno (2003), Skamarock (2004) and Klemp et al. (2007). As mentioned in section 2.3.4, HIGRAD solves the 3D, rotating, compressible Navier-Stokes equations written in conservative form and framed in generalized coordinates (Reisner et al. 2005; Reisner and Jeffery 2009). The dry momentum, energy and mass continuity equations for the Cartesian coordinates used here are

$$\frac{\partial\left(u^i\rho\right)}{\partial t}+\frac{\partial\left(u^iu^j\rho\right)}{\partial x^j}=-\frac{\partial p'}{\partial x^j}-g\rho'\delta_{i3}-2\rho\varepsilon_{ijk}\Omega_j\left(u^k-u_e^k\right)+\frac{\partial\left(\kappa\rho\tau^{ij}\right)}{\partial x^j} \tag{17a}$$

$$\frac{\partial(\theta\rho)}{\partial t}+\frac{\partial\left(u^i\theta\rho\right)}{\partial x^i}=\frac{\partial}{\partial x^i}\left(\kappa\rho\frac{\partial\theta}{\partial x^i}\right) \tag{17b}$$

$$\frac{\partial\rho}{\partial t}+\frac{\partial u^i\rho}{\partial x^i}=0 \tag{17c}$$

where Ω represents the components of Earth's rotation axis with $\Omega_1 = 0$, $\Omega_2 = 2\Omega \sin\phi$, $\Omega_3 = 2\Omega\cos\phi$ and $\Omega = 7.292 \times 10^{-5} s^{-1}$ the rotation rate. The subscript e represents environmental values and the stress tensor is expressed as

$$\tau^{ij} = \frac{\partial u^i}{\partial x^j} + \frac{\partial u^j}{\partial x^i} - \frac{2}{3}\frac{\partial u^k}{\partial x^k}\delta_{ij} . \tag{17d}$$

A deformation-based eddy diffusivity scheme (Smagorinsky 1963) was employed that can be written

$$\kappa = 1.8(C_1\Delta_1)^2|S| + C_2\left(\Delta_2{}^2\right) \tag{17e}$$

where $\Delta_1 = (\Delta x \Delta y \Delta z)^{1/3}$, $S = \sqrt{2\tau^{ij}\tau^{ij}}$, $\Delta_2 = \Delta x, \Delta y, \Delta z$ and Δx, for example, represents the grid spacing in the x-direction. The coefficients are $C_1 \approx 1\times 10^{-1}$ and $C_2 = 1\times 10^{-3}\,\mathrm{s}^{-1}$ (in horizontal, 1×10^{-2} s^{-1} in vertical). Several options exist for parameterizing the effects of turbulence and surface layer processes. Generally, a full stress tensor along with a first order deformation-based eddy diffusivity scheme (shown in 17d and 17e) or a 1.5 order TKE scheme is used to represent both surface friction and diffusive tendencies associated with sub-grid scale fluxes in the momentum equations. For the thermodynamic equation (17b), a standard Laplacian operator is used to diffuse potential temperature. Deviations from these procedures will be noted where appropriate.

The discretization of the system of equations in (17) uses a finite volume scheme with all variables existing on collocated ("A-grid"), cell centered grids and derivatives being computed on cell faces (Reisner et al. 2005). The advection scheme employed is the Quadratic Upstream Interpolation for Convective Kinematics (QUICK; Leonard and Drummond 1995) including estimated streaming terms (QUICKEST) and the current setup of HIGRAD uses a semi-implicit approach for advancing in time (Reisner et al. 2005).

To attempt to reproduce the WRF results of NG03, a similar model setup was used in HIGRAD. These include a dry atmosphere, horizontal resolution (2 km), Coriolis parameter (5.0×10^{-5} s^{-1}), time step (20 s) and free slip of momentum and scalars on the lower and upper boundaries to remove frictional effects. Note that free slip was configured here by setting the vertical derivatives of momentum and scalar variables to zero at the lower and upper levels. The same environmental sounding as NG03 was used (mean hurricane season sounding; Jordan 1958) along with similar Newtonian relaxation regions on the sides and top of the model that nudge the fields back towards the environment. Unless stated otherwise, higher vertical resolution (71 levels with stretching to ~ 22 km top) and a much larger domain (1,860 km^2 with 2 km inner resolution stretching out to ~ 20 km on edges) were used in place of the NG03 settings (30 levels stretching to ~20 km and a 600 km^2 domain) in order to minimize spatial errors and boundary effects. In their WRF and linear model simulations, NG03 used very simple values of eddy diffusivity specifying a constant 40 m^2 s^{-1} in all three Cartesian directions. Initially, we also chose simple values of the eddy diffusivity by only including the second term on the right-hand-side of (17e). Considering that a stretched grid was used, values of the eddy diffusivity were 4000 m^2 s^{-1} in the horizontal in the vortex core and ~ 30 – 300 m^2 s^{-1} in the vertical at the heights of the peak velocities. The HIGRAD setup described above represents the control case.

The basic-state vortex was the same as that used in NG03. Following NM02, a vorticity profile that ensures exponential stability (in order to focus exclusively on axisymmetrization) is

$$\zeta(x,y) = A\exp\left[-\left(\frac{r_c}{b}\right)^2\right] \tag{18}$$

where ζ is the vertical component of relative vorticity computed on the Cartesian model domain, $A = 1.5\times10^{-3}s^{-1}$, $b = 45\,\text{km}$ and r_c is radius. The horizontal velocities on the Cartesian mesh are computed by solving Poisson equations with (18) used as forcing

$$\nabla^2 u = -\frac{\partial\zeta}{\partial y} + \frac{\partial\delta}{\partial x} \tag{19a}$$

$$\nabla^2 v = \frac{\partial\zeta}{\partial x} + \frac{\partial\delta}{\partial y} \tag{19b}$$

where δ, the divergence, is equal to zero for the purely non-divergent flow specified. An elliptic partial differential equation solver ("Black Box Multigrid"; Dendy 1982) employing Dirichlet boundary conditions was used to determine the horizontal velocities on the stretched mesh at the first model level. The velocities are extended into the vertical using equation (3.3) of NM02. The above series of steps produces a clean (free of errors, such as wavenumber 4 anomalies, that arise when interpolating from cylindrical to Cartesian grids), stable, baroclinic, tropical storm strength (maximum wind speed of 21.5 m s^{-1} at an RMW of 50 km) vortex that is exactly the same as NG03. See Figs. 1a and 1b in NG03 for plots of the vortex structure.

In order to get a vortex at t = 0 that is balanced with the full model equations in HIGRAD (including the effects of diffusion), the horizontal velocities computed above were added as forcing terms in the momentum equations and nudged according to equation (12) over a ~ 20 h period with a constant coefficient of 10^{-3} s^{-1} (see section 2.3.4 for details). During this period, the potential temperature and density fields that hold the vortex in thermal wind balance are generated. Low amplitude gravity waves (identified by oscillations in the vertical velocity field) propagate throughout the model domain in response to the momentum forcing. However, the gravity wave oscillations are small at the end of the initialization period (~ 20 h) and are dissipated on the sides and top of the domain by the Newtonian relaxation zones. Thus, they should not cause major problems with the numerical solutions. An offline thermal wind balance solver that iterates between gradient and hydrostatic balance (until a convergence threshold is met) revealed that after the ~ 20 h nudging period, the vortex was in near exact thermal wind balance in terms of minimum central pressure (~ 1009.5 hPa; Fig. 35) and potential temperature anomaly (not shown).

3.2.2 Reproducing the results of NG03

After the dynamic initialization period, the nudging is shut off and thermal perturbations are initialized. The first thermal perturbation considered was a 1 K localized, impulsive (initial condition) thermal anomaly with a Gaussian structure in the horizontal (peaking at 40 km radius) and vertical (peaking at 5 km height) described by equation (5.2) in NG03. As mentioned in NG03, diffusion in nonlinear models such as WRF and HIGRAD act on the total flow, which causes the vortex to spin-down over a period of 6 h or more. The small magnitude perturbations (1 K) considered in the nonlinear studies of NG03 to verify their linear predictions were overcome by the effects of diffusion making it difficult to analyze the dynamic response of the heating. In order to isolate the effects of the perturbations and attempt to remove some model artifacts (e.g. boundary condition noise), for each perturbation considered two simulations were run:

one with thermal anomalies and one without. The impacts of the perturbations at each time are then defined to be the difference between the perturbed vortex and the initial (in this case at the end of the ~ 20 h nudging), axisymmetric vortex (NG03).

The minimum pressure perturbation (at the lowest model level of 35 m) for the 1 K localized thermal anomaly over a 6 h simulation in HIGRAD is shown in Fig. 36a with the corresponding plot from the WRF simulations of NG03 in Fig. 36b. In terms of minimum pressure, the two models agree very well with a 6 h pressure perturbation of -0.017 hPa for WRF and -0.019 hPa for HIGRAD. There are some slight differences in Fig. 36 with HIGRAD showing a larger downward spike in pressure at early times and more undulations at later times, but overall the comparisons are very good. Next, the axisymmetric or wavenumber zero (WN0) projection of the 1 K localized thermal anomaly ($\theta = 0.14$ K) was initialized in HIGRAD and the 6 h pressure perturbation was -0.014 hPa, the same value found in WRF (see table 1 in NG03). Furthermore, a 1 K WN0 thermal anomaly peaking at a radius of 40 km and a height of 5 km was initialized in HIGRAD. Figure 37a depicts the minimum pressure perturbation time series for this anomaly in HIGRAD with Fig. 37b showing the same figure from NG03 only using the linear, anelastic model results, which were shown to reproduce WRF almost exactly. An excellent match is again found with HIGRAD in the qualitative and quantitative regimes with a 6 h pressure perturbation of -8.8×10^{-2} hPa in HIGRAD and -9.1×10^{-2} hPa in the linear model.

In terms of velocity, HIGRAD was also able to reproduce the linear model results for the 1 K WN0 anomaly. Figure 38a shows the azimuthal mean tangential velocity at the lowest model level at $t = 6$ h in HIGRAD with 38b showing the same plot in NG03's linear model only at $t = 8$ h. Both plots are very similar even with the 2 h difference in timing (the velocity in HIGRAD at $t = 8$ h was not very different from that at $t = 6$ h). Subtle differences at a radius of $r = 0$ km and $r = 150$ km have to do with different grids (Cartesian for HIGRAD and cylindrical for NG03's linear model) and boundary conditions. Finally, Fig. 39 shows comparisons of the azimuthal mean tangential velocity in the radius-height plane for HIGRAD and NG03's linear model at $t = 4$ h for the 1 K WN0 anomaly. Although the magnitudes are reproduced reasonably well and some of the structure, it is clear that there are differences in terms of changes to the mean vortex.

Other plots from the 1 K WN0 results of NG03 that were reproduced almost exactly with HIGRAD include the axisymmetric, perturbation radial and vertical velocities at t = 10 minutes (not shown).

The plots and discussion above show that for the vast majority of diagnostics, HIGRAD is able to reproduce the results of NG03 for localized and axisymmetric thermal anomalies. However, initializing the basic-state, balanced vortex in HIGRAD with a 1 K wavenumber three (WN3) thermal anomaly resulted in a large discrepancy in terms of minimum pressure perturbations with the results of NG03. Figure 40 shows the time series of minimum pressure perturbation for this anomaly in HIGRAD and WRF. The differences are very large not only quantitatively (6 h values of -2.7×10^{-2} hPa for HIGRAD and 4.1×10^{-4} hPa for WRF), but also qualitatively as the pressure spikes at early times (less than 1 h) are nearly opposite of each other with slightly different structure. Comparing the impacts of axisymmetric and asymmetric thermal anomalies (for the same magnitude and location) in each model by taking the ratio WN0/WN3 at 6 h yields ~ -222 in WRF and ~ 3 in HIGRAD. Note the impacts of axisymmetric heating will always be larger than those from asymmetric heating (for the same magnitude and location) because of the larger integrated energy input for the axisymmetric case.

A large number of sensitivity tests were conducted to examine the potential cause of the discrepancy with the asymmetric results of NG03. These include using different domains and resolutions, changes to the boundary conditions and upper gravity wave absorber, initialization procedures, different wavenumber perturbations and locations (in radius and height) as well as types and amounts of explicit diffusion. A summary of the most relevant sensitivity tests in terms of minimum pressure perturbation at 6 h are shown in Table 2 with the first line showing the control case and all others changes to the control. Many of the tests listed above had very little impact on the solutions and are not included in Table 2. These include using a different domain size (600 km^2), horizontal resolution (4 km), specification of free slip (setting the vertical component of the diffusive tendencies for both the stress tensor and Laplacian operator to zero at the boundaries), time step (2 s), method of initialization (using the *exact* balanced vortex fields of NG03), eddy diffusivity for potential temperature (40 $\text{m}^2\ \text{s}^{-1}$) and widths of side and upper relaxation zones. Note that minimum pressure was used to report the results of the sensitivity tests because it represents an integrated quantity and thus is the best single measure of overall changes to the vortex. This is consistent with the methods of NG03 as well.

Table 2 shows that for the same linear heating magnitude (1 K), not a single sensitivity test conducted even came close to reproducing the results of NG03 in terms of order of magnitude. That is, HIGRAD was still two orders of magnitude larger than the linear and nonlinear (WRF) results of NG03. Initializing with thermal anomalies of larger magnitude (4 K; approaching nonlinear regime) in an attempt to increase the signal to noise ratio still showed the ratio WN0/WN3 of around 3. The largest sensitivities in Table 2 are due to the type and amount of explicit diffusion for momentum with some small differences attributed to number of vertical levels. When using the same, constant eddy diffusivity values as specified in NG03 (40 $m^2 s^{-1}$), HIGRAD produced further departures, creating a stronger vortex. Interestingly, employing a Laplacian diffusion operator to the momentum variables changed the sign on the pressure perturbation from negative to positive, but the magnitude did not change much. The fact that nearly all the pressure values in Table 2 are negative was not as alarming as the discrepancies with the magnitudes since NG03 and NMS07 found some changes in sign for different anomaly structures in space and/or time.

Given the ability of the present analyses to reproduce the axisymmetric results of NG03 but not the asymmetric ones, the reader might wonder if an error existed in the construction of the asymmetric thermal anomalies. However, extensive examination of the thermal asymmetries showed the correct magnitude and structure with zero projection onto the azimuthal mean. Furthermore, an exact reproduction of NG03's vertical velocities at 5 km height and t = 30 min for the WN3 anomaly (see their Fig. 20a) was produced with HIGRAD. The construction of the thermal anomalies was not the reason for the differences in the asymmetric results.

Initial comparisons of the perturbation vertical vorticity field (5 km height and t = 2 h) generated from the WN3 thermal anomaly showed surprisingly good agreement between HIGRAD (Fig. 41a) and WRF (Fig. 41b) although the peak values were different by about a factor of two. For this comparison, the control setup was used in HIGRAD (described above). As previously stated, the WRF results of NG03 used a constant value of eddy diffusivity (40 m^2 s^{-1}) in all three Cartesian directions, which may lead one to the conclusion that explicit diffusion was not playing a large role in the generation of vorticity. However, setting the same eddy diffusivity values as NG03 in HIGRAD produced completely different vorticity magnitude and structure shown in Fig. 42a. The WN3 vorticity anomaly that might be generated from the WN3 thermal considered is not recognizable in this figure. Instead, the vorticity field looks noisy with values that are almost an order of magnitude larger than those from NG03's WRF simulations (Fig. 41b). By increasing the eddy diffusivity from 40 m^2 s^{-1} in all directions (Fig. 42a) to 100 m^2 s^{-1} (Fig. 42b) and 200 m^2 s^{-1} (Fig. 42c) the fields are smoothed out and the structure of the WN3 vorticity anomaly begins to appear. Since the same eddy diffusivity value (40 m^2 s^{-1}; for momentum and energy) used in NG03's WRF simulations was set in HIGRAD and a similar diffusion operator was in use in both models, *this result suggests that the implicit diffusion in WRF is far different than that in HIGRAD.* Indeed, we had to use eddy diffusivity values that were two orders of magnitude larger in the horizontal and up to an order of magnitude or larger in the vertical to produce vorticity anomalies with the same structure and similar magnitudes as those in WRF.

Figure 43 summarizes the impact of explicit diffusion in HIGRAD for the 1 K WN3 thermal anomaly. The domain integrated palinstrophy (a measure of the vorticity gradient; Schubert et al. 1999; Kossin and Schubert 2003),

$$\mathrm{P} = \int_{0km}^{10km} \int_{-100km}^{100km} \int_{-100km}^{100km} \frac{1}{3}\left(\vec{\nabla}\zeta' \bullet \vec{\nabla}\zeta'\right) dxdydz\,, \tag{20}$$

was computed in order to document the formation of vorticity anomalies for different values of the eddy diffusivity. The primes in (20) represent perturbation quantities and the integrations were done over a smaller domain, focused on the inner core of the vortex. Figure 43 displays the maximum palinstrophy over the 6 h simulation (shown on a log scale) as a function of the 6 h pressure perturbation for each diffusion case. A near linear relationship between the palinstrophy and minimum pressure perturbation is evident in this figure. As the eddy diffusivity values increase from 40 to 800 m^2 s^{-1}, the vorticity anomalies that are generated get smoothed out (smaller palinstrophy), which leads to a weakening of the basic-state vortex.

The relationship to the intensity of the axisymmetric vortex can be understood in terms of the azimuthally averaged tangential momentum equation. For two-dimensional, non-divergent, inviscid flow, Montgomery and Kallenbach (1997) showed that the main effect of vortex Rossby waves on the axisymmetric vortex was accomplished through radial fluxes of vorticity,

$$\frac{\partial \bar{v}}{\partial t} = -\frac{1}{r}\overline{u'\frac{\partial rv'}{\partial r}} = -\overline{u'\zeta'} \,. \tag{21}$$

From this point forward, u and v represent the radial and tangential velocities, respectively, the over-bars represent azimuthal means and the primes denote azimuthal eddies. Although the flow here is more complicated because of three-dimensional, divergent and diffusive effects, equation (21) is still useful for interpreting the results of Fig. 43. Smaller values of the eddy diffusivity were shown to produce larger values and gradients of vorticity which, for all else being equal, will result in a larger spin-up of the axisymmetric vortex; hence the larger pressure perturbations.

The sensitivity tests shown above highlight the significant impacts the eddy diffusivity can have on the generation of vortex Rossby waves and their feedbacks onto the axisymmetric vortex in the HIGRAD model. Bryan and Rotunno (2009), using an axisymmetric numerical model, found similar vortex intensification sensitivity to an analogous parameter in the explicit diffusion parameterization, the turbulent length scale. Larger values of the turbulent length scale correspond to greater turbulence intensity and were found to weaken the radial gradients of angular momentum. Despite the similarities with Bryan and Rotunno (2009), our results seem to stand in contrast with the study of Melander et al. (1987). For simplified flows (barotropic, non-divergent) using a fourth-order “hyperviscosity” operator for diffusion, Melander et al. (1987) concluded that the axisymmetrization process was essentially an inviscid mechanism. The inclusion of unbalanced dynamics, the three-dimensional nature of the flow considered as well as different operators for diffusion present in our analysis (the hyperviscosity used by Melander et al. 1987 is more scale-selective than that used in HIGRAD—stress tensor or Laplacian) could explain the differences with the Melander et al. (1987) study. However, we note that Melander et al. (1987) analyzed the effects of dissipation by computing the timescale for relaxation towards axisymmetry, which has not been computed yet for the present work. In addition, for low values of the eddy diffusivity (40 $m^2 s^{-1}$), HIGRAD seemed to produce computational noise arising from finite-difference schemes and the chosen co-located grid although continued sensitivity was found outside of the apparently noisy regime.

The large differences in the perturbation vorticity between HIGRAD and WRF for the exact same value of the eddy diffusivity (and a similar diffusion operator) indicate that the implicit diffusion between the two models is very different. As mentioned in Takemi and Rotunno (2003) and Skamarock (2004), the WRF model employs a few different dissipation mechanisms to control computational noise. These include horizontal divergence damping and dissipation inherent in the upwind-biased advection scheme employed with a coefficient proportional to the local Courant number (Wicker and Skamarock 2002; Takemi and Rotunno 2003; Skamarock 2004). The HIGRAD model does not include any divergence damping and the apparently less diffusive numerical solution procedure (which includes among others, the QUICKEST advection scheme; Leonard and Drummond 1995) would then require the explicit diffusion to play a larger role to produce similar results to WRF at the same grid spacing. This is consistent with Fig. 41, where an eddy diffusivity value that was two orders of magnitude greater in the horizontal and up to an order of magnitude or greater in the vertical was needed to produce similar vorticity (magnitude and structure) to that from WRF. Given the uncertainty associated with the parameterization of sub-grid scale processes (for the scales here, mainly turbulence) in numerical models and the significant sensitivity of the axisymmetrization process to factors that define those parameterizations (eddy diffusivity) described in this section, research into the role of turbulence in TC inner-core dynamics may prove fruitful.

More importantly, this section revealed that the vast majority of the localized and axisymmetric thermal anomaly results of NG03 were reproducible by HIGRAD, but large discrepancies (in terms of magnitude and structure) with the impacts of purely asymmetric thermals were found. A large set of sensitivity tests revealed that none of the analyzed configurations of HIGRAD could reproduce the WRF (and linear model) results of NG03. A natural question to ask is: what are the physics responsible for these differences? And, what is the role of asymmetric convection in TC intensification?

3.2.2 Understanding the discrepancies with NG03

To understand the differences between the results of NG03 (specifically, the WRF simulations) and HIGRAD in terms of the impact of the asymmetric mode, budgets for absolute angular momentum (AAM) were performed. The axisymmetric, AAM equation taking into account the vertical and radial variations in density is

$$\frac{\partial \overline{M_a}}{\partial t} = -\frac{1}{\overline{\overline{\rho}} r}\frac{\partial\left(r\overline{\rho}\,\overline{u}\,\overline{M_a}\right)}{\partial r} - \frac{1}{\overline{\overline{\rho}}}\frac{\partial\left(\overline{\rho}\,\overline{w}\,\overline{M_a}\right)}{\partial z} - \frac{1}{\overline{\overline{\rho}} r}\frac{\partial\left(r\overline{\rho}\,\overline{u'M'_a}\right)}{\partial r} - \frac{1}{\overline{\overline{\rho}}}\frac{\partial\left(\overline{\rho}\,\overline{w'M'_a}\right)}{\partial z} + r\overline{D_\lambda} \quad (22)$$

where $\overline{M_a} = r\overline{v} + \frac{f_o r^2}{2}$ is the absolute angular momentum, f_o is the constant Coriolis parameter (5.0×10^{-5} s^{-1}) and D_λ represents the azimuthal component of explicit diffusion. The term on the left-hand-side is the storage of AAM, the first two terms on the right-hand-side are the axisymmetric flux divergences of AAM, the third and fourth terms are the eddy flux divergences and the fifth term is the axisymmetric diffusion of angular momentum. All terms are computed by interpolating the HIGRAD data output at ten minute intervals to a cylindrical grid with radial and azimuthal grid spacing consistent with the native simulation. The storage term was computed by differencing the axisymmetric AAM with a 6 h time separation and all other terms were averaged over a 6 h window with output every ten minutes.

Figure 44a shows a representative vertical profile of the storage term inside the RMW for the simulation with just the basic-state vortex—no perturbations were added. At low (upper) levels the vortex was spinning up (down), which was a result of the explicit diffusion (surface friction was disabled by specifying the free slip condition) shown in Fig. 44b along with the other terms from equation (22). Note that the large spike in diffusion above 18 km height is due to the gravity wave absorption layer. Also, note that the negative signs in front of the flux divergence terms in (22) have been included in Fig. 44b. A surprising result from Fig. 44b was that an axisymmetric, secondary circulation existed in the basic-state vortex over the 6 h simulation shown by the significant radial (black line) and vertical (red line) flux divergence terms. This was surprising because we ensured the model was setup properly to effectively reduce circulations of this type by specifying free slip lower/upper boundaries and eliminating all forcings (such as heating) in the basic-state vortex. Furthermore, we used the exact same initial vortex as NG03 where secondary circulations were not considered.

How significant was the secondary circulation produced in HIGRAD? If we consider the secondary circulation in the basic-state vortex as “noise”, then the “signal” might be the circulation produced from a 1 K WN0 thermal anomaly. Figure 45 shows the AAM terms from the right-hand-side of equation (22) for a 1 K WN0 thermal anomaly centered at 40 km radius and 5 km height. The terms in Fig. 45 represent perturbation quantities. They are computed by subtracting the terms calculated from a simulation with no thermal anomalies from those with the thermal anomaly. Comparing the magnitudes of the axisymmetric radial and vertical AAM flux divergence terms from Fig. 44b and Fig. 45, reveals that the secondary circulation in the basic-state vortex (“noise”) is about twice as strong as the one produced from the 1 K WN0 anomaly (“signal”) and thus, quite significant.

The successful reproduction of many of NG03’s axisymmetric anomaly results indicates that the dynamic response to this perturbation is not overly sensitive to the basic-state secondary circulation. However, the departures observed in Fig. 39, for instance, are likely a result of this circulation, which was largely not considered by NG03. The dynamic response to asymmetric thermal anomalies appears *very* sensitive to the basic-state secondary circulation. Figure 46 shows terms from the AAM equation for the 1 K WN3 thermal anomaly at 30 minutes into the simulation. The storage term (Fig. 46a) reveals a large region of intensifying tangential winds at lower levels and near the radius where the thermal was initialized (40 km). The vast majority of the spin-up in the AAM field is controlled by the *net* axisymmetric flux divergence term (Fig. 46b) with very similar structure and magnitudes as the storage term. The net asymmetric flux divergence term was an order of magnitude smaller than the axisymmetric term with similar magnitudes to the diffusion term (Fig. 46c) and shows indications of gravity waves propagating through the region.

Figure 47 shows the AAM terms for the 1 K WN3 thermal anomaly at 60 minutes into the simulation. A similar story to that at 30 minutes was evident with the net axisymmetric flux term (Fig. 47b) dominating the storage of AAM (Fig. 47a). The net asymmetric flux term (Fig. 47c) decayed by almost an order of magnitude in 30 minutes although gravity waves propagating both radially and vertically out of the domain were still evident at upper levels. The terms at later times (up to 6 h) were similar to those discussed here.

These results show that the net axisymmetric tendencies are doing the vast majority of the work in intensifying the axisymmetric vortex throughout the 6 h simulation as early as 10 minutes into the run (not shown). The study of NG03, using the azimuthal eddy flux tendencies generated from the thermal asymmetry as forcing in an axisymmetric linear model, showed different results. At 30 minutes into their simulations, the changes to the axisymmetric tangential wind (their Fig. 11c) had some asymmetric signatures caused by the azimuthal eddy fluxes (their Fig. 9b and 9e), which was not observed in the present study. Note that the perturbed vortex analyzed in NG03 also developed secondary circulations caused by the response to the azimuthal eddy flux forcing. However, these secondary circulations take a period of time to play a role in the evolution of the thermal asymmetry and axisymmetric vortex whereas for our case, they are important immediately.

The fundamental difference between our results and those of NG03 is the presence of a significant secondary circulation in the basic-state vortex, which is likely responsible for the discrepancies with the impacts of purely asymmetric thermal anomalies. As mentioned above, the model was setup properly to effectively reduce any secondary circulations and the exact same initial vortex as NG03 was utilized. What, then, is the cause of the significant secondary circulation in the basic-state vortex? To answer this question, radial momentum budgets were performed. The axisymmetric radial momentum equation is

$$\begin{aligned}\frac{\partial \overline{u}}{\partial t} = &-\frac{1}{\overline{\rho} r}\frac{\partial\left(r\overline{\rho}\,\overline{u}^{2}\right)}{\partial r}-\frac{1}{\overline{\rho} r}\frac{\partial\left(r\overline{\rho}\,\overline{w}\,\overline{u}\right)}{\partial z}-\frac{1}{\overline{\rho} r}\frac{\partial\left(r\overline{\rho}\,\overline{u'^{2}}\right)}{\partial r}-\frac{1}{\overline{\rho} r}\frac{\partial\left(r\overline{\rho}\,\overline{w'u'}\right)}{\partial z}+\frac{\overline{v'^{2}}}{r}\\ &+\frac{\overline{v}^{2}}{r}+f_{o}\overline{v}-\frac{1}{\overline{\rho}}\frac{\partial \overline{p}}{\partial r}+\overline{D_{r}}\end{aligned}, \qquad (23)$$

where D_r represents the radial component of explicit diffusion. A simulation using a Laplacian operator for diffusion of momentum variables, a constant eddy diffusivity of 500 $m^2\ s^{-1}$ and NG03's exact initial conditions (no nudging initialization) was run in order to simplify the interpretation of the radial flow. The first five terms on the right-hand-side of (23) were found to be very small, which is consistent with the real-data case studies of Molinari et al. (1993). The approximate form of the radial momentum equation reduces to

$$\frac{\partial \overline{u}}{\partial t} \cong \frac{\overline{v}^2}{r} + f_o \overline{v} - \frac{1}{\overline{\rho}} \frac{\partial \overline{p}}{\partial r} + \overline{D_r}\,. \tag{24}$$

Figure 48 shows the terms in (24) along with the tangential component of diffusion averaged over the 6 h simulation (the storage term was computed using a 6 h time difference). The storage of radial momentum is a small signal relative to the other terms for the 6 h period, but the other terms reveal that diffusion of momentum is responsible for the significant, secondary circulation in HIGRAD's basic-state vortex. Specifically, the tangential component of diffusion generates a gradient wind imbalance, which drives a radial flow. Initially, the radial flow is entirely a result of the tangential diffusion but after a period of time, the flow is acted on by the radial component of diffusion which further alters the evolution. Mass continuity requires the axisymmetric radial flow to generate an axisymmetric vertical flow.

The radial velocities at 30 minutes into the HIGRAD simulation described above are shown in Fig. 49a along with the corresponding velocities in the WRF simulations of NG03 (Fig. 49b;courtesy of David Nolan). The radial velocity field is very similar in structure between the two models, but the magnitudes are about an order of magnitude larger in the HIGRAD simulation. Interestingly, using a stress tensor for diffusion of momentum variables in HIGRAD created an inflow layer at lower levels (not shown) whereas using a Laplacian operator generated an outflow layer as seen in Fig. 49a. These differences in the low-level inflow of the basic-state vortex appear to dictate the sign of the pressure perturbation when a thermal asymmetry is added to the vortex (Table 2), which is consistent with the transport of angular momentum.

As shown in Fig. 41, in order for HIGRAD to produce similar perturbation vorticity to that from WRF, eddy diffusivity values around 4000 m^2 s^{-1} were required. However, these same large values (500 m^2 s^{-1} for the simulations above) generate significant, axisymmetric secondary circulations in the basic-state vortex which can corrupt the comparisons to the idealized study of NG03. Specifying smaller values of the eddy diffusivity (like those used in NG03) lead to noisy, unnatural results. For idealized vortex studies that require reduced or insignificant secondary circulations, the current setup of HIGRAD may not be the ideal choice. However, for more realistic studies that include significant secondary circulations, HIGRAD could be the ideal choice given the large, inherent uncertainty associated with effective diffusion in numerical models.

Table 2. Summary of model sensitivity tests examining the impact of impulsive thermal anomalies in HIGRAD. The first line of the table (italics) shows the settings for the control case. Other settings for the control case are listed in the text and were found to have little impact on the results. All other lines shown in the table represent the changes that were made to the control case. Abbreviations not listed in the text are as follows: Kxyz = eddy diffusivity in three Cartesian directions ($m^2 s^{-1}$), GS = eddy diffusivity using the 2nd term on the right of (17e), GS+SMAG = eddy diffusivity using all of (17e), ST = stress tensor diffusion for momentum, LD = Laplacian diffusion for momentum, L = vertical levels. Numbers in parentheses after thermal anomalies show locations in radius/height (km). Note that the control case used a large domain (1800 km^2) while some of the sensitivity tests shown below used a small domain (600 km^2). However, the differences were negligible (< 10%).

Model configuration	**p′ (hPa) at 6 h**
1 K WN3 (r = 40/z = 5), Kxyz = GS, ST, 71 L	*-2.7×10^{-2}*
1 K WN3 (r = 80/z = 7)	-2.1×10^{-2}
Kxyz = GS+SMAG	-3.4×10^{-2}
Kxyz = 40	-5.0×10^{-2}
1 K WN1, Kxyz = 40	-5.1×10^{-2}
30 L	-3.1×10^{-2}
90 L, Kxyz = 40	-4.7×10^{-2}
Kxyz = 150, LD, 30 L	1.4×10^{-2}
4 K WN3 (r = 40/z = 5), Kxyz = 40	-2.5×10^{-1}
4 K WN0 (r = 40/z = 5), Kxyz = 40	-8.4×10^{-1}

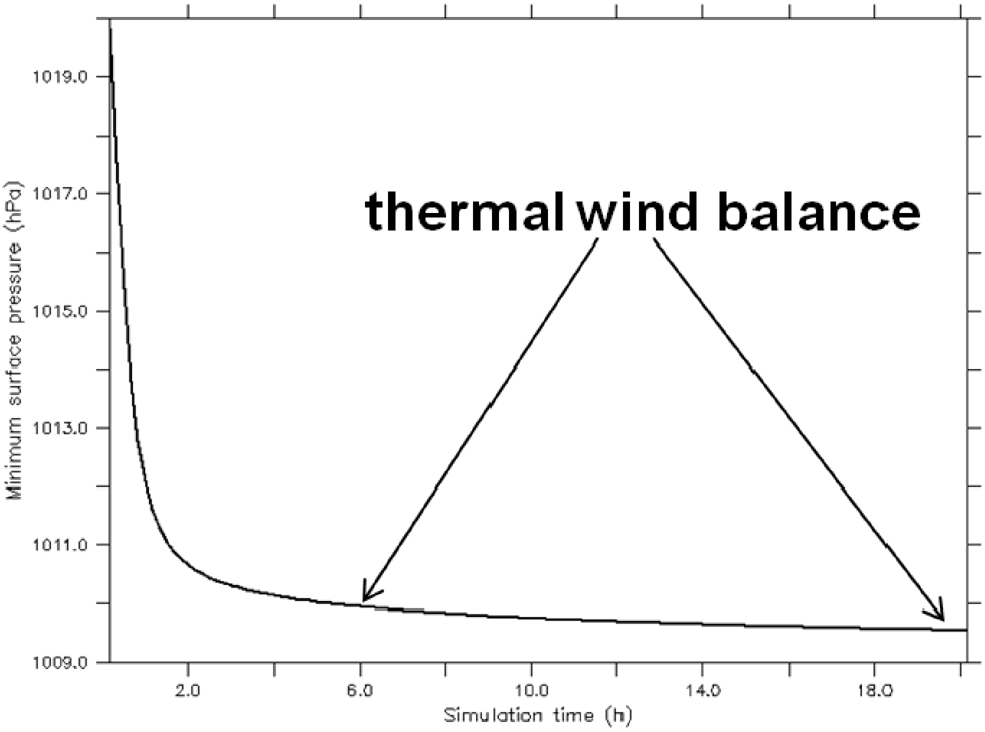

Figure 35. Time series of the minimum pressure in HIGRAD for the dynamic initialization of the NG03 tropical storm vortex.

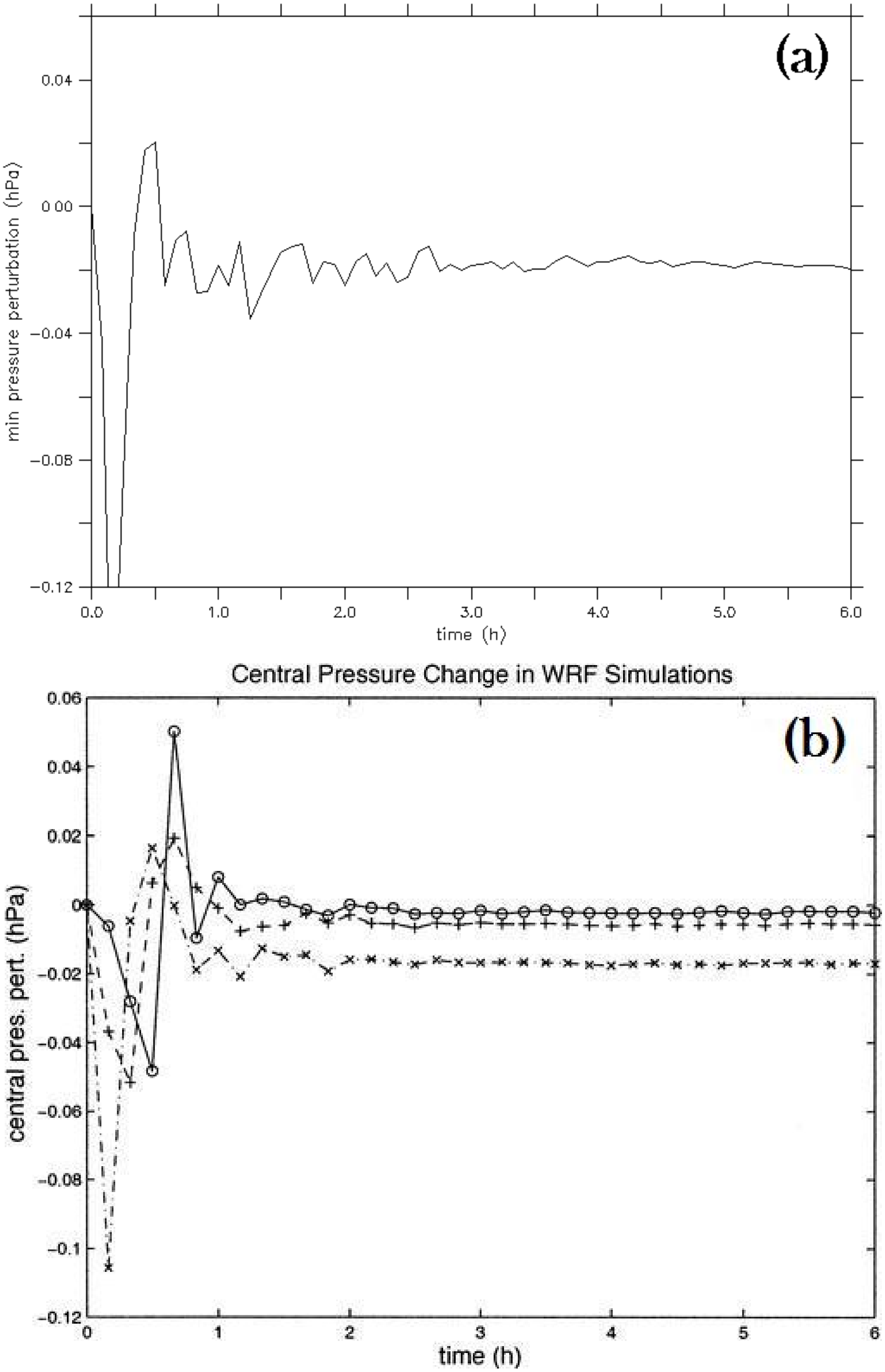

Figure 36. Time series of minimum pressure perturbation (hPa) at the lowest model level for a 1 K localized thermal anomaly centered at 40 km radius and 5 km height. (a) HIGRAD simulation and (b) WRF simulation from NG03 (see dash-dot line with Xs). Used with permission of the AMS.

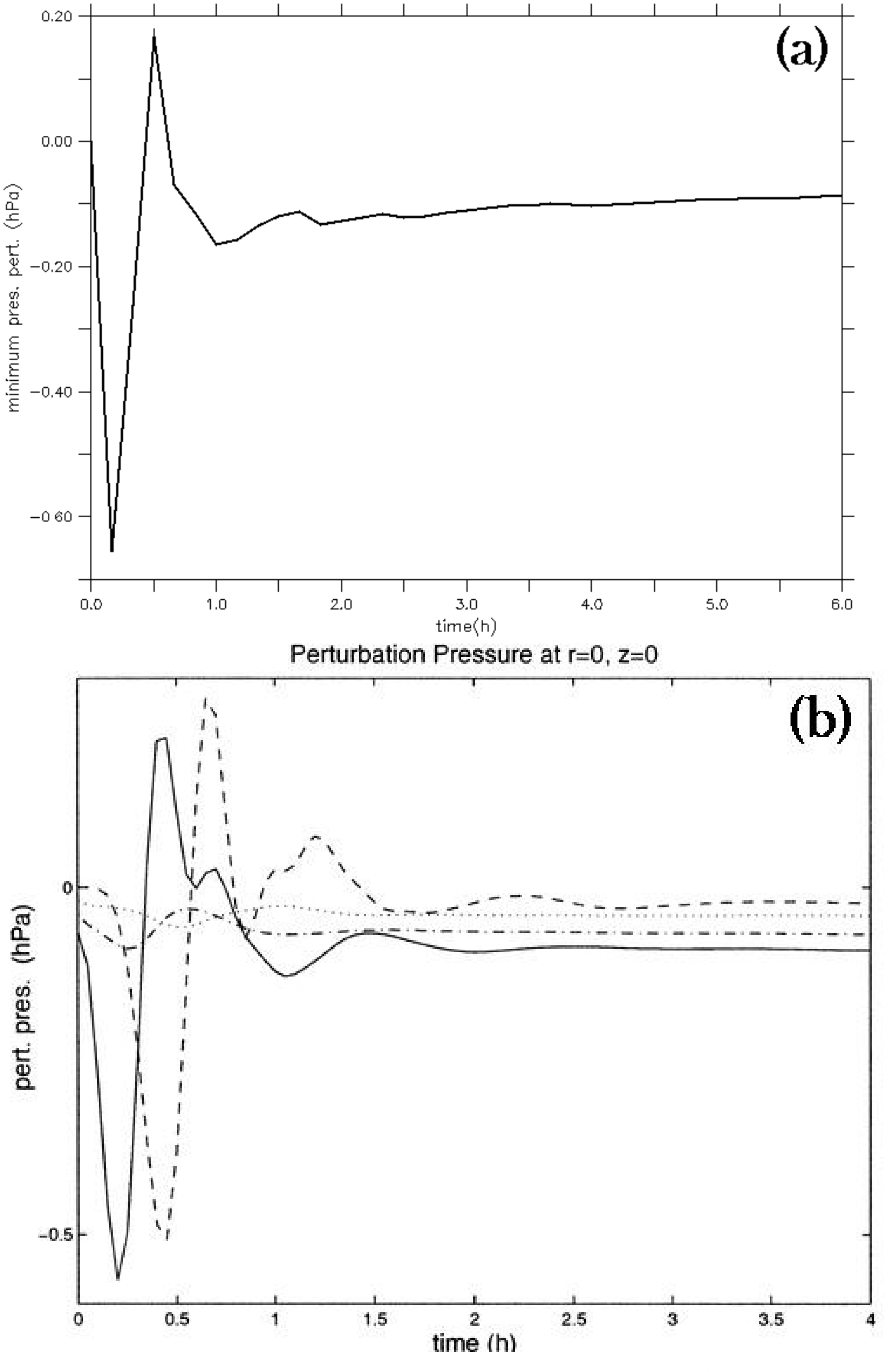

Figure 37. Time series of minimum pressure perturbation (hPa) at the lowest model level for a 1 K symmetric (WN0) thermal anomaly centered at 40 km radius and 5 km height. (a) HIGRAD simulation and (b) linear, anelastic simulation from NG03 (see solid line). Used with permission of the AMS.

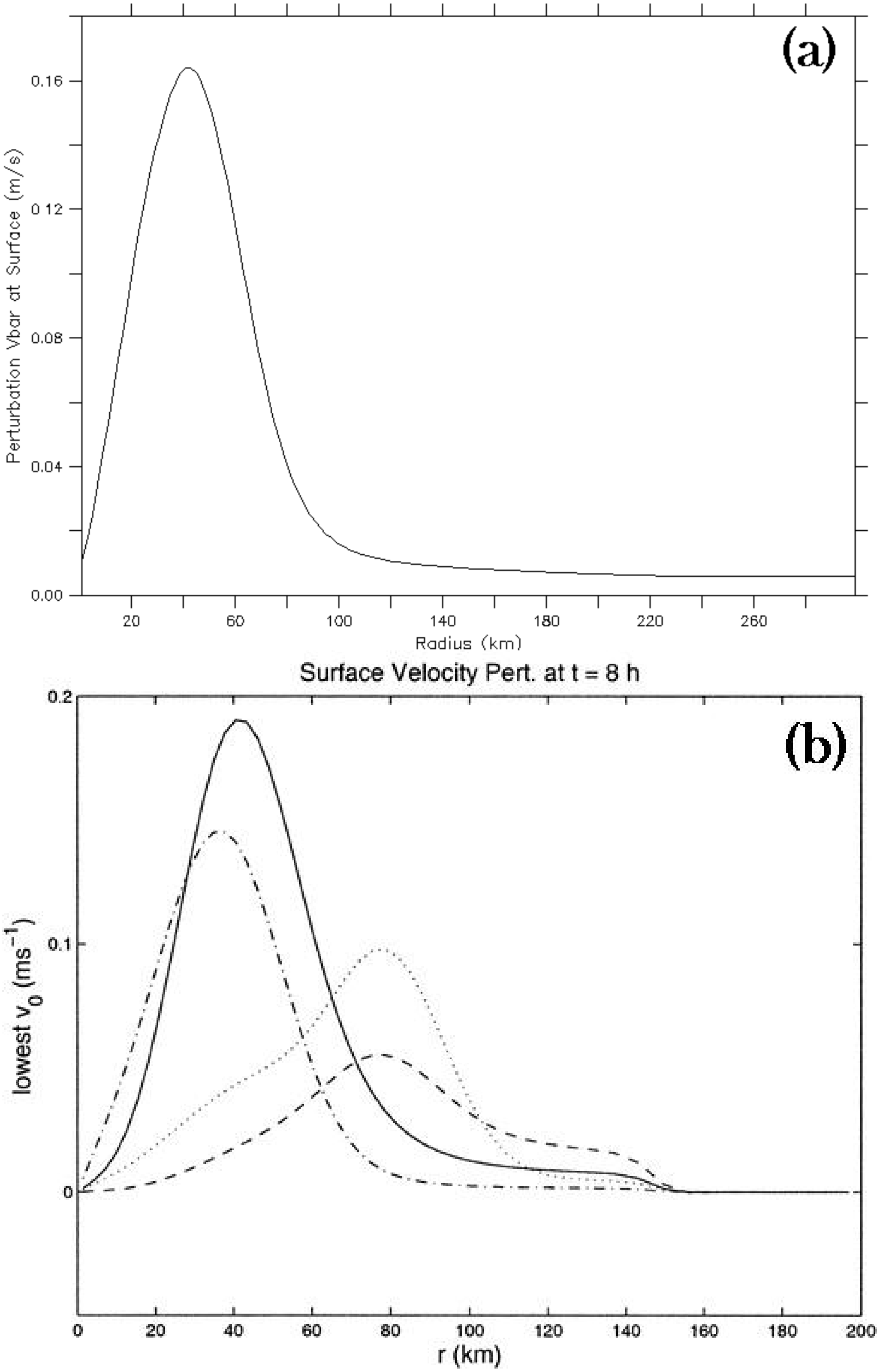

Figure 38. Azimuthal mean tangential velocity perturbation for a 1 K symmetric (WN0) thermal anomaly centered at 40 km radius and 5 km height. (a) HIGRAD simulation at t = 6 h and (b) linear, anelastic simulation from NG03 (see solid line) at t = 8 h. Used with permission of the AMS.

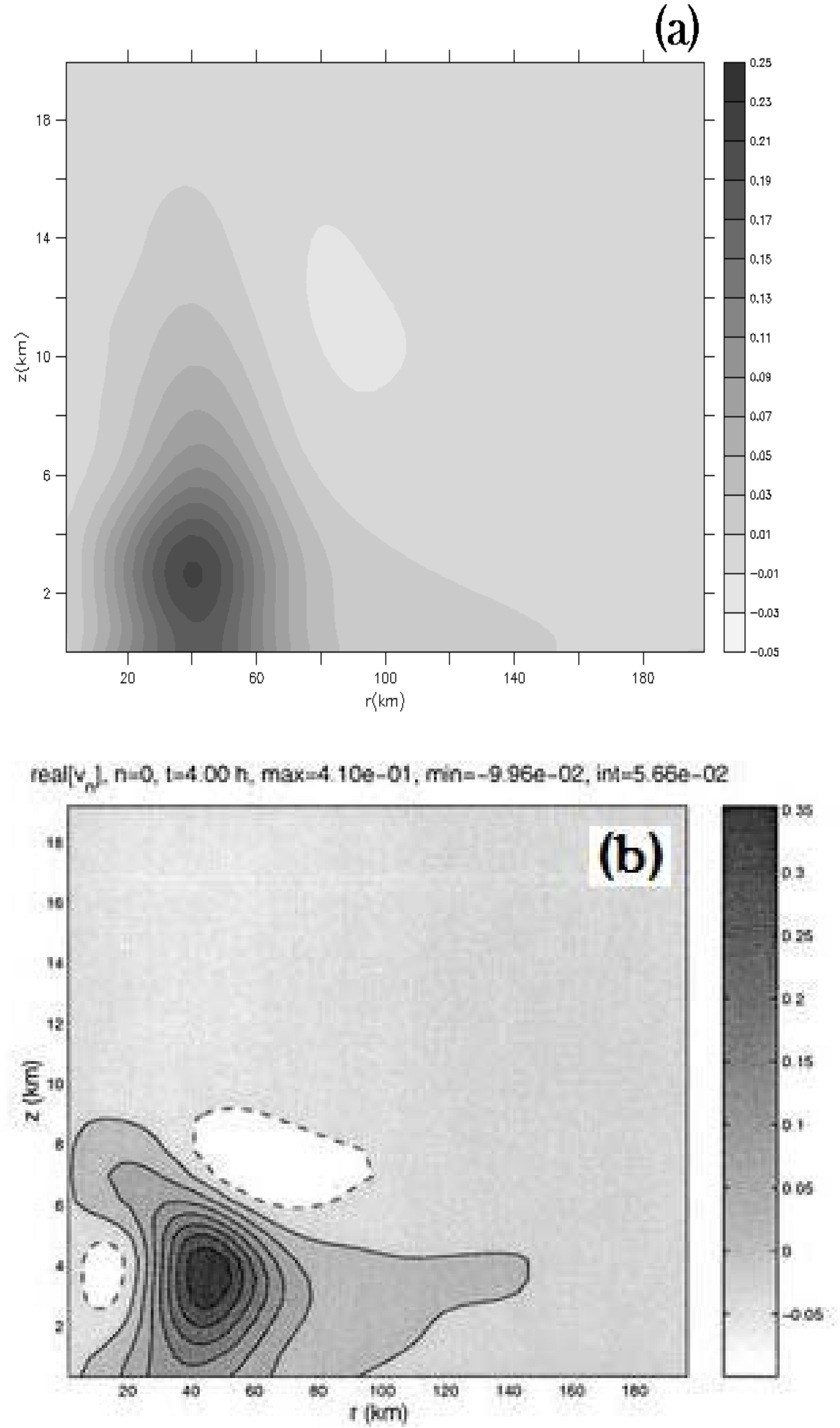

Figure 39. Azimuthal mean tangential velocity perturbation for a 1 K symmetric (WN0) thermal anomaly centered at 40 km radius and 5 km height at t = 4 h (a) HIGRAD simulation and (b) linear, anelastic simulation from NG03. Used with permission of the AMS.

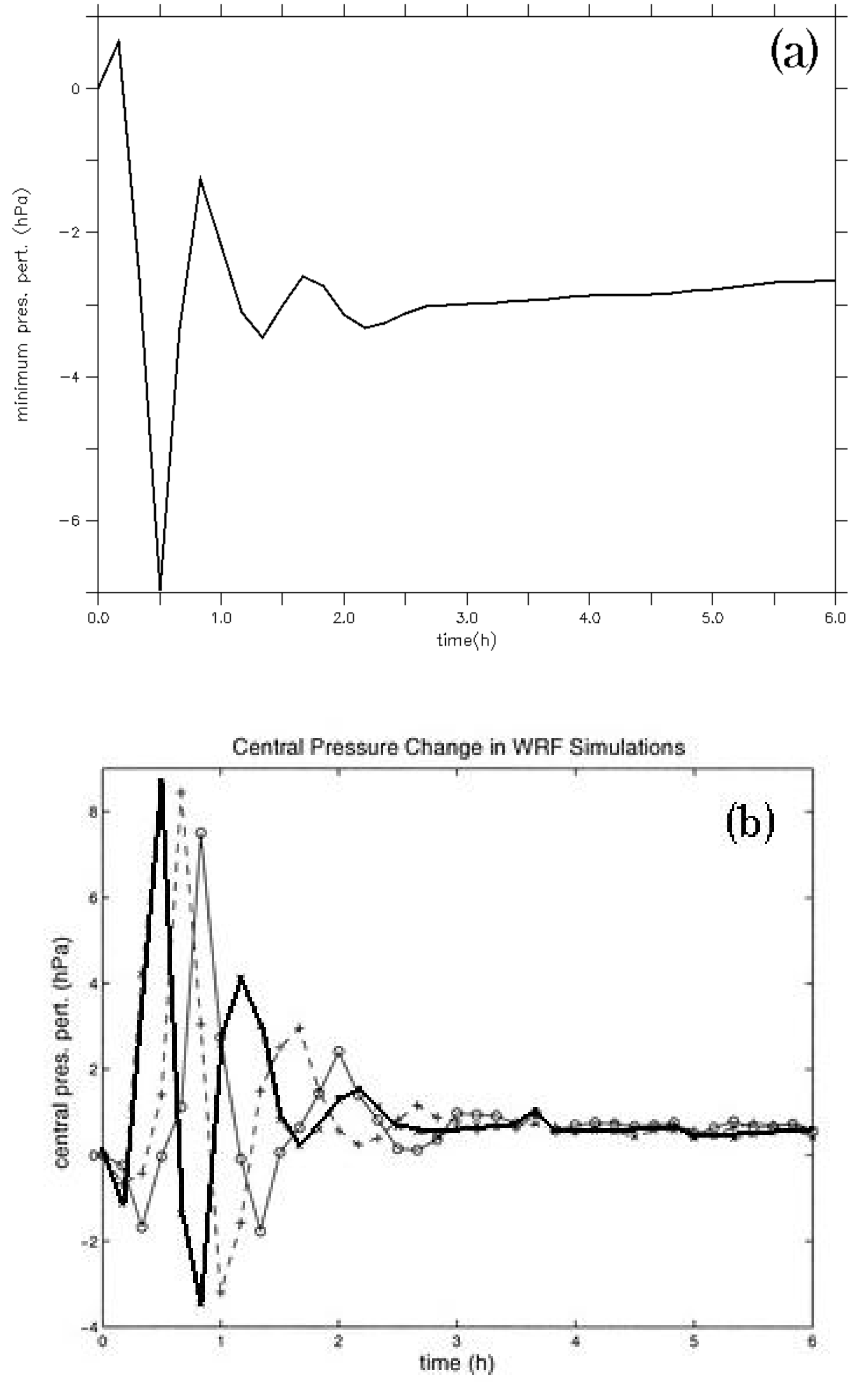

Figure 40. Time series of minimum pressure perturbation (hPa) at the lowest model level for a 1 K asymmetric (WN3) thermal anomaly centered at 40 km radius and 5 km height. (a) HIGRAD simulation (values are ×10^{-2}) and (b) WRF simulation (values are ×10^{-3}) from NG03 (see thick, solid line added to figure). Used with permission of the AMS.

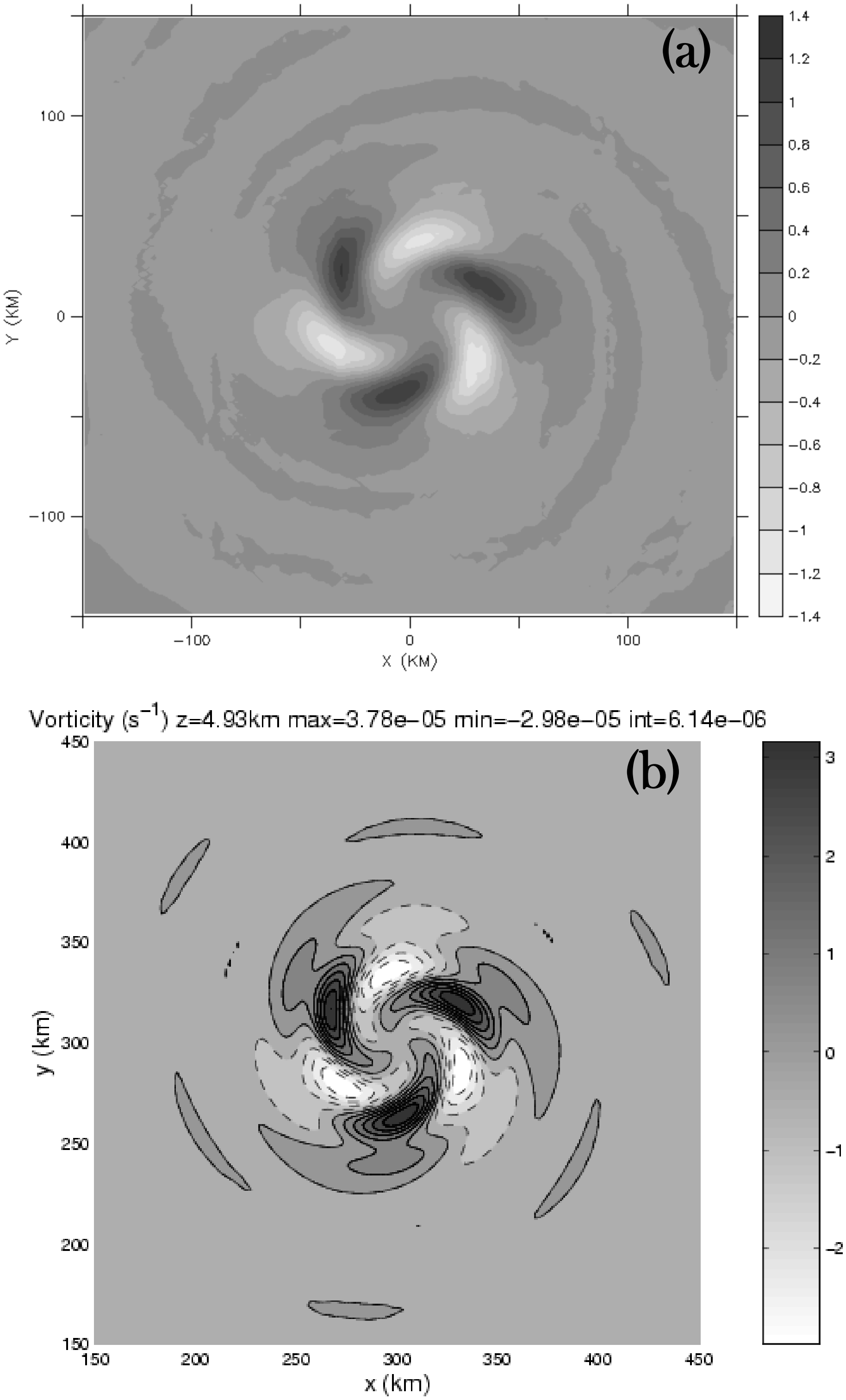

Figure 41. Perturbation vorticity ($\times 10^{-5}$ s^{-1}) at ~ 5 km height and t = 2 h. (a) HIGRAD using the control setup (see text) and (b) WRF using the setup described in NG03 (courtesy of Dave Nolan). Used with permission of the AMS.

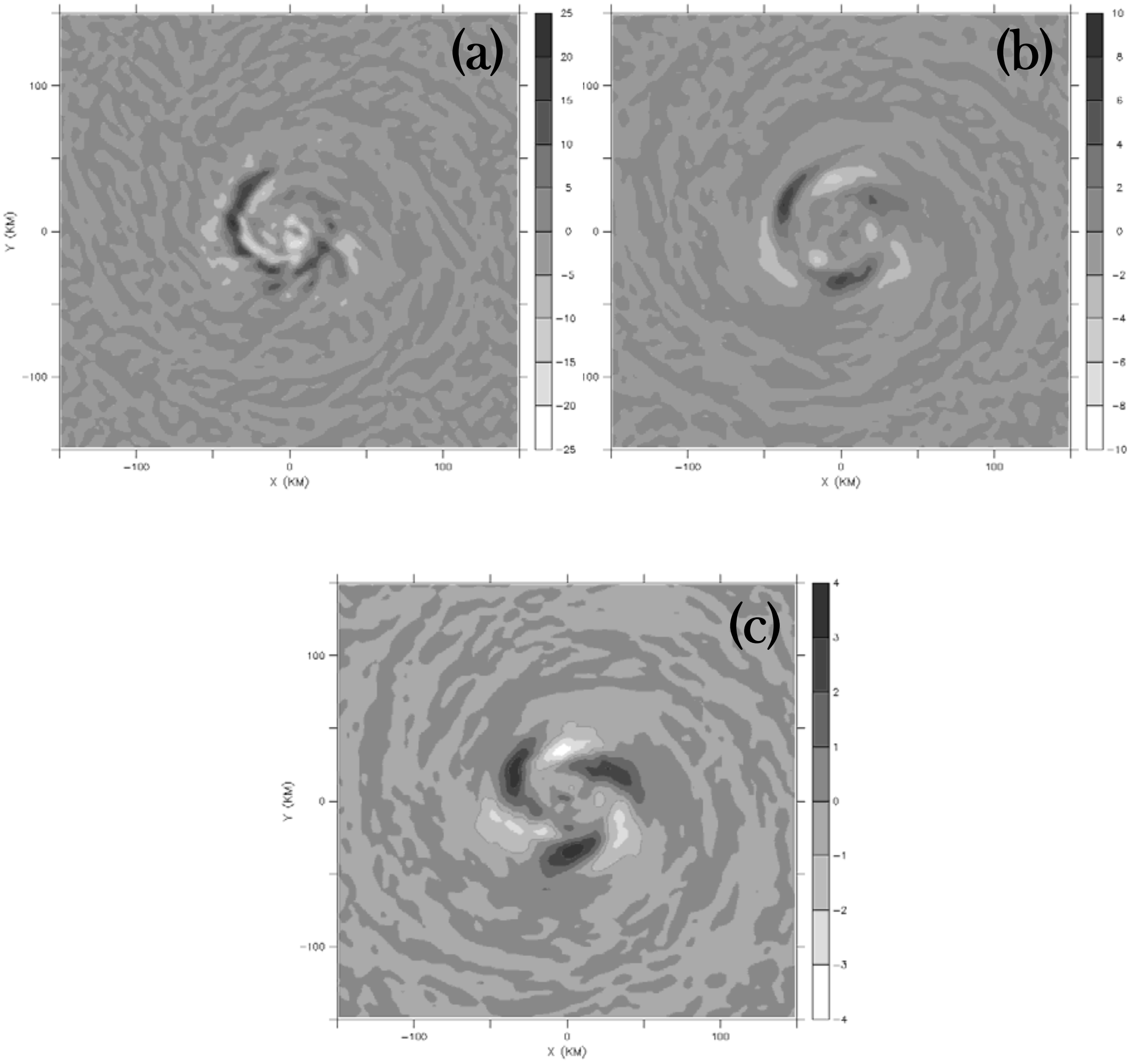

Figure 42. Perturbation vorticity (×10^{-5} s^{-1}) at ~ 5 km height and t = 2 h in HIGRAD for constant eddy diffusivity values of (a) 40 m^2 s^{-1} (b) 100 m^2 s^{-1} and (c) 200 m^2 s^{-1}.

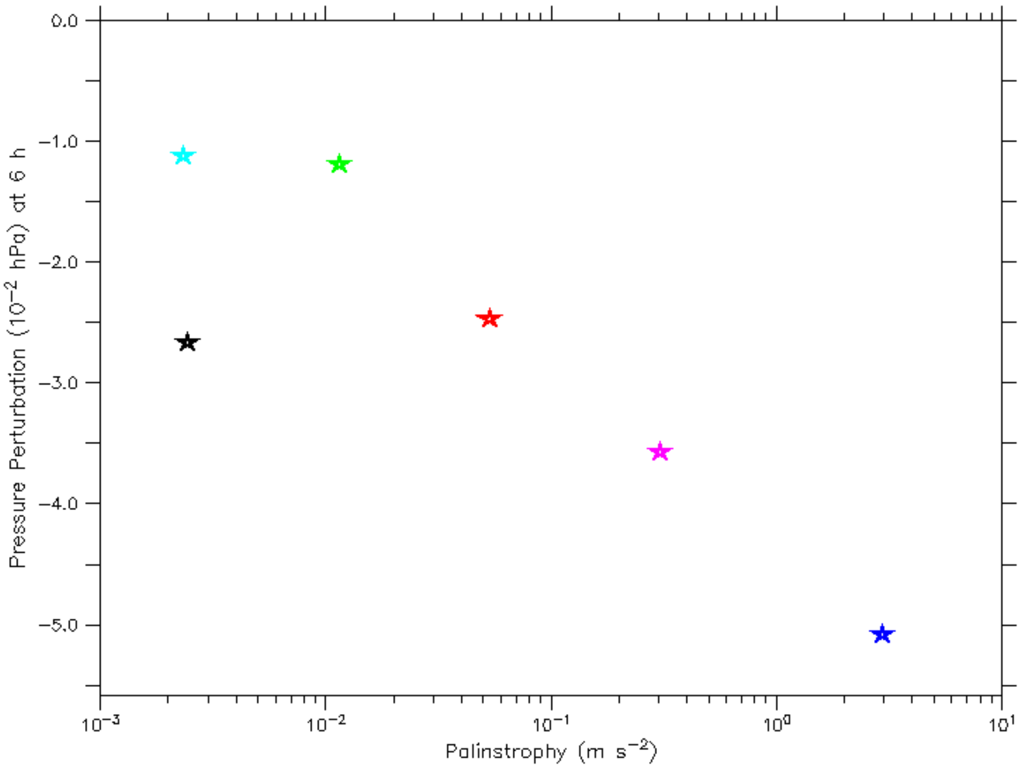

Figure 43. Domain integrated palinstrophy (equation 16) as a function of 6 h pressure perturbation for various values of the eddy diffusivity in HIGRAD. The dark blue star is for a constant eddy diffusivity of 40 $m^2 s^{-1}$, the pink star for 70 $m^2 s^{-1}$, the red star for 100 $m^2 s^{-1}$, the green star for 200 $m^2 s^{-1}$, the turquoise star for 800 $m^2 s^{-1}$, and the black star represents the default eddy diffusivity scheme (see text).

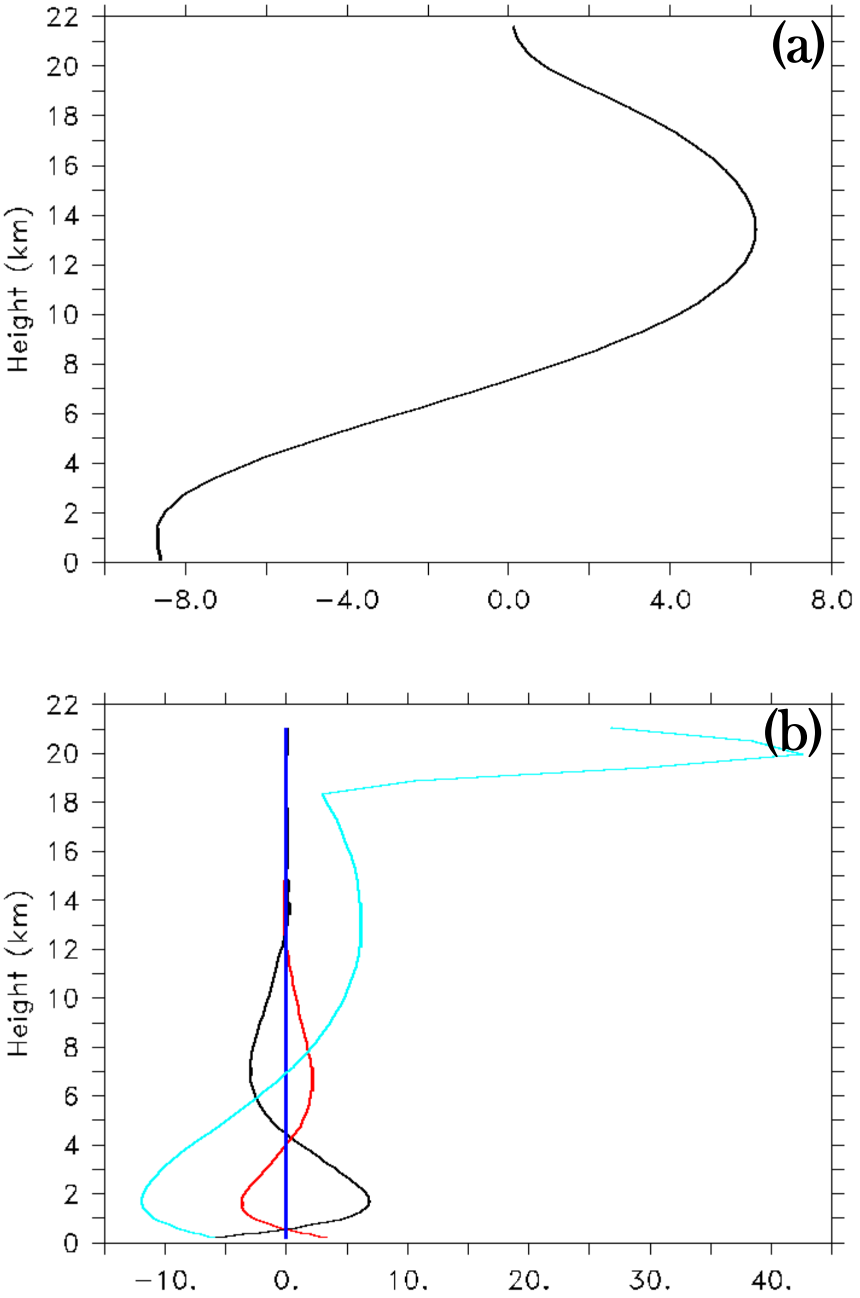

Figure 44. Vertical profiles of terms from the AAM equation in m^2 s^{-2} (multiplied by 10^5) at a radius of 40 km (inside the RMW) valid for a 6 h simulation. (a) the storage term and (b) the diffusion term (turquoise), the symmetric radial flux term (black) and the symmetric vertical flux term (red). The eddy flux terms were all zero; only the eddy vertical flux (blue) is visible. Note that each AAM flux divergence term incorporates the signs in equation (22).

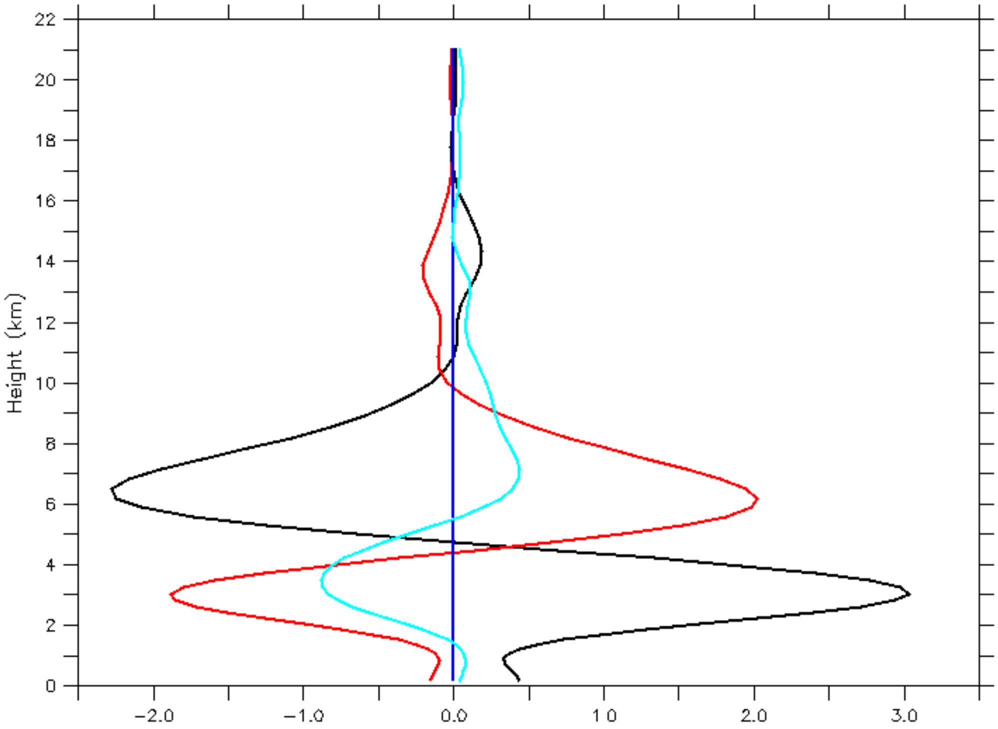

Figure 45. Vertical profiles of terms from the AAM equation in $m^2 s^{-2}$ at a radius of 40 km (inside the RMW) averaged over a 6 h simulation. All lines mean the same as those shown in Fig. 44b. Note that the terms represent perturbation quantities (see text).

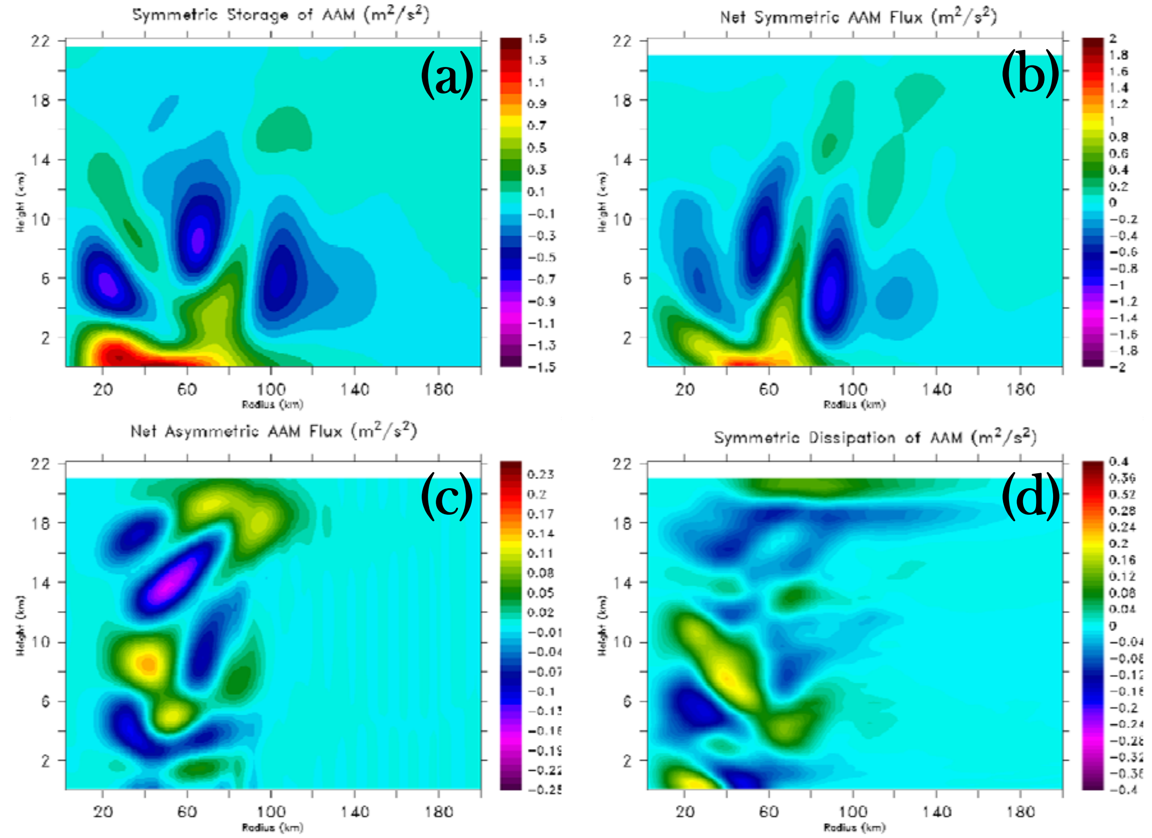

Figure 46. Contour plots of terms from the AAM equation in m^2 s^{-2} for the 1 K WN3 thermal anomaly at 30 minutes into the simulation. (a) Axisymmetric storage (b) net axisymmetric flux divergence (c) net asymmetric flux divergence and (d) axisymmetric diffusion. Note that the terms represent perturbation quantities and the signs in equation (22) have been incorporated (see text for more details).

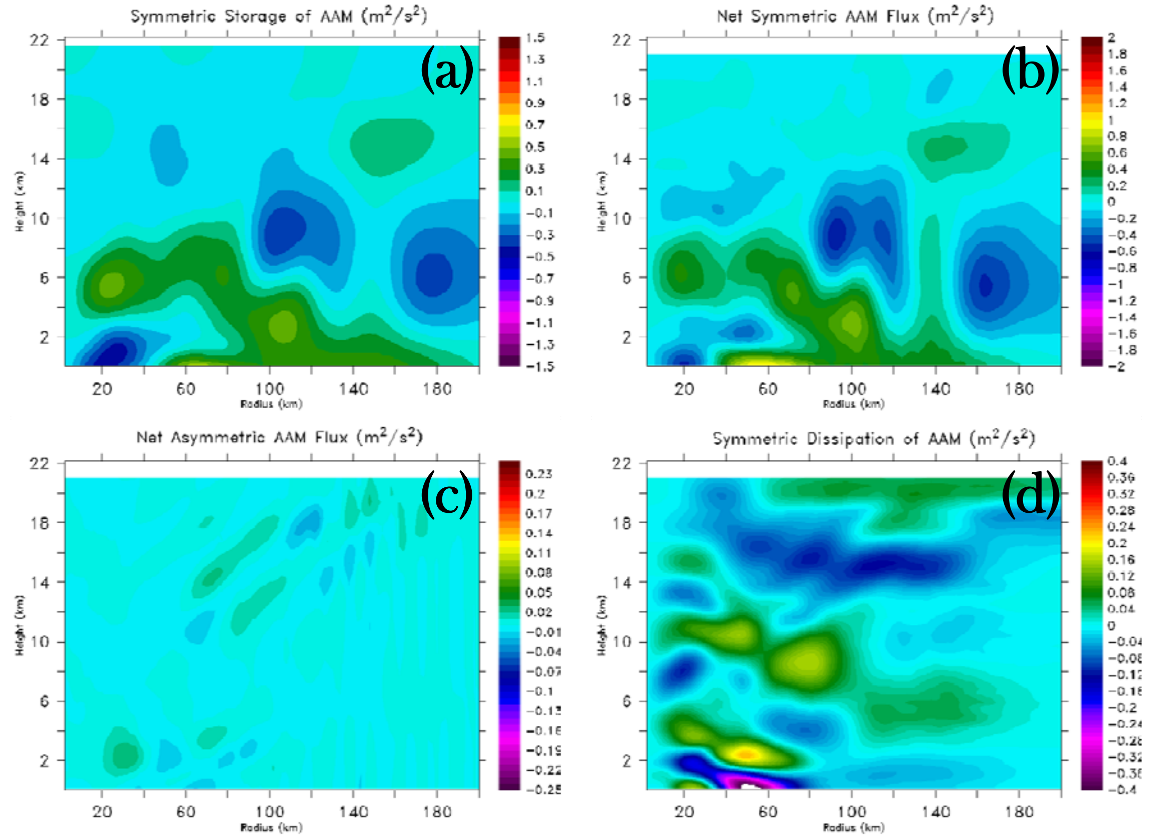

Figure 47. Same as Fig. 46, only at 60 minutes into the simulation.

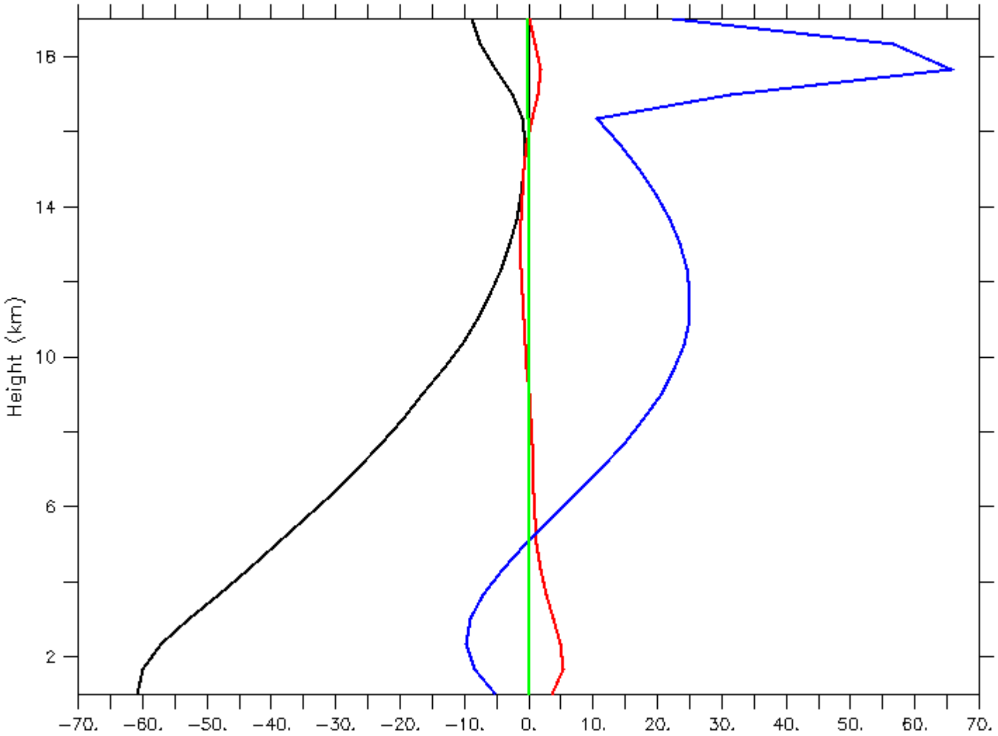

Figure 48. Vertical profiles of terms from the approximate form of the radial momentum equation (24) in $m^2\ s^{-2}$ (multiplied by 10^5) at a radius of 40 km (inside the RMW) and averaged over a 6 h simulation. The green line is the storage term, the black line represents the sum of the three terms that comprise gradient wind balance and the red line is the radial diffusion term. In addition, the tangential component of diffusion is shown by the blue line.

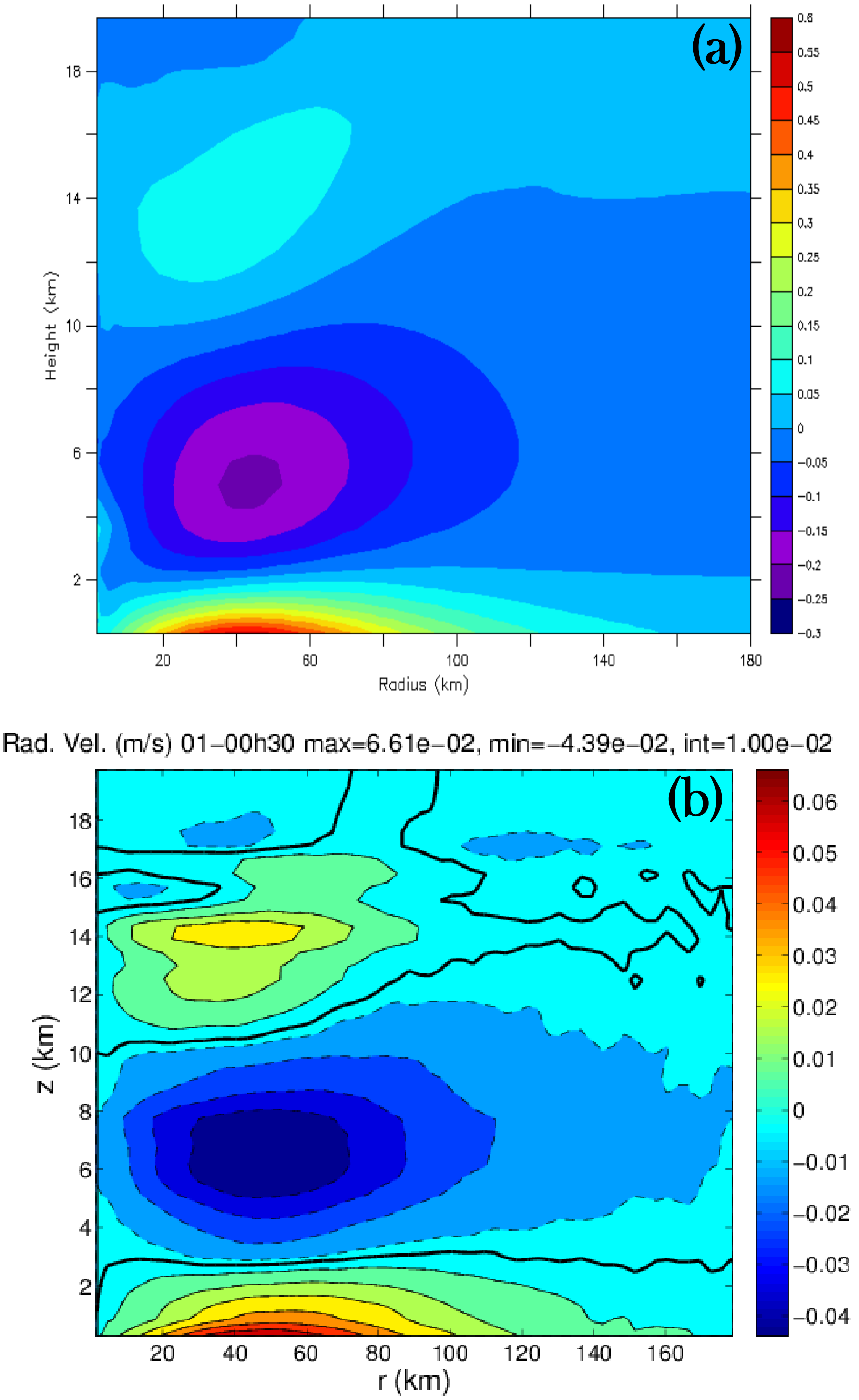

Figure 49. Azimuthal mean radial wind (m s^{-1}) at 30 minutes into the simulations described in the text. (a) HIGRAD and (b) WRF (courtesy of David Nolan).

CHAPTER 4

SUMMARY AND CONCLUSIONS

The study of tropical cyclones (TCs) has clear value through the potential mitigation of losses from not only human life, but productivity and infrastructure as well. Although tremendous progress has been made in our understanding of these highly nonlinear, complex systems, fundamental questions on the structure of convection and the impacts of axisymmetric and asymmetric processes still remain. In this study, the inner-core dynamics of TCs was analyzed from an observational and idealized numerical modeling perspective to address these fundamental questions.

4.1 Latent Heat Retrieval Algorithm

In chapter two, a newly revised algorithm for computing the latent heating associated with warm rain microphysics (condensation and evaporation) in TCs from airborne Doppler radar observations was presented. Several advancements in the basic algorithm (Roux 1985; Roux and Ju 1990) were developed including: (a) analyzing the scheme within the dynamically consistent framework of a numerical model, (b) developing a precipitation budget storage term parameterization and (c) identifying sensitivities and errors in the retrievals through the use of ancillary data sources and uncertainty analysis.

The determination of the saturation state was shown to be an important part of the algorithm. While strong vertical velocities will virtually always be saturated in order to provide the necessary buoyancy forcing (Braun 2002; Eastin et al. 2005), weak to moderate vertical velocities require calculation or observation of the saturation state. Analysis of flight-level data in the inner-core of intense hurricanes as well as a high-resolution numerical model simulation of Hurricane Bonnie (1998; Braun 2006) advocates that for $|w| > 5 \text{ m s}^{-1}$, saturation can be assumed. Vertical velocities at or below 5 m s^{-1}, which contain the vast majority of the upward mass flux in TCs (~ 70 %;

Black et al. 1996; Braun 2002) were shown to have larger variability in their saturation state and thus, more information is needed.

In the present algorithm, saturation was determined by solving for the net production of precipitation in a reduced form of the precipitation continuity equation. Cloud water production, which occurs when the air is saturated, was shown to explain ~71 % of the variability in the net production of precipitation at all temperatures and ~87 % at temperatures > 0°C. The mechanism for the production of precipitation described by the cloud water is simply the collision-coalescence process (Rogers and Yau 1989). There are errors in the saturation computation due to more complicated physics (mixed-phase regions and cloud boundaries) and when applying the algorithm to Doppler radars (resolution in time/space, attenuation and calibration). A positive aspect of the saturation algorithm is the ability to accept some error as only the *condition* of saturation is necessary.

Latent heating rate sensitivity tests showed that random errors were small (mean of less than 10 %) from the association of saturation with the net production of precipitation. The heating errors were larger from assuming steady-state in the precipitation continuity equation (mean of ~ 20 %). A parameterization for the storage term based largely on the tangential advective flux of precipitation (a consequence of the divergence theorem) was developed that shows promise for reducing the steady-state uncertainties in TCs.

Applying the new algorithm to NOAA P-3 airborne Doppler radar observations, the three- and four-dimensional structure of the latent heat of condensation/evaporation in rapidly intensifying Hurricane Guillermo (1997) was presented. Given the fact that latent heat is the primary energy source for TCs and that considerable uncertainty exists in previous observational studies and numerical model microphysics schemes, the new retrievals could prove quite useful for the community. The dominant source of error in the latent heating magnitude is the vertical velocity with only minor contributions from the thermodynamic information. For characteristic errors in vertical velocity from the Guillermo P-3 analyses (Reasor et al. 2009), an uncertainty of ~32 % in the heating magnitude was found for updrafts of 5 m s^{-1} and ~156 % for updrafts of 1 m s^{-1}. Uncertainty in the retrievals due to sampling issues (for updrafts > 5 m s^{-1}) was small (14 %). To augment the P-3 retrievals, the latent heat of condensation from a composite hot tower using nadir-pointing, high-resolution, EDOP data was also computed and is shown in Fig. 14 for reference.

The ability of the retrievals to reproduce the observed wind fields of Guillermo was tested using realistic, full-physics simulations (using HIGRAD) of the storm at a resolution consistent with the Doppler analyses (2 km). Results show that the latent heat retrieval run outperforms a simulation that relies on the model microphysics scheme in a "freemode" (only initial observational forcing) run in terms of wind speed RMSEs, explained variance and eye/eyewall structure. The larger errors in the freemode run are likely due to uncertainties in the model associated with: (1) the transport of water vapor which is a function of diffusion and numerical approximations to advection and (2) the microphysics scheme. However, in terms of integrated wind speed errors, the performance of the retrieval and freemode runs were quite similar. The retrieval run produced wind fields that were generally too strong while the freemode run produced wind fields that were generally too weak. These results indicate that the retrievals are releasing too much heat (due to errors in both the computation of saturation and the retrieved vertical velocity from the Doppler analysis, which had a small positive bias) while the freemode run is not releasing enough heat (due to uncertainties in the microphysics scheme, specifically the limits on heat release). Simulations with the retrievals where saturation was assumed for the entire inner-core of Guillermo produced wind fields that were much too strong, further motivating the need for the accurate determination of the saturation state.

Taking in the grand scope of these analyses, overall the algorithm does a reasonably good job of computing the latent heat field in a TC. Even though errors in the vertical velocity can lead to large uncertainties in the latent heating field for small updrafts/downdrafts, in an integrated sense the errors are not as drastic. The clear advantage of the retrievals in terms of producing a more accurate wind structure of Guillermo highlights the need for continuous observation of convective events in the hurricane inner-core. While we believe that airborne Doppler radars provide the highest quality observations of convection, infrequent sampling of storm cores and relatively poor time continuity of the measurements limits the use of these data from an operational perspective. The use of passive lightning imagers with their large field-of-views and continuous mapping of 2-D and even 3-D electrical discharges occurring within deep convection may prove useful for improving forecasts of hurricane structure. Computing heating rates from lightning measurements will likely be difficult, but placement of convection in near real time appears to be a very attainable goal.

4.2 The Axisymmetrization Process

In the second part of this work, the three-dimensional dynamics associated with the release of heat in the TC core was analyzed using an idealized setup of a nonlinear numerical model (HIGRAD). Early attempts at reproducing the results of Nolan and Grasso (2003) with HIGRAD revealed very good agreement with the vast majority of the axisymmetric results. However, a large discrepancy was found with the impact of pure thermal asymmetries. For a 1 K wavenumber three asymmetry at 40 km radius and 5 km height, NG03 found a 6 h pressure perturbation of 4.1×10^{-4} hPa in their linear model and the WRF model while HIGRAD simulations with the same setup and exact initial conditions resulted in -2.7×10^{-2} hPa. A large number of sensitivity tests were conducted including using a much larger domain, different resolutions, changes to the boundary conditions and upper gravity wave absorber, initialization procedures, different wavenumber perturbations and locations (in radius and height) as well as types and amounts of explicit diffusion. After all these tests and analyses, the same core result was found. That is, thermal asymmetries had a *significant* impact on the vortex in HIGRAD with 6 h pressure perturbations generally two orders of magnitude larger than that found in NG03.

The treatment of explicit diffusion was found to produce the largest changes to the control run. A near linear relationship was found between the magnitude of the 6 h pressure perturbation and the value of the eddy diffusivity with lower values (less than 100 m^2 s^{-1}) producing a more intense vortex. In addition, the sign of the pressure perturbation was found to change from negative to positive when switching from a stress tensor to a Laplacian operator for diffusion of momentum. The HIGRAD model appeared to produce noisy results for the same eddy diffusivity value (40 m^2 s^{-1}) specified by NG03 in their WRF simulations. In order to produce similar vorticity asymmetries to

WRF, an eddy diffusivity value of 4000 m^2 s^{-1} was required in HIGRAD. This result suggests that the levels of implicit diffusion between the two models are quite different with HIGRAD having a lower amount. The significant sensitivity of our results to effective (implicit and explicit) diffusion implies fundamental impacts on asymmetric tropical cyclone dynamics such as the generation of vortex Rossby waves from heating perturbations and the ensuing axisymmetrization process. This is consistent with the results of Bryan and Rotunno (2009) for axisymmetric numerical simulations.

Absolute angular momentum budgets demonstrated that the essential difference between the study of NG03 and that analyzed here was the presence of a significant, axisymmetric secondary circulation in the basic-state vortex. When a wavenumber three thermal asymmetry was imposed on this vortex, the axisymmetric fluxes of angular momentum dominated the evolution immediately. For basic-state vortices without or with insignificant secondary circulations (like those in NG03), axisymmetric fluxes of angular momentum take a period of time to develop in response to the asymmetric forcing. The decay rates of the asymmetric angular momentum fluxes were found to be much faster than those shown in NG03 suggesting the basic-state secondary circulation may accelerate the axisymmetrization process.

Radial momentum budgets demonstrated that the cause of the significant, axisymmetric secondary circulation was the diffusion of tangential velocity which produced a gradient wind imbalance and associated radial flow. After a few hours, diffusion of radial velocity became important in the maintenance of the secondary circulation at lower levels where the radial flow was the strongest. Comparisons of the radial flow in HIGRAD and WRF for a simple explicit diffusion setup revealed the same structure, but with values that were almost an order of magnitude larger in HIGRAD consistent with the hypothesis that the implicit diffusion is very different between the two models. Although explicit diffusion was the sole source for the basic-state secondary circulation in this idealized study, preliminary results imply that other sources such as surface friction and/or inner-core heating may also produce a large response from purely asymmetric heating.

Given the inherent uncertainty associated with implicit (numerical) and explicit (sub-grid) diffusion in numerical models and the fact that secondary circulations are ubiquitous features of real tropical cyclones, this research suggests two main areas for future work. First, a physical understanding is needed for how the impacts of asymmetric heating are modified by basic-state secondary circulations. Second, the role of turbulence in TC inner-core dynamics needs assessment through high-resolution observations (such as EDOP and HIWRAP; Heymsfield et al. 1996; Heymsfield et al. 2007; Guimond et al. 2010) and large eddy numerical simulations in order to reduce the uncertainty in explicit diffusion schemes. The results of this work also suggest that numerical approximations and their associated implicit diffusion need assessment for various degrees of realism.

REFERENCES

Adler, R.F., and E.B. Rodgers, 1977: Satellite-observed latent heat release in a tropical cyclone. *Mon. Wea. Rev.*, **105,** 956-963.

Black, R.A, 1990: Radar reflectivity-ice water content relationships for use above the melting level in hurricanes. *J. Appl. Meteor.*, **29,** 955-961.

——, G. M. Heymsfield, and J. Hallett, 2003: Extra large particle images at 12 km in a hurricane eyewall: Evidence of high-altitude supercooled water? *Geophys. Res. Lett.* ***30,*** 2124, doi:10.1029/2003GL017864.

Black, M.L., R.W. Burpee, and F.D. Marks, Jr., 1996: Vertical motion characteristics of tropical cyclones determined with airborne Doppler radial velocities. *J. Atmos. Sci.*, **53,** 1887-1909.

Braun, S.A., and W.-K. Tao, 2000: Sensitivity of high-resolution simulations of Hurricane Bob (1991) to planetary boundary layer parameterizations. *Mon. Wea. Rev.*, **128,** 3941-3961.

——, 2002: A cloud-resolving simulation of Hurricane Bob (1991): Storm structure and eyewall buoyancy. *Mon. Wea. Rev.,* **130**, 1573–1592.

——, M.T. Montgomery, and Z. Pu, 2006: High-resolution simulation of Hurricane Bonnie (1998). Part I: The organization of eyewall vertical motion. *J. Atmos. Sci.*, **63,** 19-42.

——, 2006: High-resolution simulation of Hurricane Bonnie (1998). Part II: Water budget. *J. Atmos. Sci.*, **63,** 43-64.

Bryan, G.H., J.C. Wyngaard, and J.M. Fritsch, 2003: Resolution requirements for the simulation of deep moist convection. *Mon. Wea. Rev.*, **131,** 2394-2416.

——, and R. Rotunno, 2009: The maximum intensity of tropical cyclones in axisymmetric numerical model simulations. *Mon. Wea. Rev.*, **137,** 1770-1789.

Cecil, D. J., and E. J. Zipser, 1999: Relationships between tropical cyclone intensity and satellite-based indicators of inner core convection: 85-GHz ice-scattering signature and lightning. *Mon. Wea. Rev.,* **127,** 103-123.

Chang, S.W., 1981: The impact of satellite-sensed winds on intensity forecasts of tropical cyclones. *Mon. Wea. Rev.*, **109,** 539-553.

Charney, J.G., and A. Eliassen, 1964: On the growth of the hurricane depression. *J. Atmos. Sci.*, **21,** 68-75.

Davis, C., and Coauthors, 2008: Prediction of landfalling hurricanes with the advanced hurricane WRF model. *Mon. Wea. Rev.*, **136,** 1990-2005.

DeMaria, M., M. Mainelli, L. K. Shay, J. A. Knaff, and J. Kaplan, 2005: Further improvements to the Statistical Hurricane Intensity Prediction Scheme (SHIPS). *Wea. Forecasting.,* **20,** 531-543.

Dendy, J.E., Jr., 1982: Black Box Multigrid. *J. Comput. Phys*., **48,** 366.

Doviak, R.J., and D.S. Zrnic, 1984: *Doppler Radar and Weather Observations*. Academic Press, 458 pp.

Eastin, M.D., W.M. Gray, and P.G. Black, 2005: Buoyancy of convective vertical motions in the inner core of intense hurricanes. Part I: General statistics. *Mon. Wea. Rev*., **133,** 188-208.

Emanuel, K.A., 1986: An air-sea interaction theory for tropical cyclones. Part I: Steady-state maintenance. *J. Atmos. Sci*., **43,** 2044-2061.

——, 1995: Sensitivity of tropical cyclones to surface exchange coefficients and a revised steady-state model incorporating eye dynamics. *J. Atmos. Sci.,* **52,** 3969-3976.

——, 1997: Some aspects of hurricane inner-core dynamics and energetics. *J. Atmos. Sci*., **54,** 1014-1026.

Farrell, B.F., 1982: The initial growth of disturbances in a baroclinic flow. *J. Atmos. Sci*., **39,** 1663-1686.

Gamache, J.F., R.A. Houze, Jr., and F.D. Marks, Jr., 1993: Dual-aircraft investigation of the inner core of Hurricane Norbert. Part III: Water budget. *J. Atmos. Sci*., **50,** 3221-3243.

——, F. D. Marks, Jr., and F. Roux, 1995: Comparison of three airborne Doppler sampling techniques with airborne in situ wind observations in Hurricane Gustav (1990). *J. Atmos. and Oceanic Technol.,* **12,** 171–181.

——, 1997: Evaluation of a fully three-dimensional variational Doppler analysis technique. Preprints, *28th Conf. on Radar Meteorology*, Austin, TX, Amer. Meteor. Soc., 422-423.

Gao, J., M. Xue, A. Shaprio, and K.K. Droegemeier, 1999: A variational method for the analysis of three-dimensional wind fields from two Doppler radars. *Mon. Wea. Rev.*, **127,** 2128-2142.

Guimond, S.R., G.M. Heymsfield, and F.J. Turk, 2010: Multiscale observations of

Hurricane Dennis (2005): The effects of hot towers on rapid intensification. *J. Atmos. Sci.*, **67,** 633-654.

Hack J. J., and W. H. Schubert, 1986: Nonlinear response of atmospheric vortices to heating by organized cumulus convection. *J. Atmos. Sci.*, **43,** 1559–1573.

Hanley, D.E., J. Molinari, and D. Keyser, 2001: A composite study of the interactions between tropical cyclones and upper tropospheric troughs. *Mon. Wea. Rev.*, **129,** 2570-2584.

Heymsfield, G.M., and Coauthors, 1996: The EDOP radar system on the high-altitude NASA ER-2 aircraft. *J. Atmos. Oceanic Technol.,* **13,** 795-809.

——, J.B. Halverson, and I.J. Caylor, 1999: A wintertime Gulf Coast squall line observed by EDOP airborne Doppler radar. *Mon. Wea. Rev.,* **127,** 2928-2949.

——, B. Geerts, and L. Tian, 2000: TRMM precipitation radar reflectivity profiles as compared with high-resolution airborne and ground-based radar measurements. *J. Appl. Meteor.*, **39,** 2080-2102.

——, J.B. Halverson, J. Simpson, L. Tian, and T.P. Bui, 2001: ER-2 Doppler radar investigations of the eyewall of Hurricane Bonnie during the Convection and Moisture Experiment-3. *J. Appl. Meteor.,* **40,** 1310-1330.

——, J. Carswell, L. Li, D. Schaubert, and J. Creticos, 2007: *NASA Science Technology Conference, College Park, MD.* (http://esto.nasa.gov/conferences/nstc2007/papers/Carswell_James_B5P2_NSTC-07-0085.pdf).

——, L. Tian, A.J. Heymsfield, L. Li, and S. Guimond, 2010: Characteristics of deep tropical and subtropical convection from nadir-viewing high-altitude airborne Doppler radar. *J. Atmos. Sci.*, **67,** 285-308.

Hoke, J.E., and R.A. Anthes, 1976: The initialization of numerical models by a dynamic-initialization technique. *Mon. Wea. Rev.*, **104,** 1551-1556.

Houze, R.A., Jr., 1993: *Cloud Dynamics*. Academic Press, 573 pp.

Jordan, C.L., 1958: Mean soundings for the West Indies area. *J. Meteor.*, **15,** 91-97.

Klemp, J.B., W.C. Skamarock, and J. Dudhia, 2007: Conservative split-explicit time integration methods for the compressible nonhydrostatic equations. *Mon. Wea. Rev.*, **135,** 2897-2913.

Kossin, J.P., and W.H. Schubert, 2003: Diffusion versus advective rearrangement of a circular vortex sheet. *J. Atmos. Sci.*, **60,** 586-589.

Krishnamurti, T.N., W. Han, B. Jha, and H.S. Bedi, 1998: Numerical prediction of Hurricane Opal. *Mon. Wea. Rev.*, **126,** 1347-1363.

Kuo, H.L., 1965: On formation and intensification of tropical cyclones through latent heat release by cumulus convection. *J. Atmos. Sci.*, **22,** 40-63.

Leonard, B., and J. Drummond, 1995: Why you should not use ‘hybrid’ ‘power-law’ or related exponential schemes for convective modeling—There are better alternatives. *Int. J. Numer. Methods Fluids*, **20,** 421-442.

Lilly, D.K., and B.F. Jewett, 1990: Momentum and kinetic energy budgets of simulated supercell thunderstorms. *J. Atmos. Sci.*, **47,** 707-726.

Marks, F.D., Jr., R.A. Houze, Jr., and J.F. Gamache, 1992: Dual-aircraft investigation of the inner core of Hurricane Norbert. Part I: Kinematic structure. *J. Atmos. Sci.*, **49,** 919-942.

Mayfield, M., 1997: Tropical cyclone report: Hurricane Guillermo 30 July – 15 August 1997. National Hurricane Center, 7 pp. [Available online at http://www.nhc.noaa.gov/1997guillerm.html].

McFarquhar, G.M., H. Zhang, G. Heymsfield, R. Hood, J. Dudhia, J.B. Halverson, and F. Marks, Jr., 2006: Factors affecting the evolution of Hurricane Erin (2001) and the distributions of hydrometeors: Role of microphysical processes. *J. Atmos. Sci.*, **63,** 127-150.

McWilliams, J.C., L.P. Graves, and M.T. Montgomery, 2003: A formal theory for vortex Rossby waves and vortex evolution. *Geophys. Astrophys. Fluid Dyn.*, **97,** 275-309

Melander, M.V., J.C. McWilliams, and N.J. Zabusky, 1987: Axisymmetrization and vorticity-gradient intensification of an isolated two-dimensional vortex through filamentation. *J. Fluid Mech.*, **178,** 137-159.

Molinari J., and D. Vollaro, 1989: External influences on hurricane intensity. Part I: Outflow layer eddy angular momentum fluxes. *J. Atmos. Sci.*, **46,** 1093-1105.

——, ——, and S. Skubis, 1993: Application of the Eliassen balanced model to real-data tropical cyclones. *Mon. Wea. Rev.*, **121,** 2409-2419.

Moller, J.D., and M.T. Montgomery, 2000: Tropical cyclone evolution via potential vorticity anomalies in a three-dimensional balance model. *J. Atmos. Sci.*, **57,** 3366-3387.

Montgomery M. T., and R. J. Kallenbach, 1997: A theory for vortex Rossby waves and its application to spiral bands and intensity changes in hurricanes. *Quart. J. Roy. Meteor. Soc.*, **123**, 435–465.

——, and J. Enagonio, 1998: Tropical cyclogenesis via convectively forced vortex Rossby waves in a three-dimensional quasi-geostrophic model. *J. Atmos. Sci.*, **55,** 3176-3207.

——, M.E. Nicholls, T.A. Cram and A. Saunders, 2006: A vortical hot tower route to tropical cyclogenesis. *J. Atmos. Sci.,* **63,** 355-386.

Morrow, C.R., 2008: An expanding database of dual-Doppler tropical cyclone observations. M.S. thesis, Dept. of Meteorology, The Florida State University, 146 pp.

Navon, I.M., X. Zou, J. Derber, and J. Sela, 1992: Variational data assimilation with an adiabatic version of the NMC spectral model. *Mon. Wea. Rev.*, **120,** 1433-1446.

Nolan, D.S., and B.F. Farrell, 1999a: Generalized stability analyses of asymmetric distrurbances in one- and two-celled vortices maintained by radial inflow. *J. Atmos. Sci.*, **56,** 1282-1307.

——, and ——, 1999b: The intensification of two-dimensional swirling flows by stochastic asymmetric forcing. *J. Atmos. Sci.*, **56,** 3937-3962.

——, and M. T. Montgomery, 2002: Nonhydrostatic, three-dimensional perturbations to balanced, hurricane-like vortices. Part I: Linearized formulation, stability, and evolution. *J. Atmos. Sci.*, **59,** 2989–3020.

——, and L.D. Grasso, 2003: Three-dimensional, nonhydrostatic perturbations to balanced, hurricane-like vortices. Part II: Symmetric response and nonlinear simulations. *J. Atmos. Sci.*, **60,** 2717-2745.

——, Y. Moon, and D.P.Stern, 2007: Tropical cyclone intensification from asymmetric convection: Energetics and efficiency. *J. Atmos. Sci.*, **64,** 3377-3405.

Orr, W.M., 1907: Stability or instability of the steady motions of a perfect liquid. *Proc. Roy. Irish Acad.*, **27,** 9-69.

Petty, G.W., 2006: *A First Course in Atmospheric Radiation.* Sundog Publishing, 459 pp.

Pielke, R.A., Sr., 2002: *Mesoscale Meteorological Modeling.* Academic Press, 676 pp.

Reasor, P.D., M.T. Montgomery, F.D. Marks, Jr., and J.F. Gamache, 2000: Low-wavenumber structure and evolution of the hurricane inner core observed by airborne dual-Doppler radar. *Mon. Wea. Rev.*, **128,** 1653-1680.

——, M.D. Eastin, and J.F. Gamache, 2009: Rapidly intensifying Hurricane Guillermo

(1997). Part I: Low-wavenumber structure and evolution. *Mon. Wea. Rev.*, **137,** 603-631.

Reisner, J.M., V.A. Mousseau, A.A. Wyszogrodzki, and D.A. Knoll, 2005: An implicitly balanced hurricane model with physics-based preconditioning. *Mon. Wea. Rev.*, **133,** 1003-1022.

——, and C.A. Jeffery, 2009: A smooth cloud model. *Mon. Wea. Rev.*, **137,** 1825-1843.

Reynolds, R.W., T.M. Smith, C. Liu, D.B. Chelton, K.S. Casey and M.G. Schlax, 2007: Daily high-resolution-blended analyses for sea surface temperature. *J. Climate*, **20,** 5473-5496.

Rodgers, E., W. Olson, J. Halverson, J. Simpson, and H. Pierce, 2000: Environmental forcing of Supertyphoon Paka's (1997) latent heat structure. *J. Appl. Meteor.*, **39,** 1983-2006.

Rogers, R.R., and M.K. Yau, 1989: *A Short Course in Cloud Physics.* Butterworth-Heinemann publishers, 304 pp.

Rogers, R.F., M.L. Black, S.S. Chen, and R.A. Black, 2007: An evaluation of microphysics fields from mesoscale model simulations of tropical cyclones. Part I: Comparisons with observations. *J. Atmos. Sci.*, **64,** 1811-1834.

Rotunno, R., and K.A. Emanuel, 1987: An air-sea interaction theory for tropical cyclones. Part II: Evolutionary study using a nonhydrostatic axisymmetric numerical model. *J. Atmos. Sci.,* **44,** 542-561.

Roux, F., 1985: Retrieval of thermodynamic fields from multiple-Doppler radar data using the equations of motion and the thermodynamic equation. *Mon. Wea. Rev.*, **113,** 2142-2157.

——, and S. Ju, 1990: Single-Doppler observations of a west African squall line on 27-28 May 1981 during COPT 81: Kinematics, thermodynamics and water budget. *Mon. Wea. Rev.*, **118,** 1826-1854.

Schubert, W.H., M. T. Montgomery, R. K. Taft, T. A. Guinn, S. R. Fulton, J. P. Kossin, and J. P. Edwards, 1999: Polygonal eyewalls, asymmetric eye contraction, and potential vorticity mixing in hurricanes. *J. Atmos. Sci.*, **56,** 1197–1223.

Sitkowski M., and G. M. Barnes, 2009: Low-level thermodynamic, kinematic, and reflectivity fields of Hurricane Guillermo (1997) during rapid intensification. *Mon. Wea. Rev.*, **137,** 645–663.

Skamarock, W.C., 2004: Evaluating mesoscale NWP models using kinetic energy spectra. *Mon. Wea. Rev.*, **132,** 3019-3032.

Smagorinsky, J., 1963: General circulation experiments with the primitive equations. I: The basic experiment. *Mon. Wea. Rev.*, **91,** 99-164.

Smith, G.B., and M.T. Montgomery, 1995: Vortex axisymmetrization: Dependence of azimuthal wavenumber or asymmetric radial radial structure changes. *Quart. J. Roy. Meteor. Soc.,* **121,** 1615-1650.

Stull, R.B., 1988: *An Introduction to Boundary Layer Meteorology*. Kluwer academic publishers, 666 pp.

Takemi, T., and R. Rotunno, 2003: The effects of subgrid model mixing and numerical filtering in simulations of mesoscale cloud systems. *Mon. Wea. Rev.*, **131,** 2085-2101.

Tao, W.-K. and Coauthors, 2006: Retrieval of latent heating from TRMM measurements. *Bull. Amer. Meteor. Soc.*, **87,** 1555-1572.

Tong, H., V. Chandrasekar, K.R. Knupp, and J. Stalker, 1998: Multiparameter radar observations of time evolution of convective storms: Evaluation of water budgets and latent heating rates. *J. Atmos. Oceanic Technol.*, **15,** 1097-1109.

Tory, K. J., M. T. Montgomery, and N. E. Davidson, 2006: Prediction and diagnosis of tropical cyclone formation in an NWP system. Part I: The critical role of vortex enhancement in deep convection. *J. Atmos. Sci.,* **63,** 3077-3090.

Ulbrich, C. W., and P. B. Chilson, 1994: Effects of variations in precipitation size distribution and fallspeed law parameters on relations between mean Doppler fallspeed and reflectivity factor. *J. Atmos. Oceanic Technol.,* **11,** 1656–1663.

Weisman, M.L., W.C. Skamarock, and J.B. Klemp, 1997: The resolution dependence of explicitly modeled convective systems. *Mon. Wea. Rev.*, **125,** 527-548.

Wicker, L.J., and W.C. Skamarock, 2002: Time-splitting methods for elastic models using forward time schemes. *Mon. Wea. Rev.*, **130,** 2088-2097.

Wimmers, A.J., and C.S. Velden, 2007: MIMIC: A new approach to visualizing satellite microwave imagery of tropical cyclones. *Bull. Amer. Meteor. Soc.*, **88,** 1187-1196.

Yau, M.K., Y. Liu, D.L. Zhang, and Y. Chen, 2004: A multiscale numerical study of Hurricane Andrew (1992). Part VI: Small-scale inner-core structures and wind streaks. *Mon. Wea. Rev.*, **132,** 1410-1433.

Zhang, D.-L., Y. Liu, and M.K. Yau, 2002: A multiscale numerical study of Hurricane Andrew (1992). Part V: Inner-core thermodynamics. *Mon. Wea. Rev.*, **130,** 2745-2763.

Zou, X., I.M. Navon, and F.X. Ledimet, 1992: An optimal nudging data assimilation scheme using parameter estimation. *Quart. J. Roy. Meteor. Soc.,* **118,** 1163-1186.

——, Y. Wu, and P.S. Ray, 2010: Verification of a high-resolution model forecast using airborne Doppler radar analysis during the rapid intensification of Hurricane Guillermo. *J. Appl. Meteor.*, **49,** 807-820.

BIOGRAPHICAL SKETCH

Stephen R. Guimond

Stephen Guimond graduated from Iowa State University with a B.S. in Meteorology in the spring of 2004, then pursued graduate education at the Florida State University (FSU). He earned his Master's degree in Meteorology in the spring of 2007 under Dr. Mark Bourassa and shortly thereafter started working on his Doctoral degree. The majority of his doctorate work was under the advisement of Dr. Paul Reasor until his departure from FSU at the end of 2009. Steve finished his Ph.D. under the direction of Dr. Mark Bourassa who had been serving as his co-advisor.

Steve's research interests are broad and include: physical and dynamic Meteorology with a focus on tropical cyclones, remote sensing with a focus on Doppler radar and numerical modeling. He has experience in all of the above areas working at the Naval Research Laboratory, Los Alamos National Laboratory and NASA Goddard Space Flight Center throughout his graduate career. Upon graduation, he will be a NASA postdoctoral fellow at Goddard Space Flight Center.